UNIVERSITY
OF OSLO

Maaike Francine Maria Weerdesteijn

Solid earth deformation due to glacial mass changes above low-viscosity upper mantle

Model development, importance of contemporary ice melt, and an application to southeast Greenland

Thesis submitted for the degree of Philosophiae Doctor

The Centre for Earth Evolution and Dynamics (CEED)
Department of Geosciences
Faculty of Mathematics and Natural Sciences, University of Oslo,
Oslo, Norway

2023

Series of dissertations submitted to the
Faculty of Mathematics and Natural Sciences, University of Oslo
No. 2617

ISSN 1501-7710

Cover: UiO.
Print production: Graphic Center, University of Oslo.

Preface

This doctoral thesis titled "Solid earth deformation due to glacial mass changes above low-viscosity upper mantle: Model development, importance of contemporary ice melt, and an application to southeast Greenland" is submitted to the Department of Geosciences, Faculty of Mathematics and Natural Sciences, at the University of Oslo in partial fulfillment of the requirements for the degree of *Philosophiae Doctor*. The research presented here was conducted under the supervision of Professor Dr. Clinton P. Conrad at the Centre for Earth Evolution and Dynamics. This work was supported by the Norwegian Research Council through grant 223272 (Centre of Excellence) and 288449 (MAGPIE Project).

This thesis consists of a historical background of postglacial rebound and description of the modern field of glacial isostatic adjustment, conclusions and future directions based on the thesis research, and a collection of three first author scientific papers, of which two are published and one is a manuscript ready to be submitted, at the time of submitting this thesis. The research covered by these papers have been presented to the scientific community at several national and international conferences. Paper I covers the benchmark of a new viscoelastic solid earth deformation model in an open-source finite element code. Paper II explores the effects of a low-viscosity region in the upper mantle on solid earth deformation due to contemporary ice melt. Paper III investigates the plausibility and characteristics of a low-viscosity region, as a result of the Iceland plume, underneath southeast Greenland from deformation induced by glacial cycle to contemporary ice mass changes.

Acknowledgements

`04:10 am, 6 February 2019:  my bed, Delft, The Netherlands`
It was a week after I had presented and defended my master thesis. I felt drained. I gave myself a month-long break, to read books I have been wanting to read, to rest, to do anything I wanted to. A month before even thinking about applying for jobs. But that night, I woke up and I couldn't fall back to sleep. One week into my month-long break, and a burning question kept me awake: What is next? After years of exploring job opportunities in industry, I still hadn't found my calling. With the ups and downs experienced during my master thesis research, I also didn't think I wanted to pursue an academic career. Although, when I closed my eyes, I could still sense the intensely rewarding feeling from the received praise upon graduating. That feeling had already made me forget about all the struggles endured. Maybe research wasn't so bad after all? Is there a way I can combine research and also enjoy time outside... My search query: "research greenland antarctica fieldwork". After two hours of mindless scrolling on my phone, there it was: "PhD Research Fellowship in Magnetotellurics and Mantle Dynamics of Greenland", with only one week left to apply.

`14:30 pm, 17 March 2023:  my office, Oslo, Norway`
Fast forward to nearly four years of research, adventures, and friends richer, and only a few hours away from submitting my PhD thesis. But before I hit the submit button, I would like to take the opportunity to acknowledge all the people who supported me in my research and PhD journey, and made me feel more at home in Norway than I ever could have imagined.

First and foremost, I wish to thank my supervisor Clint. Over the years you have been incredibly supportive. Where I didn't see the innovation or new insights, you did. You encouraged me to further develop the work, which resulted in my first published PhD paper. You have always been able to provide me with guidance, whether that was research specific or more general career oriented. I am very grateful for the freedom and flexibility, which allowed me to explore wonderful polar regions in a research environment. I am grateful for never feeling pressured and for the trust you put into your PhD students. I truly feel I got to create my own path. We got to know each other during my first month of the PhD on the Greenland ice sheet, an unusual setting to say the least. I felt slightly embarrassed the day after one of the Saturday night escapades, our day off, when I was incredibly hungover curled up on the couch, regretting the night before. You didn't seem to mind my perishing state and joined the seating area (end of said couch) to do some work. Luckily that sight didn't affect our years of collaborations to come. Thank you also to Kate for hiring me and for leading

the successful field campaign in Greenland. Together with Clint, Kate, and Silje we formed a well-functioning (almost entirely female!) team and shared many cold, sometimes surprisingly warm, moments in the middle of nowhere. The fieldwork in Greenland was a memorable experience I will always carry with me.

I would like to thank my colleagues at CEED (especially Valentina, Ági, Petter, Madeleine, Annique, Sara, and Liz) for the countless lunch and coffee breaks, the Norwegian language tests, fun times at conferences, CEED trips to mines and places with rocks, and boat party dancing outings. Even though half of the time I don't know what you are all talking about (referring to rocks), everyone at CEED is very welcoming, and I am very thankful for the work environment. Special shout-out to my office mate Ági for putting up with my habit of opening the window for my after bicycle commute cool-down, no matter the weather.

I would like to thank the ASPECT community. The code developers and maintainers are always ready to help, and they taught me a lot regarding version control and good coding practises. Most contact with the community has been online, apart from an in-person meeting at AGU. Last year on my way to attend my third hackathon (and first time in-person), I really messed up with misplacing my passport somewhere in between Oslo and Frankfurt airport. Maybe fourth time is a charm? I would like to thank INACH and Professor Raúl Cordero for giving me the opportunity to perform atmospheric fieldwork on Isla Rey Jorge in Antarctica, and all the amazing Chilenos and foreign scientists for the fun times we had together. I would like to thank the APECS community for connecting so many people within Norway, but also worldwide, with a general interest in polar sciences, and the PhD research school CHESS for connecting me with Norway based scientists with similar interests in climate dynamics. The annual meetings were very resourceful, and who doesn't like to discuss climate change while sailing past snowy Norwegian fjords? Also thank you to the PhD research school DEEP, for their PhD short courses on anything related to Earth, and for their financial support to spend nearly two months on Svalbard to learn about seismics in the arctic. Blowing up explosives on glaciers was literally a blast, and I am still blown away by the natural beauty I feel privileged to have witnessed.

I would like to thank Arctic Frontiers for giving me the once in a lifetime opportunity to participate in a royal roundtable discussion on arctic sustainability with eight young Norwegian and Dutch professionals who have a strong relation to the Arctic. The event took place in my favorite museum on the deck of the Fram, which is an arctic exploration vessel used by the greatest Norwegian polar explorers and scientists Fridtjof Nansen, Otto Sverdrup, and Roald Amundsen, in the Arctic and Antarctic. We were joined at the discussion table by their majesties King Harald & Queen Sonja of Norway, and King Willem-Alexander & Queen Máxima of the Netherlands. We shared our perspectives on the future of the Arctic, the preservation of arctic diversity, and the role of science and cooperation in a sustainable future. It was very rewarding to see the royals actively engaged in the conversation.

I believe that life is so much more than work, and there are countless of people I would like to thank with whom I have shared so many great experiences with in Norway. My dear friend Marie, we are there for each other through thick and thin, and I cannot imagine how my time in Norway would have been if we hadn't met (although that is an unlikely scenario with all interests we share). I am beyond thrilled to go to Greenland with you, and for all the fun and sometimes less fun times ahead! Ivar, my first friend when I came to Oslo, I am happy you enjoy my company because there is really nothing I can teach you in return when it comes to *friluftsliv*. Thank you for making ultra running sound like a good idea and for believing in my physical abilities when it comes to literally any sport without me having any experience. You took me on my first ski touring trip, my first multi-pitch trad climb, my first winter camping fjellski adventure, and you encouraged me to run further than I thought I was capable of. Madison and Ibrahim, you are the loveliest bunch of people and you are so funny together (also individually). Please cook one of your delicious meals for me soon, and I hope you don't mind dragging me up another rock wall, because I am exited for a spring skiing and climbing trip with you this season.

My (ex-)housemates in Oslo, Frøya, Lars Erik, Marie, David, and especially the ones who keep coming back, thank you for making our home feel like a home. My (mostly) Dutch-Norwegian crew, Erik, Maria, Tiemen, Cathinka, Martijn, Manon, Ralph, Simone, Tim, Marie, thank you for the many drinks and dances in cabins we shared, and days like the winter triathlons. You are such warm and fun people! John, thank you for introducing me to beer brewing (can you help with all the brewing for my defense party?). I enjoy spending time with you and your endless waterfall of thoughts. My badminton team, thank you for spending weekends together in sports halls all over Norway and in tiny Airbnb's, often with mixed performances, but that doesn't bring us down! A community I am very happy to be a part of is the Mikkeller Running Club. You gave me structure and purpose in times when we were limited in our movement. I found a new sport I love, plus countless friends who like to crawl through the mud and drink a good beer after exercise.

My close friends back home, Caroline, Jasmijn, Anouk and Maaike, we may not have seen or spoken to each other as often as we wished, but although we live in other countries, you were never out of mind. I think we should plan some more city trips together because I'm running out of cheese. Last but not least, my family. My brother Niels and his fiancé Danitsja, and my parents Frans and Francine. Thank you for your love, our weekly calls, your open doors when I come over, for supporting my choice to live abroad, and for always accepting when I didn't want to talk about my PhD. Because, let's be fair, it's not always sunshine and rainbows.

Maaike Francine Maria Weerdesteijn
Oslo, May 2023

Summary

The redistribution of past and present ice and ocean loading on Earth's surface causes solid earth deformation and geoid changes, known as glacial isostatic adjustment (GIA). The solid earth deformation is controlled by elastic and viscous material parameters of the lithosphere and mantle. It is commonly thought that GIA deformations result from a combination of a viscous response to historic ice load changes (i.e., ice age melting), and an elastic response to ice melting due to current climate change. The GIA response is captured by modern geodetic measurements from, e.g., satellite gravimetry, altimetry, tide gauges, and GNSS (Global Navigation Satellite System). These geodetic observations capture both the response to ice mass changes over the last glacial cycle, but also to more recent ice mass changes, accelerated by human-induced climate change. Consequently, these geodetic measurements can be corrected for the viscous response to past ice load changes, based on GIA modeling, and the remaining (assumed elastic) signal is used to constrain contemporary ice load changes. Or, these geodetic measurements can be corrected for the elastic response to contemporary ice load changes and the remaining viscous signal is used to constrain Earth material properties, such as mantle viscosity and lithospheric thickness, or ice sheet histories, also using GIA models.

However, recent studies have shown that a few regions are undergoing rapid viscous uplift on decadal or centennial timescales in response to contemporary ice melt. Such uplift is occurring in West Antarctica and southeast Greenland. Rapid uplift in these regions is commonly linked to low viscosities in the upper mantle that accelerate the viscous response to recent melting. In this case, contemporary ice melt generates not only an instantaneous elastic response, but also a viscous response on short timescales. This rapid viscous response is mixed with the other deformation components of GIA (elastic and long-term viscous), which makes it difficult to distinguish between solid earth deformation caused by historical versus contemporary ice load changes. Thus, a rapid viscous response following recent ice melt complicates studies that use GIA to infer Earth material properties, ice sheet histories, or contemporary ice load changes. Moreover, rapid viscous ground uplift can impact ice dynamics, with a potentially stabilizing effect, if the low-viscosity region is located close to an ice sheet margin, as for Antarctica and Greenland.

In order to isolate the solid earth deformation due to past and contemporary ice load changes, we need a modeling tool that functions from glacial cycle (thousands of years) to decadal timescales. Furthermore, this tool should accommodate large lateral variations in Earth rheology, requiring a numerical

tool. For this, we developed and benchmarked a new viscoelastic solid earth deformation modeling tool in ASPECT (Advanced Solver for Problems in Earth's ConvecTion). ASPECT is a modern, massively parallel, open-source finite element code originally designed to simulate convection in the Earth's mantle. We characterize the performance of solid earth deformation in ASPECT and compare solutions to TABOO, a semi-analytical code, and Abaqus, a commercial finite element code. The maximum deformation and deformation rates using ASPECT agree within 2.6% for the average percentage difference with TABOO and Abaqus on glacial cycle (∼100 kyr) and contemporary ice melt (∼100 years) timescales. This gives confidence in the performance of our new solid Earth deformation modeling tool. We also demonstrate the computational efficiency of using adaptively refined meshes and report on parallel scalability of the code. Furthermore, we demonstrate our model's performance in the presence of lateral viscosity variations in the upper mantle, which represents a first of its kind benchmark for numerical GIA codes. Our benchmarked code can now be used to investigate regional solid earth deformation rates caused by glacial loading on ice age to contemporary timescales.

We first use our new code to investigate the poorly understood role of small (∼100s km) regions of unusually low-viscosity mantle. We developed viscoelastic models with low-viscosity regions in the upper mantle, and measured the effect of these regions on solid earth uplift resulting from contemporary surface ice melt. We found viscous uplift occurring on decadal timescales above the low-viscosity region, at rates comparable to or larger than those from elastic uplift or the viscous response to ice age melting. We find that uplift rates are sensitive to the location, dimensions, and viscosity of the low-viscosity region, and that the largest uncertainty in uplift rates is likely associated with uncertainty in the low-viscosity region's horizontal extent. Our modeled uplift rates show that there is a significant reduction in rates for low-viscosity regions with a radius smaller than 300 km compared to a low-viscosity asthenospheric layer.

We then apply our code to southeast Greenland, a region that is possibly characterized by a weakened earth structure (thin lithosphere and low-viscosity upper mantle) due to the passage of Greenland over the Iceland plume over 40 Ma ago. On the coast of southeast Greenland, near the Kangerlussuaq glacier, several GNSS stations show abnormally rapid ground uplift, reflecting Earth's response to past and contemporary changes in Greenland's ice mass. Current earth deformation models, which employ a layered earth structure, cannot explain this rapid uplift. We use our new code for high resolution regional modeling of the solid Earth in response to ice mass changes over the last glacial cycle, the second millennium, and the satellite altimetry era. We find that earth models that incorporate a track of low-viscosity upper mantle and thin lithosphere can explain the rapid observed uplift in southeast Greenland. The uplift is dominated by a viscous response to rapid deglaciation occurring within the past few decades. This viscous contribution is not usually considered in GIA models, but will become increasingly important in the future as deglaciation accelerates.

Sammendrag

Omfordelingen av tidligere og nåværende is- og havbelastning på jordens overflate forårsaker deformasjon av den faste jorden og dens geoide. Dette er kjent som *glacial isostatic adjustment* (GIA). Deformasjon av den faste jorden styres av elastiske og viskøse materialparametre i litosfæren og mantelen. Det er vanlig å tro at GIA deformasjoner skyldes en kombinasjon av en viskøs respons fra historiske isbelastningsendringer (dvs. istidssmelting), og en elastisk respons fra issmelting på grunn av nåværende klimaendringer. GIA-responsen fanges opp av moderne geodetiske målinger fra f.eks. satellittgravimetri, altimetri, tidevannsmålere og GNSS (Global Navigation Satellite System). Disse geodetiske observasjonene fanger både responsen på ismasseendringer i løpet av den siste bresyklusen, men også på nyere ismasseendringer akselerert av menneskeskapte klimaendringer. Følgelig kan disse geodetiske målingene korrigeres for den viskøse responsen på tidligere islastendringer, basert på GIA modeller, og det gjenværende (antatt elastiske) signalet brukes til å begrense moderne islastendringer. Videre kan disse geodetiske målingene korrigeres for den elastiske responsen på moderne isbelastningsendringer, og det gjenværende viskøse signalet brukes til å begrense jordmaterialegenskapene, slik som mantelviskositet og litosfærisk tykkelse, eller isarkhistorier, også ved bruk av GIA modeller.

Nyere studier har imidlertid vist at noen få regioner gjennomgår rask viskøs landhevning på tiår eller hundre år som svar på moderne issmelting. Slik hevning skjer i Vest-Antarktis og Sørøst-Grønland. Rask landhevning i disse regionene er ofte knyttet til lave viskositeter i den øvre mantelen som akselererer den viskøse responsen på nylig smelting. I dette tilfellet genererer moderne issmelting ikke bare en øyeblikkelig elastisk respons, men også en viskøs respons på korte tidsskalaer. Denne raske viskøse responsen er blandet med de andre deformasjonskomponentene i GIA (elastisk og langtidsviskøs), noe som gjør det vanskelig å skille mellom deformasjon av den faste jorden forårsaket av historiske versus moderne islastendringer. En rask viskøs respons etter nylig issmelting kompliserer studier som bruker GIA for å utlede jordmaterialeegenskaper, isdekkehistorier eller moderne isbelastningsendringer. Dessuten kan rask viskøs landhevning påvirke isdynamikken, med en potensielt stabiliserende effekt, hvis den lavviskøse regionen ligger nær en isdekkekant, slik som for Antarktis og Grønland.

For å isolere deformasjonen av den faste jorden grunnet tidligere og samtidige islastendringer, trenger vi et modelleringsverktøy som fungerer fra issyklusen (tusenvis av år) til dekadale tidsskalaer. Videre bør dette verktøyet imøtekomme store laterale variasjoner i jordreologi, noe som krever et numerisk verktøy. For

dette utviklet og benchmarket vi et nytt viskoelastisk deformasjonsmodelleringsverktøy for den faste jorden i ASPECT (Advanced Solver for Problems in Earth's ConvecTion). ASPECT er en moderne, parallell, åpen kildekode med endelig elementkode opprinnelig designet for å simulere konveksjon i jordens mantel. Vi karakteriserer ytelsen til deformasjonen av den fasten jorden i ASPECT og sammenligner løsninger med TABOO, en semi-analytisk kode, og Abaqus, en kommersiell endelig elementkode. De maksimale deformasjons og deformasjonsrater ved bruk av ASPECT stemmer overens innenfor 2.6% for den gjennomsnittlige prosentvise forskjellen med TABOO og Abaqus på issyklus (∼100 kyr) og moderne issmelting (∼100 år). Dette gir tillit til ytelsen til vårt nye modelleringsverktøy. Vi demonstrerer også beregningseffektiviteten ved å bruke adaptivt raffinerte mesh og rapporterer om parallell skalerbarhet av koden. Videre demonstrerer vi modellens ytelse når det er laterale viskositetsvariasjoner i den øvre mantelen, som er første i sitt slag for numeriske GIA koder. Vår benchmarket kode kan nå brukes til å undersøke regionale deformasjonsrater for den faste jorden forårsaket av isbelastning fra istid til moderne tidsskalaer.

Vi bruker først vår nye kode for å undersøke den dårlig forståtte rollen til små (∼100s km) regioner med uvanlig lavviskøs mantel. Vi utviklet viskoelastiske modeller med lavviskositetsområder i den øvre mantelen, og målte effekten av landhevning i disse områdene som følge av moderne issmelting på overflaten. Vi fant at landhevning skjedde på tiårlige tidsskalaer over lavviskositetsområder med hevningsrater som er sammenlignbare med eller større enn de fra elastisk landhevning eller den viskøse responsen fra istidssmelting. Vi finner at hevningsrater er følsomme for plasseringen, dimensjonene og viskositeten til lavviskositetsregionen, og at den største usikkerheten i hevningsrater sannsynligvis er forbundet med usikkerhet i lavviskositetsregionens horisontale utstrekning. Våre modellerte landhevningsrater viser at det er en betydelig reduksjon i rater for lavviskositetsområder med en radius mindre enn 300 km sammenlignet med et lag av lav viskositet i astenosfæren.

Vi bruker deretter koden vår på Sørøst-Grønland, en region som muligens er preget av en svekket jordstruktur (tynn litosfære og lavviskøs øvre mantel) grunnet Grønland sin forflytning over Island-varmesøylen for over 40 millioner år siden. På kysten av Sørøst-Grønland, nær Kangerlussuaq breen, viser flere GNSS stasjoner unormalt rask landhevning, noe som gjenspeiler den faste jordens respons på tidligere og samtidige endringer i Grønlands ismasse. Deformasjonsmodeller av den faste jorden som bruker en lagdelt jordstruktur kan ikke forklare denne raske hevningen. Vi bruker vår nye kode for høyoppløselig regional modellering av den faste jorden som svar på ismasseendringer i løpet av den siste issyklusen, det andre årtusenet og satellittmålingstiden. Vi finner at jordmodeller som inkorporerer et spor av lavviskøs øvre mantel og tynn litosfære kan forklare den raske observerte landhevningen på Sørøst-Grønland. Hevningen er dominert av en viskøs respons på rask deglasiasjon som har skjedd i løpet av de siste tiårene. Dette viskøse bidraget vurderes vanligvis ikke i GIA modeller, men vil bli stadig viktigere i fremtiden ettersom deglasiasjonen akselererer.

Samenvatting

De herverdeling van vroegere en huidige ijs- en oceaanbelasting op het aardoppervlak veroorzaakt vervorming van de aarde en geoïde veranderingen, bekend als *glacial isostatic adjustment* (GIA). De aardvervorming wordt bepaald door elastische en viskeuze materiaal parameters van de lithosfeer en bovenmantel. Over het algemeen wordt aangenomen dat GIA deformaties het gevolg zijn van een combinatie van een viskeuze reactie op historische veranderingen in de ijsmassa (d.w.z. het smelten gedurende de laatste ijstijd) en een elastische reactie op het smelten van ijs als gevolg van huidige klimaatveranderingen. De GIA-respons wordt gemeten door moderne geodetische technieken van bijvoorbeeld satelliet gravimetrie, altimetrie, getijdenmeters en GNSS (Global Navigation Satellite System). Deze geodetische waarnemingen leggen zowel de reactie vast op veranderingen in de ijsmassa tijdens de laatste ijstijd, maar ook op meer recente veranderingen in de ijsmassa, versneld door klimaatverandering. Deze geodetische metingen kunnen worden gecorrigeerd voor de viskeuze respons op veranderingen in de historische ijsmassa, op basis van GIA modellen, en het resterende (aangenomen elastische) signaal wordt gebruikt om hedendaagse veranderingen in de ijsmassa te bepalen. Of, deze geodetische metingen kunnen worden gecorrigeerd voor de elastische respons op recente ijsmassa veranderingen en het resterende viskeuze signaal wordt gebruikt om de aardmateriaaleigenschappen, zoals de viscositeit van de mantel en de dikte van de lithosfeer, of de ijsmassa geschiedenis te bepalen, ook met behulp van GIA modellen.

Recente studies hebben echter aangetoond dat een aantal gebieden een snelle viskeuze opheffing van de aarde ondergaan op tijdschalen van tien tot honderd jaar als reactie op het recente smelten van ijs. Een dergelijke opheffing vindt plaats in West-Antarctica en Zuidoost-Groenland. Snelle opheffing in deze gebieden wordt in verband gebracht met lage viscositeiten in de bovenmantel die de viskeuze reactie op recente ijssmelt versnellen. In dit geval genereert het smelten van hedendaags ijs niet alleen een onmiddellijke elastische respons, maar ook een viskeuze respons op korte tijdschalen. Deze snelle viskeuze reactie is gemengd met de andere aardvervormingscomponenten van GIA (elastische en langdurige viskeuze), waardoor het moeilijk is om onderscheid te maken tussen aardvervorming veroorzaakt door historische versus hedendaagse ijsmassaveranderingen. Een snelle viskeuze reactie na recente ijssmelt bemoeilijkt dus studies die GIA gebruiken om aardmateriaaleigenschappen, ijskapgeschiedenissen of hedendaagse veranderingen in de ijsbelasting af te leiden. Bovendien kan een snelle viskeuze opheffing van de grond de ijsdynamiek beïnvloeden, met een mogelijk stabiliserend effect, als het laagviskeuze gebied dicht bij een ijskaprand ligt, zoals voor Antarctica en Groenland.

Om de aardvervorming als gevolg van veranderingen in de ijsbelasting in het verleden en heden te isoleren, hebben we een modelleringstool nodig die functioneert van glaciale cyclus (duizenden jaren) tot tienjarige tijdschalen. Bovendien moet deze tool grote laterale variaties in de reologie van de aarde kunnen opvangen, waarvoor een numerieke tool nodig is. Hiervoor hebben we een nieuwe visco-elastische aarddeformatietool ontwikkeld en gebenchmarkt in ASPECT (Advanced Solver for Problems in Earth's ConvecTion). ASPECT is een moderne, parallelle, open-source eindige-elementencode die oorspronkelijk is ontworpen om convectie in de aardmantel te simuleren. We tonen de prestaties van aarddeformatie in ASPECT en vergelijken oplossingen met TABOO, een semi-analytische code, en Abaqus, een commerciële eindige-elementencode. De maximale vervorming en vervormingssnelheden in ASPECT komen binnen 2.6% overeen voor het gemiddelde procentuele verschil met TABOO en Abaqus op de tijdschalen van de ijstijd (∼100 kyr) en het hedendaagse smelten van ijs (∼100 jaar). Dit geeft vertrouwen in de prestaties van onze nieuwe modelleringstool voor aarddeformatie. We demonstreren ook de efficiëntie van het gebruik van dynamische meshes en rapporteren over parallelle schaalbaarheid van de code. Bovendien demonstreren we de prestaties van ons model in de aanwezigheid van laterale viscositeitsvariaties in de bovenmantel, wat een eerste in zijn soort is voor numerieke GIA codes. Onze gebenchmarkte code kan nu worden gebruikt om regionale aarddeformatie te onderzoeken die wordt veroorzaakt door glaciale belasting op ijstijd tot hedendaagse tijdschalen.

We gebruiken eerst onze nieuwe code om de slecht begrepen rol van kleine (∼100s km) gebieden met een ongewoon lage viscositeit bovenmantel te onderzoeken. We ontwikkelden visco-elastische modellen met gebieden met een lage viscositeit in de bovenmantel en maten het effect van deze gebieden op de opwaartse beweging van de aarde als gevolg van het hedendaagse smelten van ijs aan het oppervlak. We vinden viskeuze opheffing die plaatsvindt op tienjarige tijdschalen boven het gebied met lage viscositeit, met snelheden die vergelijkbaar zijn met of groter zijn dan die van elastische opheffing of de viskeuze reactie op het smelten van de ijstijd. We vinden dat opwaartse snelheden gevoelig zijn voor de locatie, afmetingen en viscositeit van het gebied met lage viscositeit, en dat de grootste onzekerheid in opwaartse snelheden waarschijnlijk verband houdt met onzekerheid in de horizontale omvang van het gebied met lage viscositeit. Onze gemodelleerde opwaartse snelheden laten zien dat er een significante verlaging van de snelheden is voor gebieden met een lage viscositeit met een straal kleiner dan 300 km in vergelijking met een asthenosferische laag met een lage viscositeit.

Vervolgens passen we onze code toe op Zuidoost-Groenland, een regio die mogelijk wordt gekenmerkt door een verzwakte aardstructuur (dunne lithosfeer en lage viscositeit bovenmantel) als gevolg van de overgang van Groenland over de IJslandse mantelpluim meer dan 40 miljoen jaar geleden. Aan de kust van Zuidoost-Groenland, in de buurt van de Kangerlussuaq gletsjer, meten verschillende GNSS stations een abnormaal snelle opheffing van de aarde, wat

de reactie van de aarde op veranderingen in de ijsmassa in het verleden en nu weerspiegelt. De huidige aarddeformatiemodellen, die een gelaagde aardstructuur gebruiken, kunnen deze snelle opheffing niet verklaren. We gebruiken onze nieuwe code voor regionale, hoge resolutie, modellering als reactie op veranderingen in de ijsmassa tijdens de laatste ijstijd, het tweede millennium en het tijdperk van satellietmetingen. We vinden dat aardmodellen die een spoor van laag viscositeit bovenmantel en dunne lithosfeer bevatten, de snelle waargenomen opheffing in Zuidoost-Groenland kunnen verklaren. De opheffing wordt gedomineerd door een viskeuze reactie op snelle deglaciatie die zich de afgelopen decennia heeft voorgedaan. Deze viskeuze bijdrage wordt gewoonlijk niet overwogen in GIA modellen, maar zal in de toekomst steeds belangrijker worden naarmate de deglaciatie versnelt.

List of Papers

Paper I

Weerdesteijn, Maaike F. M., Naliboff, John B., Conrad, Clinton P., Reusen, Jesse M., Steffen, Rebekka, Heister, Timo, and Zhang, Jiaqi. (2023). Modeling Viscoelastic Solid Earth Deformation Due To Ice Age and Contemporary Glacial Mass Changes in ASPECT. *Geochemistry, Geophysics, Geosystems*, 24 , e2022GC010813. 10.1029/2022GC010813

Paper II

Weerdesteijn, Maaike F. M., Conrad, Clinton P., and Naliboff, John B. (2022). Solid Earth Uplift Due To Contemporary Ice Melt Above Low-Viscosity Regions of the Upper Mantle. *Geophysical Research Letters*, 49, e2022GL099731. 10.1029/2022GL099731

Paper III

Weerdesteijn, Maaike F. M., and Conrad, Clinton P. (in preparation). Rapid Earth uplift in southeast Greenland driven by recent ice melt above low-viscosity upper mantle.
In manuscript stage, and will be submitted to *Science Advances*.

Contents

Preface iii

Acknowledgements v

Summary ix

Sammendrag xi

Samenvatting xiii

List of Papers xvii

Contents xix

1 Introduction 1
- 1.1 History of Glacial Isostatic Adjustment Research 1
- 1.2 Modern field of Glacial Isostatic Adjustment 7
- 1.3 Lateral variations in Earth's structure 13
- 1.4 3D Glacial Isostatic Adjustment Modeling Codes 17
- References 19

2 Conclusions and outlook 29
- 2.1 Summary of main results 30
- 2.2 Limitations and future directions 33
- References 35

Papers 40

I Modeling Viscoelastic Solid Earth Deformation Due To Ice Age and Contemporary Glacial Mass Changes in ASPECT 41
- I.1 Introduction 43
- I.2 Numerical Model 44
- I.2.1 Constitutive Equations 45
- I.2.2 Viscoelastic Rheology 46
- I.2.3 Boundary Conditions 48
- I.2.4 Solver Options 48
- I.3 Benchmark Study: Short and Long Timescales 49
- I.3.1 Reference Models 49
- I.3.2 Test Setup 50
- I.4 Benchmark Results and Model Performance 53

I.4.1 Short Timescale Simulation 53
I.4.2 Long Timescale Simulation 54
I.4.3 Model Performance 56
I.5 Benchmark Variations: Adaptive Mesh Refinement and Lateral Heterogeneous Viscosity 58
I.5.1 Adaptive Mesh Refinement 58
I.5.2 Lateral Heterogeneous Viscosity 60
I.6 Scaling and Material Averaging 62
I.7 Conclusion 64
Appendix A: Model Horizontal Dimension 66
Appendix B: Sphericity and Self-Gravitation 68
Appendix C: Model Density 69
References 71

II Solid Earth Uplift Due To Contemporary Ice Melt Above Low-Viscosity Regions of the Upper Mantle 79
II.1 Introduction 80
II.2 Modeling Deformation Near a Low-Viscosity Region: 1D Versus 3D Approach 82
II.3 Sensitivity of Deformation to Low-Viscosity Region Characteristics 85
II.3.1 Low-Viscosity Region Thickness 87
II.3.2 Low-Viscosity Region Radius 87
II.3.3 Low-Viscosity Region Depth 87
II.3.4 Low-Viscosity Region and Ice Load Distance 87
II.3.5 Ice Load Radius 87
II.3.6 Low-Viscosity Region Viscosity 88
II.4 Discussion 88
II.4.1 Factors Affecting Uplift From Contemporary Ice Melt . 88
II.4.2 Importance of Contemporary Ice Melt for Greenland Uplift 89
II.4.3 1D Versus 3D Modeling for Greenland 89
II.4.4 Ice Sheet and Glacier Dynamics 90
II.5 Conclusion 91
Supporting Information S1 92
References 94

III Rapid Earth uplift in southeast Greenland driven by recent ice melt above low-viscosity upper mantle 101
III.1 Introduction 101
III.2 Results 102
III.2.1 GNSS uplift rates 104
III.2.2 Global modeling of last glacial cycle ice mass changes . . 105
III.2.3 Greenland modeling of Earth's elastic response to satellite altimetry era ice mass changes 106
III.2.4 Regional modeling of last glacial cycle ice mass changes 106
III.2.5 Regional modeling of satellite altimetry era ice mass changes 108

III.2.6 Regional modeling of second millennium ice mass changes 108
III.2.7 Total vertical surface displacement rates in southeast Greenland and the GNSS sites 109
III.3 Discussion 114
III.3.1 On the preferred earth structure 114
III.3.2 Viscous response of the solid earth to contemporary ice loading changes 114
III.3.3 Large variations in uplift rate during the last glacial cycle 115
III.3.4 Uplift rates at PLPK and KSNB 115
III.3.5 Complex rheologies 116
III.4 Material and Methods 117
III.4.1 Regional solid earth deformation modeling in ASPECT . 117
III.4.2 Global solid earth deformation modeling in SELEN . . . 118
III.4.3 Greenland modeling of elastic response 118
III.4.4 Earth structure and variations 118
III.4.5 Ice loading changes for model input 119
III.4.6 GNSS uplift rates 120
Supplementary Materials 121
References 138

Chapter 1

Introduction

Mass redistributions on the Earth's surface cause the Earth to deform due its viscoelastic nature, and its gravitational field to change, both affecting sea level. The response of the solid Earth, the oceans, and Earth's gravitational field to mass changes from the global ice sheets, is known as glacial isostatic adjustment (GIA). The Earth is still responding to past changes in ice sheets over the last glacial cycle, but also to contemporary ice melt. One component of GIA, the land uplift following ice sheet melt or "postglacial rebound", has been a long-studied field. The first findings of the Earth's response to melting ice sheets and how this developed to form our understanding of postglacial rebound and the Earth as a viscoelastic body is described in Section 1.1, and Section 1.2 describes how this work led to the modern field of GIA. Section 1.3 discusses lateral heterogeneities within the Earth and how these affect GIA. GIA modeling codes and developments are covered in Section 1.4. These concepts form the foundation of the research described in the rest of the thesis.

1.1 History of Glacial Isostatic Adjustment Research

The history of land uplift in this section is based on the work of Martin Ekman, who has done a fantastic job collecting documents, observations, and theories of the level of the Baltic Sea (Ekman, 2009), and whom I have had the pleasure to meet during the Glacial Isostatic Adjustment Training School 2019 in Gävle, Sweden. For a more elaborate overview of the history of land uplift around the Baltic Sea I refer to his extensive work in Ekman (2009).

The oldest documented observation of land uplift is a resolution from 1491 by the Swedish government to relocate the fishing town Östhammar, located between Stockholm and Gävle at the Gulf of Bothnia. Fishing boats could not enter the town's harbor any longer where previously cargo boats could go. The resolution describes that "(...) the land is still growing and rising every year." The conclusion that the land was rising, was beyond the available knowledge at the time, as instead the sea level may have been falling. Between the town's erection (around 1100) and relocation (1491), the relative sea level had fallen by about 2 m, making the shallow harbor dysfunctional. Two centuries later Swedish scientist Hiärne and historian Brenner believed that it was not the land that was rising, as suggested in 1491, but the sea level that was falling. This phenomenon was observed across a large region around the Baltic sea (Östhammar was not the last town along the Swedish east coast to be relocated) and therefore could not be due to a local cause (the land), but had to be due to a cause spanning a wider region (the sea). They explained that water entering

the Gulfs of Bothnia and Finland through rivers caused the sea level to be higher in the past. The water was now flowing into the North Sea, causing erosion and widening of the outlet.

Swedish astronomer and geodesist Celsius, known for the temperature scale, also believed in the general water decrease in the Baltic Sea, and was the first person to compute the rate of sea level fall (Celsius, 1743). He made use of documents on the ownership of an abandoned seal rock, which are rocks in the sea on which seals could rest, used by seal hunters. The rock tops had to be close to the mean sea level for the seal to get on top and for the seal to be largely out of the water. These seal rocks were valued in inheritance documents and bills of sale, and sometimes declared unusable when they were too high above the sea level to be worth anything. One seal rock was of particular importance because it could be identified and measured based on the available documentation (Figure 1.1 (Celsius, 1743; Ekman, 2009)).

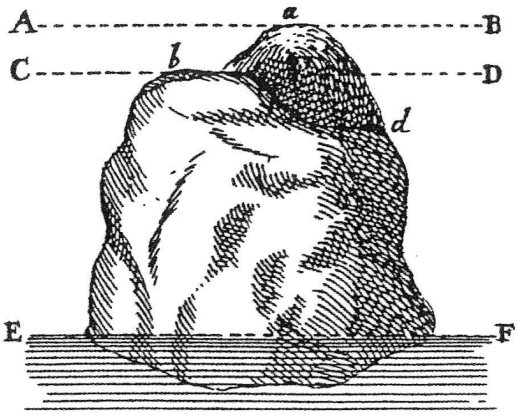

Figure 1.1: A sketch of the abandoned seal rock, with different plateaus on which seals could rest, on which the first measurements of land uplift or sea level fall were based. (Celsius, 1743). See Ekman (2016) for depictions of the letters based on a description from Celsius.

Celsius found a sea level fall rate of 1.4 cm/yr, which is 60% larger than estimates based on modern methods of 0.8 cm/yr. He explained the sea level fall as being due to either sea water evaporation that after precipitation did not all return to the Baltic Sea but instead was consumed by plants, or sea water disappearing through holes on the sea floor. Celsius cut a mean sea level mark in 1731 into a seal rock of an island near the coast of Gävle (Figure 1.2 (Ekman, 2016)) “in order to make future generations able to determine this rate of change more accurately”.

Swedish botanist Linnaeus and physicist Gissler supported Celsius’ ideas, based on the ridges they observed parallel to the coast, which were interpreted as old shorelines that lost contact with the sea because of the water decrease.

Figure 1.2: The Celsius seal rock at the island of Lövgrunden in the Gulf of Bothnia of the coast of Gävle with mean sea level marks from 1731, 1831, and 1931. (Ekman, 2016).

Opposition was met with Swedish-Finnish land surveyor Runeberg and Swedish astronomer Ferner who believed that the land was rising, based on bedrock structure observations in mines that indicated bedrock movement. Scottish mathematician Playfair was also in favor of the land uplift theory, as he believed that it was more likely for the land to change regionally than for the sea. Another theory was put forward by Italian mathematician Frisi, who did not think land uplift was likely because of the lack of earthquakes. Instead he explained the sea level fall by the cooling and contracting of the Earth, leading to an increase in Earth's rotational speed, and thereby a flattening of the sea surface at more northern latitudes.

Two decades after Celsius' 1731 mark on the Celsius rock, multiple marks were erected on rocks around the Baltic Sea. These sea level marks proved to be valuable in monitoring the sea level. Finnish-Swedish geodesist Hällström published a table of sea level change rates based on these sea level marks, and Swedish chemist Berzelius concluded from these tables that the land was rising. He believed, similar to Frisi, that the Earth was cooling and contracting, but unlike Frisi, that this would cause land uplift around the Baltic Sea because this contraction would force the Earth's crust to deform. English geologist Lyell performed a study to find the deviation of the instant sea level from the mean sea level and found a sea level change rate of 8.3 mm/yr from the sea level marks at the Celsius rock, only 10% larger than estimates based on modern methods. Lyell also found no relative sea level change on the Swedish south coast, meaning there could be no general water decrease in the Baltic Sea. There were also no conclusive findings on a latitude-dependent sea level change as proposed by Frisi, favoring the theory of regional land uplift. The cause of the

land uplift, however, still remained unknown. Lyell proposed that the land uplift was caused by internal heating of the Earth and therefore expansion of the crust. Previously, Berzelius suggested land uplift due to cooling and contracting of the Earth, whilst Frisi thought that this cooling and contracting would cause a sea level fall.

Danish-Norwegian geologist Esmark found that mountain glaciers could create large moraines and transport large erratic boulders. He thought that Norway must have been covered by ice, because the erratics and moraines were found all over Norway. Swiss zoologist Agassiz went a step further and introduced the idea that large parts of Europe and the northern hemisphere were covered by ice during the "Ice Age", based on the erratics and moraines found in the Alps. In 1859 Swedish geologist and polar explorer Torell supported the idea of complete glaciation of the Nordic countries, based on geological findings in Iceland, Greenland, and Svalbard. French mathematician Adhémar and British geophysicist Croll explained the repeating occurrence of ice ages due to periodical variations in Earth's orbit. This theory was 100 years later elaborated on by Serbian geophysicist Milankovitch, and these orbital variations in eccentricity, obliquity (or axial tilt), and precession are now known as the Milankovitch cycles (Figure 1.3. (Maslin, 2016)).

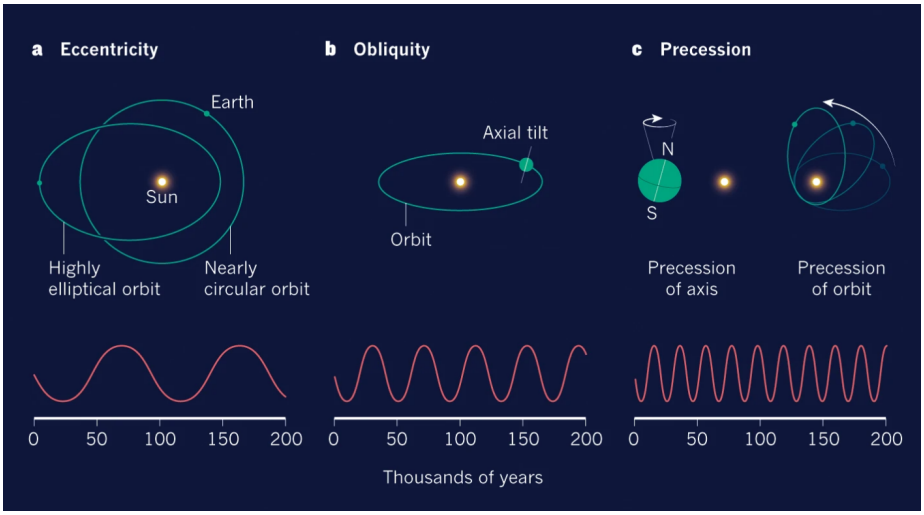

Figure 1.3: (a) Eccentricity describes the shape of Earth's orbit around the Sun, and varies from being almost a circle to a more elliptical shape, with a period of about 96,000 years. (b) Obliquity is the tilt of Earth's axis of rotation with respect to the plane of its orbit, and it oscillates with a period of about 41,000 years. (c) Both Earth's rotational axis and its orbital path precess over time — the combined effects of these two components and the eccentricity produce an approximately 21,000-year cycle. (Maslin, 2016).

British geologist Jamieson was the first to introduce the concept of what we now know as "postglacial rebound" as he wrote in 1865 "In Scandinavia and North America, as well as in Scotland, we have evidence of a depression of the land following close upon the presence of the great ice-covering. It has occurred to me that the enormous weight of ice thrown upon the land may have had something to do with this depression. Then the melting of the ice would account for the rising of the land, which seems to have followed upon the decrease of the glaciers." However, postglacial rebound did not become a widely accepted idea as it requires thick ice and a "fluid" Earth. Most geologists would accept the fluid Earth part but did not believe in large climate changes due to an astronomical cause (i.e., ice ages due to Milankovitch cycles). By contrast, most geophysicists would accept the ice ages, but believed that the Earth was solid based on the existence of solid Earth tides.

A map of land uplift could shed more light on the still unknown cause of the uplift. However, such map was not created due to lack of knowledge of how long-term sea level variations in the Baltic Sea affect the sea level marks. The locations of the sea level marks also did not allow for regular readings. Around 1850, this lead to the establishment of sea level scales at light houses and pilot stations along the Swedish and Finnish coasts, where the uplift rate was found through linear regression of annual sea level means, already used by Finnish-Swedish polar explorer Nordenskiöld to characterize the Stockholm sea level series. The disadvantage of these scales was that they were not fixed to the bedrock and therefore less stable. Continuous sea level observations were recorded at mareographs starting around 1890. Mareographs use sea level gauges that automatically record, without having to read the observations as for the sea level scales.

Figure 1.4: Raised beach north of Gävle, Sweden. This old shoreline is now raised over 200 m above the current sea level. Photo by Maaike F. M. Weerdesteijn.

Meanwhile Swedish geologist De Geer invented another method to measure land uplift since the last glacial maximum. De Geer mapped the highest shorelines (Figure 1.4), also known as the marine limit, and assumed that they were approximately the same age as the end of the last deglaciation (Figure 1.5 (de Geer, 1888)). Based on this map, De Geer found that the land uplift area overlaps with the glaciation area, and that the area of maximum uplift matches with the maximum ice thickness area. De Geer findings pointed towards postglacial rebound caused by ice unloading as the cause of the land uplift. He continued developing the maps along with Swedish geotechnician Lidén by dating the raised beaches based on annually deposited clay layers. They found that the uplift had been over 10 times faster at the start of the deglaciation compared to the current rate, and that the uplift rate decayed exponentially. This method did not take into account sea level rise caused by the ice melt.

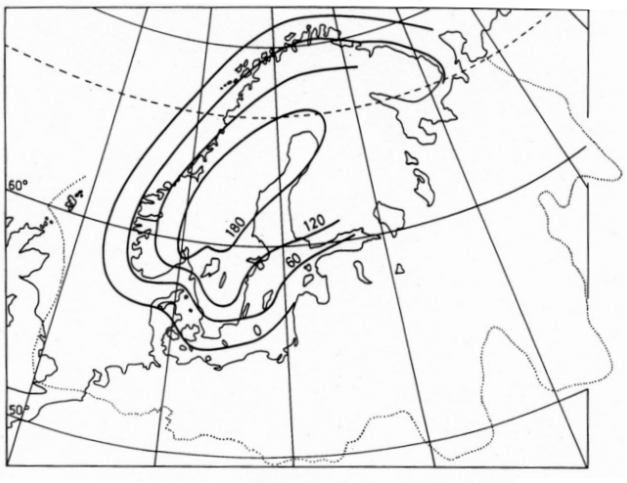

Figure 1.5: Land uplift map based on the height (m) of the marine limit. Redrawn from De Geer (1888). Ekman (2016).

It was now confirmed that the land was rising, and not the sea level falling, that this rebound is due to the melting of an extensive ice cover, and that the uplift rate following the last deglaciation is not linear. The next questions to be answered related to the properties of Earth's interior. British physicist Lord Kelvin and geophysicist Darwin were in favor of a solid Earth, as they argued that the Earth had to be rigid for long-period tides to exist. Norwegian oceanographer and polar explorer Nansen believed in a more fluid Earth, where earth material underneath the crust viscously flows to the area of deglaciation, and thereby changing the local gravity (Figure 1.6 (Nansen, 1921)). British geophysicist and geologist Holmes used the idea of viscous mantle flow to explain the theory of moving continents from the German geophysicist Wegener, suggesting that the flow is driven by convective currents within the Earth's

mantle.

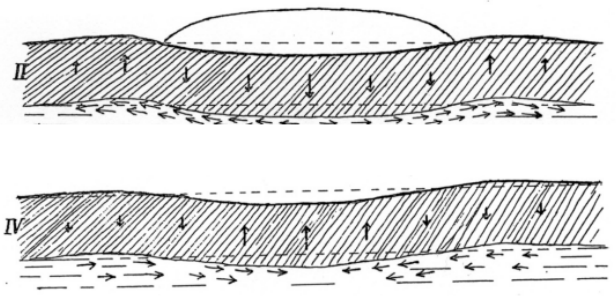

Figure 1.6: Changing ice load and viscous flow of mantle material. (Nansen, 1921).

Dutch geophysicist and geodesist Vening Meinesz took gravity measurements on the sea, which showed gravity anomalies he believed to be caused by mantle flow. He was the first person to determine the viscosity (i.e., resistance to flow) of the Earth's mantle, by using the land uplift from sea level recordings around the Gulf of Bothnia and estimations of remaining uplift based on negative gravity anomalies, resulting in a mantle viscosity estimate of $4{\cdot}10^{21}$ Pa s. American geophysicist Haskell used a similar approach as Vening Meinesz, but used both uplift data from the centre of the uplift region as well as on the periphery to estimate a mantle viscosity of 10^{21} Pa s, a value that is still widely accepted as average mantle viscosity. Now that a viscosity had been found, meaning the Earth is viscous, how about the theory that the Earth has to be rigid enough for the existence of tides? Both theories are correct: the Earth is viscous when subject to forces of long duration (e.g., ice loading) and elastic when subject to forces of short duration (e.g., tidal forcing), thus the Earth is a viscoelastic body.

1.2 Modern field of Glacial Isostatic Adjustment

Here, we make a jump in time from the finding of postglacial rebound, existence of ice ages, and Earth as a viscoelastic body, to the modern field of glacial isostatic adjustment (GIA). As mentioned earlier, GIA encompasses not only the response of the solid Earth to ice mass changes, but the response of the solid Earth, oceans, and Earth's gravitational field to mass changes from the global ice sheets (Fig. 1.7 (Whitehouse, 2018)). Note that with "solid" we do not refer to the Earth as a rigid body as in the previous section. Thus, next to the ice and earth, GIA also includes changes in the gravitational field and to the oceans. In 1882, German geographer Penck already considered the gravitational attraction of the ice on the ocean water. He used it to explain the theory of regional water decrease, because the effect of the decrease in gravitational attraction of ocean water to the ice would be larger than the water increase in the ocean basin following the ice melt.

The regional water decrease theory, as opposed to land uplift, was incorrect, but the gravitational attraction of the ice on the ocean water is an important component in GIA, and shows itself in the meltwater fingerprint (e.g., Conrad & Hager, 1997; Mitrovica et al., 2001; Tamisiea et al., 2001; Coulson et al., 2022).

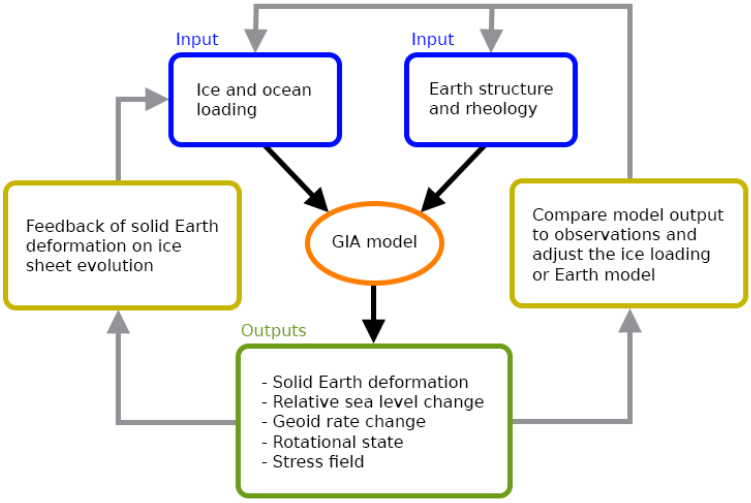

Figure 1.7: Schematic overview of forward GIA modeling. Model inputs are ice and ocean loading, and Earth structure and rheology. Model outputs are solid earth deformation, relative sea level change, geoid rate change, Earth's rotational state, and the stress field in the Earth's crust. Solid earth deformation can affect ice sheet evolution and therefore feeds back into the ice loading input. Model outputs are compared to modern geodetic observations, followed by tuning of the model inputs to improve the model fit. Adapted from Whitehouse (2018).

When land ice melts, the solid Earth rebounds, both on short timescales from the elastic lithosphere and on longer timescales from the viscous mantle (Figure 1.8 (Whitehouse, 2018; Conrad, 2013)), causing a relative sea level drop. The sea level also drops in the near-field due to the decrease in gravitational attraction of the ocean water to the ice. The increase in water in the ocean basin causes a net sea level rise. Even after the ice has melted, the earth will keep rebounding. Furthermore, the forebulge will collapse (the forebulge is created when the ice mass grows and mantle material flows away from the area of glaciation). When the forebulge collapses and is located in the ocean, the volume of the ocean basin increases causing the mean sea surface height to drop. The forebulge can also be located on land, as for example, Greenland lies on the collapsing forbulge of the past Laurentide ice sheet over northern North America, causing Greenland to subside (demonstrated in Paper III).

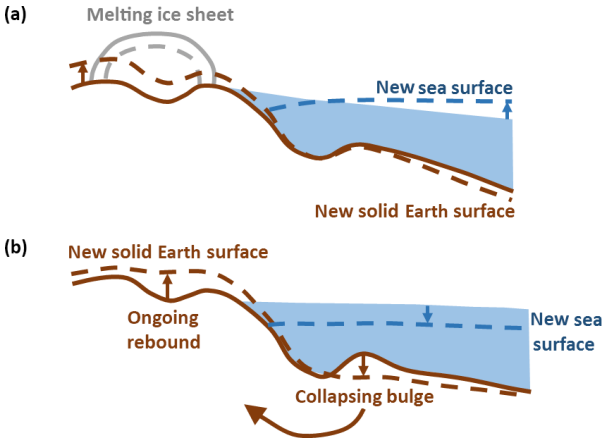

Figure 1.8: Solid earth deformation and sea level change. (a) Ice sheet losing mass results in solid earth rebound and a decrease in sea surface height due to the decreased gravitational attraction of the ice sheet, causing near-field relative sea level fall. Relative sea level rises in the far field due to the addition of meltwater to the ocean. (b) Ongoing solid earth relaxation after disappearance of the ice sheet. Ocean syphoning is the process whereby peripheral bulge subsidence increases the capacity of the ocean; the result is a fall in mean sea surface height. Solid lines indicate original positions; dashed lines indicate new positions. Figure adapted from Conrad (2013). (Whitehouse, 2018).

Meltwater from the ice sheet enters the ocean basin and is distributed across the global oceans. The mean sea level (which excludes variations from atmospheric and oceanic forcing) follows the geoid. The geoid is an equipotential surface, i.e., a surface on which the potential energy is equal, and is dependent on the distribution of mass in the Earth system (e.g., mountain ranges, density variations in the Earth's crust, ice sheets etc.). Satellite gravimetry missions CHAMP (Challenging Minisatellite Payload) (Reigber et al., 2002), GRACE and GRACE-FO (Tapley et al., 2004), and GOCE (Gravity Field and Steady-State Ocean Circulation Explorer) (Drinkwater et al., 2003) measure(d) the Earth's gravity field with a high accuracy from a low Earth orbit. The shape of the Earth's geoid resembles a potato (Figure 1.9).

The so called sea level equation solves for the gravitationally self-consistent redistribution of meltwater across the ocean (e.g., Farrell & Clar, 1976; Mitrovica & Milne, 2003), and is dependent on the geoid. Because of the dependency of the sea level on the geoid, and the dependency of the geoid on the solid earth deformation following ice melt, an iterative solving process is required to find the state of the sea level. For a realistic determination of the sea level one has to take into account shoreline migration i.e., the change in ocean area when the sea level rises or falls. Furthermore, over the last glacial cycle the ice of the larger ice sheets was not only grounded on land, but could extend into the

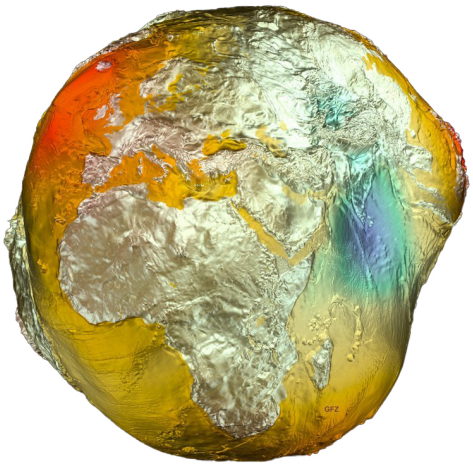

Figure 1.9: The geoid, or "Potato Earth". Image courtesy of GFZ.

oceans, either grounded (full displacement of water column) or floating (partly displacement of water column), and thereby decreasing the area over which meltwater is distributed (Mitrovica & Milne, 2003; Lambeck et al., 2003).

Another component of GIA is the rotational feedback (Mitrovica et al., 2005; Mitrovica & Wahr, 2011; Martinec & Hagedoorn, 2014). The equilibrium between centrifugal and self-gravitational forces defines the hydrostatic shape of the Earth, with an equatorial bulge (Fig. 1.10.A1, (Weerdesteijn, 2019)). GIA perturbs the Earth's moment of inertia through a redistribution of mass (here a positive mass anomaly, Fig. 1.10.A2), and causes a change in centrifugal force. To conserve angular momentum the rotational axis moves in the direction of the maximum moment of inertia. After reorientation of the body, the centrifugal force is applied to the body at its new position, causing the equatorial bulge to readjust perpendicular to the new rotational axis (Fig. 1.10.A3). The equatorial bulge readjustment breaks the balance between the centrifugal and self-gravitational forces, and the Earth reorients again. The reorientation of the body and the readjustment of the equatorial bulge occur simultaneously until a new equilibrium is reached. For a negative mass anomaly (e.g., melt of the Laurentide ice sheet) the rotational axis moves towards the mass anomaly with respect to the Earth's surface. This change in rotational state translates into the sea level as well, where we see a relative sea level increase and decrease in opposing quadrants (Fig. 1.10.B, (Tamisiea, 2011; Peltier, 2004)). Following ice melt over the last deglaciation we see see a sea level increase around Australia and decrease around South America. The rotational feedback on the sea level in the northern hemisphere is not as noticeable due to the collapse of the northern hemisphere ice sheets (Laurentide and Fennoscandian) and all its consequences.

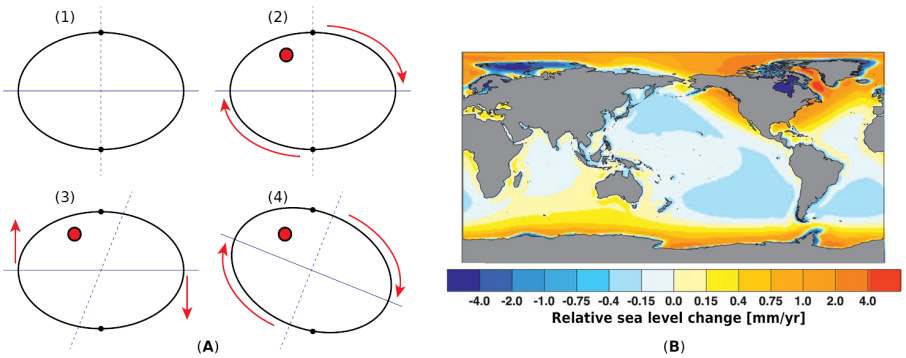

Figure 1.10: (A) Visual representation of true polar wander in the body-fixed co-rotating frame viewed in the body's cross-section, for a body with a dominant relaxation time much longer than its Chandler wobble period. The blue dashed line is the rotational axis, the blue solid line the position of the equatorial bulge, the black dots the original north and south poles, and the red with black encircled dot the positive mass anomaly. (Weerdesteijn, 2019) (B) Example model prediction of the ongoing GIA contributions to geodetic measurements, showing the relative sea level change (tide gauges), using the ICE-5G(VM2) ice history and rheological model (Peltier, 2004). (Tamisiea, 2011).

The last output of GIA modeling to discuss is the movement of ice and ocean masses, and the consequential earth deformation, which cause stresses in the Earth's crust (Wu et al., 2021, and references therein). Stress released due to deglaciation have been linked to possible glacially-triggered earthquakes in Greenland and earthquake-induced paleotsunamis in the North-Atlantic during the early Holocene (R. Steffen et al., 2020), and intraplate seismicity in northern Central Europe during the past millennium (Brandes et al., 2015).

An important feedback mechanism is the effect of solid Earth deformation and sea level change on ice sheet evolution (Fig. 1.7, left yellow box). For marine terminating glaciers, GIA can stabilize the grounding line (i.e., the location where the ice begins to float), which is dependent on the water depth (Whitehouse et al., 2019; Gomez et al., 2018; Kachuck et al., 2020; van Calcar et al., preprint). This feedback is particularly important for Antarctica which is characterized by ice flows with large floating sections, but some of Greenland's outlet glaciers also have substantial ice tongues and a reversed bed slope (i.e., the bed elevation decreases inward toward land) (Khan et al., 2014). The ice loss increases when the grounding line retreats into deeper water, leading to further retreat. However, relative sea level decreases due to the rebounding of the solid Earth following ice mass loss and the decrease in gravitational attraction on the ocean. This can lead to stabilization of the ice sheet or glacier. This stabilization mechanism is dependent on the rate of solid earth uplift and thus Earth's viscosity (see next section).

The outputs of the GIA model can be compared to historic sea level indicators (e.g., marine terraces, fossil beach deposits, dated corals) (Rovere et al., 2023) or modern geodetic measurements (Fig. 1.7, right yellow box). These measurements are for example vertical land motion from GNSS (Global Navigation Satellite System), mass changes from (satellite) gravimetry such as the GRACE and GRACE-FO missions, relative sea level from tide gauges, and absolute sea level from satellite altimetry. By comparing model outputs and observations, one can tune the model inputs (the ice loading and Earth rheology) to improve the model fit. The ice and Earth model should only be tuned within the constraints from other observations. For example, the ice sheet extent is constrained by geological evidence of glacial erratics, or the Earth rheology by viscosities derived from seismic wave anomalies (see next section).

Geodetic observations not only capture the response to ice mass changes over the last glacial cycle, but also to more recent ice mass changes, accelerated by human-induced climate change. It is commonly thought that GIA displacements result from a combination of (a) a viscous response to historic ice load changes (i.e., ice age melting), and (b) an elastic response to contemporary ice load changes. Thus, if one wants to infer GIA displacements related to the last glacial cycle, for example from GNSS, one has to correct the uplift for the contemporary ice mass changes with an elastic term. The remaining signal can then be used in combination with GIA modeling to further constrain ice sheet history or Earth rheology (Fig. 1.7). It is important that this elastic term is derived from measurements that are not too much affected by GIA. For example, estimates of the ice mass loss derived from satellite altimetry are to some extent affected by GIA as the distance between the satellite sensor and the Earth's surface changes due to changes in ice sheet thickness but also the solid Earth beneath this ice is rebounding. However, contemporary ice elevation changes are on the order of 1 m/yr whilst the solid earth uplift is on the order of 1 mm-cm/yr. The other way around, one can also correct the total signal with a GIA model to find the mass changes related to current climate change.

However, recent studies have shown regions undergoing rapid viscous uplift on decadal or centennial timescales in response to contemporary ice melt in West Antarctica (Barletta et al., 2018; Bradley et al., 2015; Nield et al., 2014; Samrat et al., 2020, 2021; Wolstencroft et al., 2015; Zhao et al., 2017) and southeast Greenland (Adhikari et al., 2021; Khan et al., 2016; Milne et al., 2018; Simpson et al., 2011; van Dam et al., 2017, Paper III). Thus, next to a viscous response to historic ice load changes and an elastic response to contemporary ice load changes, these modern geodetic measurements also capture a viscous response to contemporary ice load changes if the mantle viscosity underneath the ice loading is sufficiently low. Since this rapid viscous response is mixed with the other deformation components of GIA (elastic and long-term viscous) that are measured using GNSS, it is difficult to distinguish between solid earth deformation due to historical and contemporary ice load changes. This can

complicate (a) studies in which GNSS uplift rates are corrected for GIA from historic ice load changes and the remaining (assumed elastic) deformation is used to constrain contemporary ice discharge (e.g., Hansen et al., 2021) and (b) studies in which an elastic correction for contemporary ice change is applied to GNSS uplift rates to infer the GIA signal from past ice change (e.g., Whitehouse et al., 2012), because the viscous response from contemporary ice change is not considered.

1.3 Lateral variations in Earth's structure

Earlier GIA models assume a radially symmetric (i.e., lateral homogeneous or 1D) earth structure (e.g., Roy & Peltier, 2018), whilst more recent models explore the effect of lateral variations (e.g., van der Wal et al., 2015; Milne et al., 2018; Bagge et al., 2021; Marsman et al., 2021; Li et al., 2020; Yousefi et al., 2021; H. Steffen et al., 2006), as the Earth is characterized by lateral heterogeneities. Mantle viscosity can be inferred from seismic tomography as seismic waves sample elastic and transient rheology, allowing mapping of spatial variations (Figure 1.11 (Kennett et al., 1995; Shapiro & Ritzwoller, 2002)).

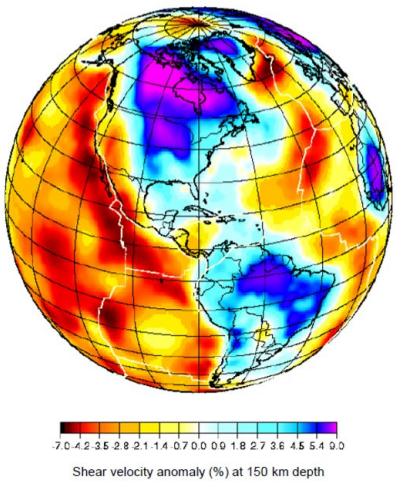

Figure 1.11: Isotropic S-wave velocities from the Median Model at 150 km depth in the upper mantle, presented as percent deviation from the 1D model ak135 (Kennett et al. 1995). (Shapiro & Ritzwoller, 2002).

Viscosity is dependent on the rock temperature, grain size, water content, melt fraction, and laboratory derived parameters (van der Wal et al., 2013; Hirth & Kohlstedt, 2003; Karato, 2008), whereas seismic wave velocities and attenuation are mostly affected by temperature, composition, grain size, and melt fraction.

To estimate viscosity from seismic wave velocity anomalies, there are two main approaches: the reference model approach (Ivins & Sammis, 1995; Wu et al., 2012) and the temperature-flow law approach (van der Wal et al., 2013, 2015). The first approach determines seismic velocity anomalies relative to a 1D model. Using diffusion creep laws, viscosity anomalies are determined from temperature anomalies, which are calculated from the velocity anomalies using temperature derivatives (Karato, 2008). The 3D viscosity structure is then found by adding the anomalies to a reference 1D viscosity structure. The temperature flow-law approach finds absolute temperatures from velocity with laboratory derived relationships. Diffusion creep viscosity is then based on temperature using olivine flow laws, and dislocation creep viscosity is based on the stress. The effective viscosity is determined from the diffusion and dislocation creep viscosities, and is controlled by the weaker viscosity of the two.

Both conversion methods have their weaknesses. Many flow law variables used in the temperature-flow law approach are poorly constrained. The reference model method only gives a Newtonian viscosity, but the upper mantle is likely characterized by more complex rheologies (Paxman et al., 2023; Lau et al., 2021; Blank et al., 2021; Adhikari et al., 2021). Ivins et al. (2021) described three different flow laws to derive lateral viscosity variations from a seismic model. These flow laws either assume diffusion creep, dislocation creep, or a combination of both (i.e., composite flow law). The choice of flow law can locally result in subsurface viscosities that vary by several orders of magnitude depending on the flow law. The reference model method assumes an independently constructed reference viscosity model that corresponds with the reference seismic and temperature models. Furthermore, velocities and attenuation are highly correlated and therefore variations in composition can be misinterpreted as temperature variations. Recent efforts further constrain the conversion from seismics to viscosity by adding constraints on water content derived from magnetotelluric electrical conductivity observations (Ramirez et al., 2022).

Large lateral variations in rheology are present in the lithosphere and upper mantle underneath Antarctica and Greenland, and they can have large effects on solid earth deformation. Especially important is the lateral extent of a low-viscosity region (Weerdesteijn et al., 2022, Paper II). Seismic studies in Antarctica show slower velocity anomalies in West compared to East Antarctica (Heeszel et al., 2016; Lloyd et al., 2020) (Fig. 1.12 (Lloyd et al., 2020; Kustowski et al., 2008; Fretwell et al., 2013; Bird, 2003)), consistent with a colder cratonic region in East Antarctica, and a warmer tectonically active region in West Antarctica, possibly with a mantle plume (Bredow et al., 2021). Lateral variations in mantle temperature, derived from seismic velocity anomalies, suggest lateral variations in mantle rheology (Ivins & Sammis, 1995; van der Wal et al., 2013). Upper mantle viscosities constrained by GNSS uplift and ice mass change show large variations across the Antarctic Peninsula and the Amundsen Sea Embayment, ranging from $<3{\cdot}10^{18}$ Pa s to $3{\cdot}10^{18}$ Pa s (Barletta et al., 2018; Bradley et al., 2015; Nield et al., 2014; Samrat et al., 2020, 2021; Wolstencroft et al., 2015; Zhao et al., 2017).

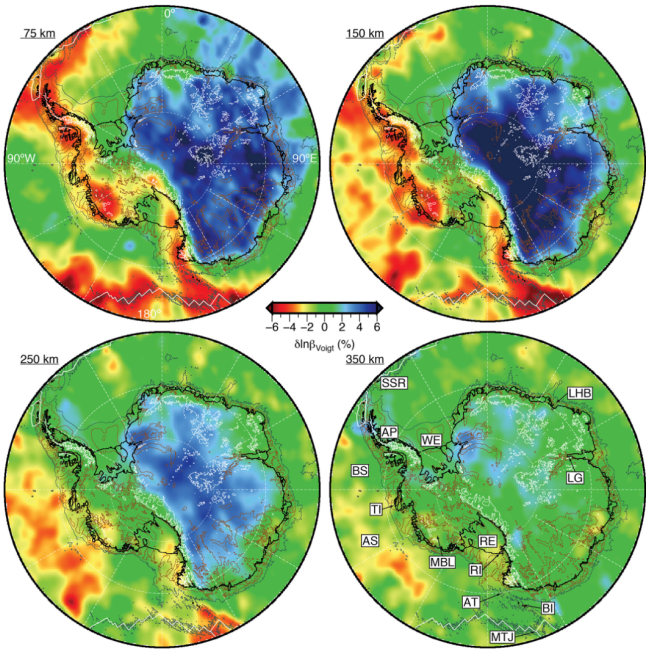

Figure 1.12: Tomographic images of the Voigt average shear-wave speed structure of ANT-20 at 75-, 150-, 250-, and 350-km depth with respect to sea level. Mantle velocity anomalies are relative to the 1-D Earth model STW105 (Kustowski et al., 2008), which has been slightly modified to account for the topography of first- and second- order seismic discontinuities. Bathymetry and bedrock topography contours are shown for 1,000 m (thin white line) and -500 m (thin brown line), as well as -2,500 m (thin dark gray line) elevation in the oceans (Fretwell et al., 2013). Thicker white lines denote the plate boundaries (Bird, 2003), while dashed white lines denote lines of latitude every 10° or lines of longitude every 30°. See Lloyd et al. (2020) for references to areas listed as abbreviations. (Lloyd et al., 2020).

Seismic analysis in Greenland also shows large lateral contrasts in shear wave velocity anomalies (Fig. 1.13A (Celli et al., 2021)). The Kangerlussuaq glacier in southeast Greenland, one of Greenland's three largest ice mass losing glaciers (Brough et al., 2019), sits above a proposed upper mantle low-viscosity feature that is likely as a consequence of Greenland having passed over the Iceland plume more than 40 Myr ago (Steinberger et al., 2019, 2004; O'Neill et al., 2005; Doubrovine et al., 2012). Proposed hot spot tracks align with magnetic, temperature, gravity, and seismic data (Celli et al., 2021; Martos et al., 2018; Mordret, 2018; Rogozhina et al., 2016; R. Steffen et al., 2018) (Fig. 1.13B (Martos et al., 2018; Forsyth et al., 1986)) and suggest a weakened lithosphere and upper mantle (Khan et al., 2016, Paper III).

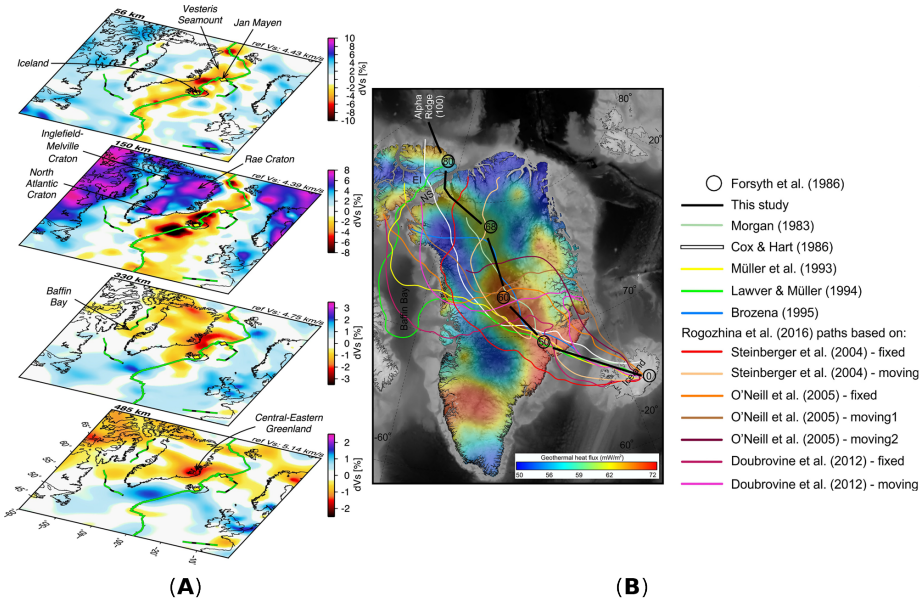

Figure 1.13: (A) Shear wave velocity anomalies depth slices through NAT2021 at 56, 150, 330 and 485 km depths in perspective view. Depth is shown on the top left of each panel, reference velocity on the top right. Mantle plumes are shown as yellow diamonds, past (dashed) and present (solid) plate boundaries are plotted in green. (Celli et al., 2021). (B) New heat flux distribution for Greenland and main Iceland plume tracks proposed since the 80s. Circles and numbers are plume track positions in millions of years based on Forsyth et al. (1986). Fixed: considering Iceland plume fixed. Moving: considering Iceland plume moving. EI = Ellesmere Island; NS = Nares Strait. (Martos et al., 2018).

Lateral variations in earth structure (e.g., in mantle viscosity and lithospheric thickness) greatly impact uplift rates following ice melt (Weerdesteijn et al., 2022, Paper II and III). Including these lateral variations in modeling efforts can increase our understanding of the Earth's response to ice melt and of the Earth's structure, especially near areas of low-viscosity upper mantle and areas characterized by historic and recent ice melt. Rapid uplift in response to recent deglaciation can potentially stabilize ice shelves and glaciers on the periphery of the Antarctic and Greenland ice sheets. This viscous contribution to uplift is usually not considered, but will become increasingly important in the future as deglaciation accelerates.

1.4 3D Glacial Isostatic Adjustment Modeling Codes

The majority of GIA models use a radially symmetric earth structure and are based on spherical-harmonic viscoelastic Love numbers (Farrell, 1972; Peltier, 1974). To include lateral variations in earth structure, numerical methods are required, such as the spectral-finite element method (Martinec, 2000; Klemann et al., 2008; Bagge et al., 2021; Hagedoorn et al., 2007; Tanaka et al., 2011), the finite element method (Zhong et al., 2022; Wu, 2004; Blank et al., 2021), and the finite volume method (Latychev et al., 2005; Gomez et al., 2018; Wan et al., 2022). These more advanced computational methods do come at a cost of a large increase in computational resources, and one needs to consider whether a 3D code is necessary because some regions or applications can be resolved with 1D codes (Hartmann et al., 2020).

There are differences between codes, for example regarding (in)compressibility, self-gravitation, spherical or box domain, shoreline migration, rotational feedback, resolving power etc. Over the past decade large benchmark studies have been undertaken (Spada et al., 2011; Martinec et al., 2018) (Fig. 1.14). However, in these studies the codes are benchmarked for 1D earth structures. Efforts are underway to benchmark the latest global models including 3D earth structures. Although not a global model (yet), we show the first initial comparison between 3D modeling codes with laterally varying viscosity in Paper I.

Throughout this thesis we use a new code in the GIA scene called ASPECT (Advanced Solver for Problems in Earth's ConvecTion). We use ASPECT v2.4.0 (Kronbichler et al., 2012; Heister et al., 2017; Bangerth et al., 2022a, 2022b; Rose et al., 2017; Clevenger & Heister, 2021) published under the GPL2 license and builds on the deal.II v9.4 finite element library (Arndt et al., 2022). ASPECT is open source and is originally build for Earth mantle convection studies. Because ASPECT is under continuous development its applications have extended beyond its original purpose to include, for example, subduction zone dynamics, dynamic topography, gravity field anomalies, and now also solid earth deformation following ice mass changes (e.g., Austermann et al., 2017; Dannberg & Gassmöller, 2018; Glerum et al., 2018; Clerc et al., 2021; Root et al., 2022; Weerdesteijn et al., 2023). ASPECT is supported by the Computational Infrastructure for Geodynamics (CIG) at the University of California in Davis through, e.g., user meetings and in-person hackathons to share developments, search help, and support code development by the main ASPECT developers and maintainers. ASPECT is written in C++, is build on advanced numerical methods (e.g., adaptive mesh refinement, linear and nonlinear solvers, stabilization of transport-dominated processes), and designed to support parallel computing.

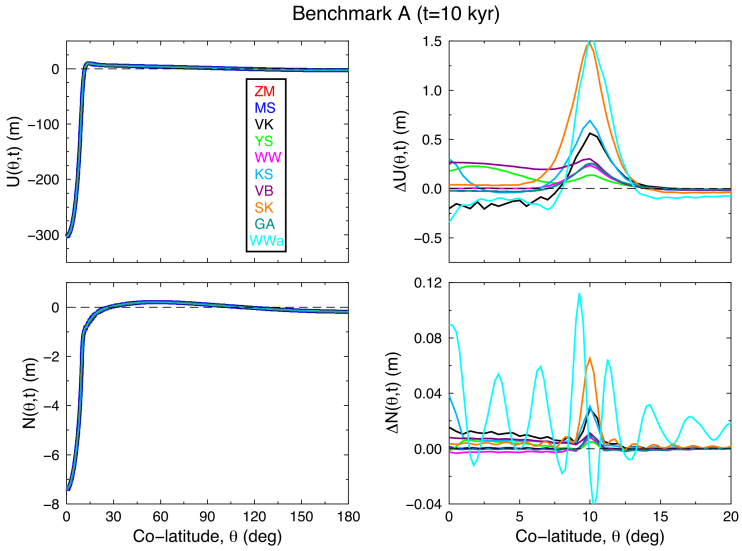

Figure 1.14: Left-hand panels: the latitudinal cross-section of surface vertical displacement U and geoid displacement N through the centre of the ice load located at (0°, 0°) and time $t = 10$ kyr for benchmark case A (solid earth deformation following a Heaviside loading centered at the pole, without an ocean basin) provided by the participants of the benchmark study. Right-hand panels: the differences between the individual solutions and VEGAref along the co-latitudinal interval (0°, 20°). See Martinec et al. (2018) for references to modeling codes listed as abbreviations. (Martinec et al., 2018).

Paper I presents a new solid earth deformation code for modeling glacial cycle to contemporary glacial mass changes, in combination with a dynamically changing finite element mesh. This new code is used in Paper II to explore the importance of contemporary ice melt above confined low-viscosity regions in the upper mantle, and how the low-viscosity region properties affect uplift rates. Paper III applies this code to southeast Greenland, where a weakened earth structure may be present as a result of the passage of Greenland over the Iceland plume. This new model can be used for regional modeling but not yet for global studies. It does not take into account gravity field changes induced by the deformation and does not solve for the gravitationally self-consistent redistribution of ocean water. Developments are underway to create a 3D spherical GIA model. Based on ASPECT, advancements have already been made on geoid calculations in combination with a free surface, boundary traction in a spherical domain, and a sea level post-processor which calculates the state of sea level as function of the geoid, topography, and solid earth deformation (see the next chapter for details on these developments). ASPECT is unique as it is open-source, used by a large community, and new developments are supported by the main developers and maintainers.

References

Adhikari, S., Milne, G. A., Caron, L., Khan, S. A., Kjeldsen, K. K., Nilsson, J., ... Ivins, E. R. (2021). Decadal to Centennial Timescale Mantle Viscosity Inferred From Modern Crustal Uplift Rates in Greenland. *Geophysical Research Letters*, *48*. doi: 10.1029/2021GL094040

Arndt, D., Bangerth, W., Feder, M., Fehling, M., Gassmöller, R., Heister, T., ... Wells, D. (2022). The `deal.II` library, version 9.4. *Journal of Numerical Mathematics*. Retrieved from https://dealii.org/deal94-preprint.pdf doi: 10.1515/jnma-2022-0054

Austermann, J., Mitrovica, J. X., Huybers, P., & Rovere, A. (2017). Detection of a dynamic topography signal in last interglacial sea-level records. *Science Advances*, *3*(7), e1700457. doi: 10.1126/sciadv.1700457

Bagge, M., Klemann, V., Steinberger, B., Latinović, M., & Thomas, M. (2021). Glacial-Isostatic Adjustment Models Using Geodynamically Constrained 3D Earth Structures. *Geochemistry, Geophysics, Geosystems*, *22*(11), e2021GC009853. doi: 10.1029/2021GC009853

Bangerth, W., Dannberg, J., Fraters, M., Gassmöller, R., Glerum, A., Heister, T., ... Naliboff, J. (2022a). *ASPECT v2.4.0.* Zenodo. doi: 10.5281/zenodo.6903424

Bangerth, W., Dannberg, J., Fraters, M., Gassmöller, R., Glerum, A., Heister, T., ... Naliboff, J. (2022b). *ASPECT: Advanced Solver for Problems in Earth's ConvecTion, User Manual.* doi: 10.6084/m9.figshare.4865333.v9

Barletta, V., Bevis, M., Smith, B., Wilson, T., Brown, A., Bordoni, A., ... Wiens, D. (2018). Observed rapid bedrock uplift in amundsen sea embayment promotes ice-sheet stability. *Science*, *360*, 1335–1339. doi: 10.1126/science.aao1447

Bird, P. (2003). An updated digital model of plate boundaries. *Geochemistry, Geophysics, Geosystems*, *4*(3). doi: 10.1029/2001GC000252

Blank, B., Barletta, V., Hu, H., Pappa, F., & van der Wal, W. (2021). Effect of Lateral and Stress-Dependent Viscosity Variations on GIA Induced Uplift Rates in the Amundsen Sea Embayment. *Geochemistry, Geophysics, Geosystems*, *22*(9), e2021GC009807. doi: 10.1029/2021GC009807

Bradley, S. L., Hindmarsh, R. C. A., Whitehouse, P. L., Bentley, M. J., & King, M. A. (2015). Low post-glacial rebound rates in the Weddell Sea due to Late Holocene ice-sheet readvance. *Earth and Planetary Science Letters*, *413*, 79-89. doi: 10.1016/j.epsl.2014.12.039

Brandes, C., Steffen, H., Steffen, R., & Wu, P. (2015). Intraplate seismicity in northern central europe is induced by the last glaciation. *Geology*, *43*(7), 611-614. doi: 10.1130/G36710.1

Bredow, E., Steinberger, B., Gassmoeller, R., & Dannberg, J. (2021). Mantle convection and possible mantle plumes beneath Antarctica – insights from geodynamic models and implications for topography. *Geological Society, London, Memoirs*, *56*. doi: https://doi.org/10.1144/M56-2020-2

Brough, S., Carr, J. R., Ross, N., & Lea, J. M. (2019). Exceptional Retreat of Kangerlussuaq Glacier, East Greenland, Between 2016 and 2018. *Frontiers*

in Earth Science, *7*(123). doi: 10.3389/feart.2019.00123

Celli, N. L., Lebedev, S., Schaeffer, A. J., & Gaina, C. (2021). The tilted iceland plume and its effect on the north atlantic evolution and magmatism. *Earth and Planetary Science Letters*, *569*, 117048. doi: 10.1016/j.epsl.2021.117048

Celsius, A. (1743). Anmärkning om vatnets färminskande så i Östersiön som Vesterhafvet. *Kongl. Swenska Wetenskaps Academiens Handlingar*, *4*, 33-50.

Clerc, F., Behn, M. D., & Minchew, B. M. (2021). Deglaciation-enhanced mantle CO2 fluxes at Yellowstone imply positive climate feedback. *Earth ArXiv*. doi: 10.31223/X56322

Clevenger, T. C., & Heister, T. (2021). Comparison between algebraic and matrix-free geometric multigrid for a Stokes problem on an adaptive mesh with variable viscosity. *Numerical Linear Algebra with Applications*, *28*(5), e2375. doi: 10.1002/nla.2375

Conrad, C. P. (2013). The solid earth's influence on sea level. *GSA Bulletin*, *125*(7-8), 1027-1052. doi: 10.1130/B30764.1

Conrad, C. P., & Hager, B. H. (1997). Spatial variations in the rate of sea level rise caused by the present-day melting of glaciers and ice sheets. *Geophysical Research Letters*, *24*, 1503-1506. doi: 10.1029/97GL0133

Coulson, S., Dangendorf, S., Mitrovica, J. X., Tamisiea, M. E., Pan, L., & Sandwell, D. T. (2022). A detection of the sea level fingerprint of greenland ice sheet melt. *Science*, *377*(6614), 1550-1554. doi: 10.1126/science.abo0926

Dannberg, J., & Gassmöller, R. (2018). Chemical trends in ocean islands explained by plume–slab interaction. *Proceedings of the National Academy of Sciences*, *115*(17), 4351-4356. doi: 10.1073/pnas.1714125115

de Geer, G. (1888). Om Skandinaviens nivåförändringar under qvartär-perioden. *Geologiska Föreningens i Stockholm Förhandlingar*, *10*, 366-379.

Doubrovine, P. V., Steinberger, B., & Torsvik, T. H. (2012). Absolute plate motions in a reference frame defined by moving hot spots in the pacific, atlantic, and indian oceans. *Journal of Geophysical Research: Solid Earth*, *117*(B9), B09101. doi: 10.1029/2011JB009072

Drinkwater, M., Floberghagen, R., Haagmans, R., Muzi, D., & Popescu, A. (2003). Goce: Esa's first earth explorer core mission. In G. Beutler, M. R. Drinkwater, R. Rummel, & R. Von Steiger (Eds.), *Earth gravity field from space - from sensors to earth sciences* (p. 419-432). Springer Netherlands, Dordrecht.

Ekman, M. (2009). *The changing level of the Baltic Sea during 300 years: A clue to understanding the Earth*. Summer Institute for Historical Geophysics.

Ekman, M. (2016). *The Man behind "Degrees Celsius": A Pioneer in Investigating the Earth and its Changes*. Summer Institute for Historical Geophysics.

Farrell, W. E. (1972). Deformation of the earth by surface loads. *Reviews of Geophysics*, *10*(3), 761-797. doi: 10.1029/RG010i003p00761

Farrell, W. E., & Clar, J. A. (1976). On postglacial sea level. *Geophysical Journal International*, *46*(3), 647-667. doi: 10.1111/j.1365-246X.1976.tb01252.x

Forsyth, D. A., Morel-A-L'Huissier, P., Asudeh, I., & Green, A. G. (1986). Alpha ridge and iceland-products of the same plume? *Journal of Geodynamics*, *6*(1-4), 197-214. doi: 10.1016/0264-3707(86)90039-6

Fretwell, P., Pritchard, H. D., Vaughan, D. G., Bamber, J. L., Barrand, N. E., Bell, R., ... Zirizzotti, A. (2013). Bedmap2: improved ice bed, surface and thickness datasets for antarctica. *The Cryosphere*, *7*(1), 375-393. doi: 10.5194/tc-7-375-2013

Glerum, A., Thieulot, C., Fraters, M., Blom, C., & Spakman, W. (2018). Nonlinear viscoplasticity in ASPECT: benchmarking and applications to subduction. *Solid Earth*, *9*(2), 267-294. doi: 10.5194/se-9-267-2018

Gomez, N., Latychev, K., & Pollard, D. (2018). A Coupled Ice Sheet–Sea Level Model Incorporating 3D Earth Structure: Variations in Antarctica during the Last Deglacial Retreat. *Journal of Climate*, *31*, 4041-4054. doi: 10.1175/JCLI-D-17-0352.1

Hagedoorn, J. M., Wolf, D., & Martinec, Z. (2007). An estimate of global mean sea-level rise inferred from tide-gauge measurements using glacial-isostatic models consistent with the relative sea-level record. *Pure and Applied Geophysics*, *164*, 791-818. doi: 10.1007/s00024-007-0186-7

Hansen, K., Truffer, M., Aschwanden, A., Mankoff, K., Bevis, M., Humbert, A., ... Khan, S. A. (2021). Estimating Ice Discharge at Greenland's Three Largest Outlet Glaciers Using Local Bedrock Uplift. *Geophysical Research Letters*, *48*. doi: 10.1029/2021GL094252

Hartmann, R., Ebbing, J., & Conrad, C. P. (2020). A Multiple 1D Earth Approach (M1DEA) to account for lateral viscosity variations in solutions of the sea level equation: An application for glacial isostatic adjustment by Antarctic deglaciation. *Journal of Geodynamics*, *135*, 101695. doi: 10.1016/j.jog.2020.101695

Heeszel, D. S., Wiens, D. A., Anandakrishnan, S., Aster, R. C., Dalziel, I. W. D., Huerta, A. D., ... Winberry, J. P. (2016). Upper mantle structure of central and West Antarctica from array analysis of Rayleigh wave phase velocities. *Journal of Geophysical Research: Solid Earth*, *121*, 1758-1775. doi: 10.1002/2015JB012616

Heister, T., Dannberg, J., Gassmöller, R., & Bangerth, W. (2017). High Accuracy Mantle Convection Simulation through Modern Numerical Methods – II: Realistic Models and Problems. *Geophysical Journal International*, *210*, 833-851. doi: 10.1093/gji/ggx195

Hirth, G., & Kohlstedt, D. (2003). Rheology of the upper mantle and the mantle wedge: A view from the experimentalists. In *Inside the subduction factory* (p. 83-105). American Geophysical Union (AGU).

Ivins, E. R., & Sammis, C. G. (1995). On lateral viscosity contrast in the mantle and the rheology of low-frequency geodynamics. *Geophysical Journal International*, *123*, 305-322. doi: 10.1111/j.1365-246X.1995.tb06856.x

Ivins, E. R., van der Wal, W., Wiens, D. A., Lloyd, A. J., & Caron, L. (2021). Antarctic upper mantle rheology. *Geological Society, London, Memoirs*,

56. doi: 10.1144/M56-2020-19

Kachuck, S. B., Martin, D. F., Bassis, J. N., & Price, S. F. (2020). Rapid Viscoelastic Deformation Slows Marine Ice Sheet Instability at Pine Island Glacier. *Geophysical Research Letters*, *47*, e2019GL086446. doi: 10.1029/2019GL086446

Karato, S.-I. (2008). *Deformation of Earth Materials*. Cambridge University Press, Cambridge, UK.

Kennett, B. L. N., Engdahl, E. R., & Buland, R. (1995). Constraints on seismic velocities in the earth from traveltimes. *Geophysical Journal International*, *122*(1), 108-124. doi: 10.1111/j.1365-246X.1995.tb03540.x

Khan, S. A., Kjeldsen, K. K., Kjær, K. H., Bevan, S., Luckman, A., Aschwanden, A., ... Fitzner, A. (2014). Glacier dynamics at helheim and kangerdlugssuaq glaciers, southeast greenland, since the little ice age. *The Cryosphere*, *8*(4), 1497-1507. doi: 10.5194/tc-8-1497-2014

Khan, S. A., Sasgen, I., Bevis, M., van Dam, T., Bamber, J. L., Wahr, J., ... Munneke, P. K. (2016). Geodetic measurements reveal similarities between post–Last Glacial Maximum and present-day mass loss from the Greenland ice sheet. *Science Advances*, *2*(9). doi: 10.1126/sciadv.1600931

Klemann, V., Martinec, Z., & Ivins, E. R. (2008). Glacial isostasy and plate motion. *Journal of Geodynamics*, *46*(3-5), 95-103. doi: 10.1016/j.jog.2008.04.005

Kronbichler, M., Heister, T., & Bangerth, W. (2012). High Accuracy Mantle Convection Simulation through Modern Numerical Methods. *Geophysical Journal International*, *191*, 12-29. doi: 10.1111/j.1365-246x.2012.05609.x

Kustowski, B., Ekström, G., & Dziewoński, A. M. (2008). Anisotropic shear-wave velocity structure of the earth's mantle: A global model. *Journal of Geophysical Research: Solid Earth*, *113*(B6). doi: 10.1029/2007JB005169

Lambeck, K., Purcell, A., Johnston, P., Nakada, M., & Yokoyama, Y. (2003). Water–load definition in the glacio–hydro–isostatic sea–level equation. *Quaternary Science Reviews*, *22*, 309–318. doi: 10.1016/S0277-3791(02)00142-7

Latychev, K., Mitrovica, J. X., Tromp, J., Tamisiea, M. E., Komatitsch, D., & Christara, C. C. (2005). Glacial isostatic adjustment on 3-D Earth models: a finite-volume formulation. *Geophysical Journal International*, *161*(2), 421-444. doi: 10.1111/j.1365-246X.2005.02536.x

Lau, H. C. P., Austermann, J., Holtzman, B. K., Havlin, C., Lloyd, A. J., Book, C., & Hopper, E. (2021). Frequency Dependent Mantle Viscoelasticity via the Complex Viscosity: Cases From Antarctica. *Journal of Geophysical Research: Solid Earth*, *126*(e2021JB022622). doi: 10.1029/2021JB022622

Li, T., Wu, P., Wang, H. S., Steffen, H., Khan, N. S., Engelhart, S. E., ... Horton, B. P. (2020). Uncertainties of Glacial Isostatic Adjustment model predictions in North America associated with 3D structure. *Geophysical Research Letters*, *47*, e2020GL087944. doi: 10.1029/2020GL087944

Lloyd, A. J., Wiens, D. A., Zhu, H., Tromp, J., Nyblade, A. A., Aster, R. C., ... O'Donnell, J. P. (2020). Seismic Structure of the Antarctic Upper Mantle

Imaged with Adjoint Tomography. *Journal of Geophysical Research: Solid Earth*, *125*. doi: 10.1029/2019JB017823

Marsman, C. P., van der Wal, W., Riva, R. E. M., & Freymueller, J. T. (2021). The Impact of a 3-D Earth Structure on Glacial Isostatic Adjustment in Southeast Alaska Following the Little Ice Age. *Journal of Geophysical Research: Solid Earth*, *126*, e2021JB022312. doi: 10.1029/2021JB022312

Martinec, Z. (2000). Spectral–finite element approach to three-dimensional viscoelastic relaxation in a spherical earth. *Geophysical Journal International*, *142*(1), 117-141. doi: 10.1046/j.1365-246x.2000.00138.x

Martinec, Z., & Hagedoorn, J. (2014). The rotational feedback on linear-momentum balance in glacial isostatic adjustment. *Geophysical Journal International*, *199*(3), 1823–1846. doi: 10.1093/gji/ggu369

Martinec, Z., Klemann, V., van der Wal, W., Riva, R. E. M., Spada, G., Sun, Y., ... James, T. S. (2018). A benchmark study of numerical implementations of the sea level equation in gia modelling. *Geophysical Journal International*, *215*(1), 389-414. doi: 10.1093/gji/ggy280

Martos, Y. M., Jordan, T. A., Catalán, M., Jordan, T. M., Bamber, J. L., & Vaughan, D. G. (2018). Geothermal Heat Flux Reveals the Iceland Hotspot Track Underneath Greenland. *Geophysical Research Letters*, *45*, 8214-8222. doi: 10.1029/2018GL078289

Maslin, M. (2016). Forty years of linking orbits to ice ages. *Nature*, *540*, 208-209. doi: 10.1038/540208a

Milne, G. A., Latychev, K., Schaeffer, A., Crowley, J. W., Lecavalier, B. S., & Audette, A. (2018). The influence of lateral Earth structure on glacial isostatic adjustment in Greenland. *Geophysical Journal International*, *214*, 1252–1266. doi: 10.1093/gji/ggy189

Mitrovica, J. X., & Milne, G. A. (2003). On post-glacial sea level: I. general theory. *Geophysical Journal International*, *154*(2), 253-267. doi: 10.1046/j.1365-246X.2003.01942.x

Mitrovica, J. X., Tamisiea, M. E., L., D. J., & A., M. G. (2001). Recent mass balance of polar ice sheets inferred from patterns of global sea-level change. *Nature*, *409*, 1026–1029. doi: 10.1038/35059054

Mitrovica, J. X., & Wahr, J. (2011). Ice age earth rotation. *Annual Review of Earth and Planetary Sciences*, *39*, 577-616. doi: 10.1146/annurev-earth-040610-133404

Mitrovica, J. X., Wahr, J., Matsuyama, I., & Paulson, A. (2005). The rotational stability of an ice-age earth. *Geophysical Journal International*, *161*(2), 491–506. doi: j.1365-246X.2005.02609.x

Mordret, A. (2018). Uncovering the Iceland Hot Spot Track Beneath Greenland. *Journal of Geophysical Research: Solid Earth*, *123*, 4922-4941. doi: 10.1029/2017JB015104

Nansen, F. (1921). *The strandflat and isostasy.* Skrifter utgit av Videnskapsselskapet i Kristiania, Matematisk-naturvidenskabelig klasse.

Nield, G. A., Barletta, V. R., A. Bordoni and, M. A. K., Whitehouse, P. L., Clarke, P. J., Domack, E., ... Berthier, E. (2014). Rapid bedrock uplift in the Antarctic Peninsula explained by viscoelastic response to recent

ice unloading. *Earth and Planetary Science Letters*, *397*, 32-41. doi: 10.1016/j.epsl.2014.04.019

O'Neill, C., Müller, D., & Steinberger, B. (2005). On the uncertainties in hot spot reconstructions and the significance of moving hot spot reference frames. *Geochemistry, Geophysics, Geosystems*, *6*(4), Q04003. doi: 10.1029/2004GC000784

Paxman, G. J. G., Lau, H. C. P., Austermann, J., Holtzman, B. K., & Havlin, C. (2023). Inference of the timescale-dependent apparent viscosity structure in the upper mantle beneath greenland. *AGU Advances*, *4*(2), e2022AV000751. doi: 10.1029/2022AV000751

Peltier, W. R. (1974). The impulse response of a maxwell earth. *Reviews of Geophysics*, *12*(4), 649-669. doi: 10.1029/RG012i004p00649

Peltier, W. R. (2004). Global glacial isostasy and the surface of the ice-age earth: the ice-5g (vm2) model and grace. *Annual Review of Earth and Planetary Sciences*, *32*, 111-149. doi: 10.1146/annurev.earth.32.082503.144359

Ramirez, F., Selway, K., Conrad, C. P., & Lithgow-Bertelloni, C. (2022). Constraining upper mantle viscosity using temperature and water content inferred from seismic and magnetotelluric data. *Journal of Geophysical Research: Solid Earth*, *127*, e2021JB023824. doi: 10.1029/2021JB023824

Reigber, C., Balmino, G., Schwintzer, P., Biancale, R., Bode, A., Lemoine, J., ... Perossanz, F. (2002). A high quality global gravity field model from champ gps tracking data and accelerometry (eigen-1s). *Geophysical Research Letters*, *29*(14). doi: 10.1029/2002GL015064

Rogozhina, I., Petrunin, A. G., Vaughan, A. P. M., Steinberger, B., Johnson, J. V., Kaban, M. K., ... Koulakov, I. (2016). Melting at the base of the Greenland ice sheet explained by Iceland hotspot history. *Nature Geoscience*, *9*, 366-369. doi: 10.1038/ngeo2689

Root, B. C., Sebera, J., Szwillus, W., Thieulot, C., Martinec, Z., & Fullea, J. (2022). Benchmark forward gravity schemes: the gravity field of a realistic lithosphere model WINTERC-G. *Solid Earth*, *13*(5), 849-873. doi: 10.5194/se-13-849-2022

Rose, I., Buffett, B., & Heister, T. (2017). Stability and accuracy of free surface time integration in viscous flows. *Physics of the Earth and Planetary Interiors*, *262*, 90-100. doi: 10.1016/j.pepi.2016.11.007

Rovere, A., Ryan, D. D., Vacchi, M., Dutton, A., Simms, A. R., & Murray-Wallace, C. V. (2023). The world atlas of last interglacial shorelines (version 1.0). *Earth System Science Data*, *15*(1), 1-23. doi: 10.5194/essd-15-1-2023

Roy, K., & Peltier, W. R. (2018). Relative sea level in the western mediterranean basin: A regional test of the ice-7g_na (vm7) model and a constraint on late holocene antarctic deglaciation. *Quaternary Science Reviews*, *183*, 76-87. doi: 10.1016/j.quascirev.2017.12.021

Samrat, N. H., King, M. A., Watson, C., Hay, A., Barletta, V. R., & Bordoni, A. (2021). Upper Mantle Viscosity Underneath Northern Marguerite Bay, Antarctic Peninsula Constrained by Bedrock Uplift and Ice Mass

Variability. *Geophysical Research Letters*, *48*(24), e2021GL097065. doi: 10.1029/2021GL097065

Samrat, N. H., King, M. A., Watson, C., Hooper, A., Chen, X., Barletta, V. R., & Bordoni, A. (2020). Reduced ice mass loss and three-dimensional viscoelastic deformation in northern Antarctic Peninsula inferred from GPS. *Geophysical Journal International*, *222*, 1013-1022. doi: 10.1093/gji/ggaa229

Shapiro, N. M., & Ritzwoller, M. H. (2002). Monte-carlo inversion for a global shear-velocity model of the crust and upper mantle. *Geophysical Journal International*, *151*(1), 88-105. doi: 10.1046/j.1365-246X.2002.01742.x

Simpson, M. J. R., Wake, L., Milne, G. A., & Huybrechts, P. (2011). The influence of decadal- to millennial-scale ice mass changes on present-day vertical land motion in Greenland: Implications for the interpretation of GPS observations. *Journal of Geophysical Research: Solid Earth*, *116*. doi: 10.1029/2010jb007776

Spada, G., Barletta, V. R., Klemann, V., Riva, R. E. M., Martinec, Z., P. Gasperini, B., ... King, M. A. (2011). A benchmark study for glacial isostatic adjustment codes. *Geophysical Journal International*, *185*(1), 106-132. doi: 10.1111/j.1365-246X.2011.04952.x

Steffen, H., Kaufmann, G., & Wu, P. (2006). Three-dimensional finite-element modeling of the glacial isostatic adjustment in Fennoscandia. *Earth and Planetary Science Letters*, *250*(1), 358-375. doi: 10.1016/j.epsl.2006.08.003

Steffen, R., Audet, P., & Lund, B. (2018). Weakened Lithosphere Beneath Greenland Inferred From Effective Elastic Thickness: A Hot Spot Effect? *Geophysical Research Letters*, *45*, 4733-4742. doi: 10.1029/2017GL076885

Steffen, R., Steffen, H., Weiss, R., Lecavalier, B. S., Milne, G. A., Woodroffe, S. A., & Bennike, O. (2020). Early holocene greenland-ice mass loss likely triggered earthquakes and tsunami. *Earth and Planetary Science Letters*, *546*, 116443. doi: 10.1016/j.epsl.2020.116443

Steinberger, B., Bredow, E., Lebedev, S., Schaeffer, A., & Torsvik, T. H. (2019). Widespread volcanism in the Greenland–North Atlantic region explained by the Iceland plume. *Nature Geoscience*, *12*, 61-68. doi: 10.1038/s41561-018-0251-0

Steinberger, B., Sutherland, R., & O'Connell, R. J. (2004). Prediction of emperor-hawaii seamount locations from a revised model of global plate motion and mantle flow. *Nature*, *430*, pages167–173. doi: 10.1038/nature02660

Tamisiea, M. E. (2011). Ongoing glacial isostatic contributions to observations of sea level change. *Geophysical Journal International*, *186*(3), 1036-1044. doi: 10.1111/j.1365-246X.2011.05116.x

Tamisiea, M. E., Mitrovica, J. X., Milne, G. A., & Davis, J. L. (2001). Global geoid and sea level changes due to present-day ice mass fluctuations. *Journal of Geophysical Research: Solid Earth*, *106*(B12), 30849-30863. doi: 10.1029/2000JB000011

Tanaka, Y., Klemann, V., Martinec, Z., & Riva, R. E. M. (2011). Spectral-finite element approach to viscoelastic relaxation in a spherical compressible

earth: application to gia modelling. *Geophysical Journal International*, *184*(1), 220-234. doi: 10.1111/j.1365-246X.2010.04854.x

Tapley, B. D., Bettadpur, S., Watkins, M., , & Reigber, C. (2004). The gravity recovery and climate experiment: mission overview and early results. *Geophysical Research Letters*, *31*(9), L09607. doi: 10.1029/2004GL019920

van Calcar, C. J., van de Wal, R. S. W., Blank, B., de Boer, B., & van der Wal, W. (preprint). Simulation of a fully coupled 3d gia – ice-sheet model for the antarctic ice sheet over a glacial cycle. doi: 10.5194/egusphere-2022-1328

van Dam, T., O. Francis, a. d. J., Khan, S. A., Bevis, M., & den Broeke, M. R. (2017). Using GPS and absolute gravity observations to separate the effects of present-day and Pleistocene ice-mass changes in South East Greenland. *Earth and Planetary Science Letters*, *459*, 127-135. doi: 10.1016/j.epsl.2016.11.014

van der Wal, W., Barnhoorn, A., Stocchi, P., Gradmann, S., Wu, P., Drury, M., & Vermeersen, B. (2013). Glacial isostatic adjustment model with composite 3-D Earth rheology for Fennoscandia. *Geophysical Journal International*, *194*(1), 61-77. doi: 10.1093/gji/ggt099

van der Wal, W., Whitehouse, P. L., & Schrama, E. J. O. (2015). Effect of GIA models with 3D composite mantle viscosity on GRACE mass balance estimates for Antarctica. *Earth and Planetary Science Letters*, *414*, 134-143. doi: 10.1016/j.epsl.2015.01.001

Wan, J. X. W., Gomez, N., Latychev, K., & Han, H. K. (2022). Resolving glacial isostatic adjustment (GIA) in response to modern and future ice loss at marine grounding lines in West Antarctica. *The Cryosphere*, *16*(6), 2203–2223. doi: 10.5194/tc-16-2203-2022

Weerdesteijn, M. F. M. (2019). *The implementation of glaciation-induced rotational behavior of the earth in a numerical model* (Master thesis, Delft University of Technology). http://resolver.tudelft.nl/uuid:c2ca74b4-f909-45f0-9d11-0d4994695da2.

Weerdesteijn, M. F. M., Conrad, C. P., & Naliboff, J. B. (2022). Solid Earth Uplift Due To Contemporary Ice Melt Above Low-Viscosity Regions of the Upper Mantle. *Geophysical Research Letters*, *49*(17), e2022GL099731. doi: 10.1029/2022GL099731

Weerdesteijn, M. F. M., Naliboff, J. B., Conrad, C. P., Reusen, J. M., Steffen, R., Heister, T., & Zhang, J. (2023). Modeling viscoelastic solid earth deformation due to ice age and contemporary glacial mass changes in aspect. *Geochemistry, Geophysics, Geosystems*, *24*(3), e2022GC010813. doi: 10.1029/2022GC010813

Whitehouse, P. L. (2018). Glacial isostatic adjustment modelling: historical perspectives, recent advances and future directions. *Earth Surface Dynamics*, *6*, 401-429. doi: 10.5194/esurf-6-401-2018

Whitehouse, P. L., Bentley, M. J., Milne, G. A., King, M. A., & Thomas, I. D. (2012). A new glacial isostatic adjustment model for antarctica: calibrated and tested using observations of relative sea-level change and present-day uplift rates. *Geophysical Journal International*, *190*(3), 1464-1482. doi:

10.1111/j.1365-246X.2012.05557.x

Whitehouse, P. L., Gomez, N., King, M. A., & Wiens, D. A. (2019). Solid Earth change and the evolution of the Antarctic Ice Sheet. *Nature Communications*, *10*(503). doi: 10.1038/s41467-018-08068-y

Wolstencroft, M., King, M. A., Whitehouse, P. L., Bentley, M. J., Nield, G. A., King, E. C., ... Gunter, B. C. (2015). Uplift rates from a new high-density GPS network in Palmer Land indicate significant late Holocene ice loss in the southwestern Weddell Sea. *Geophysical Journal International*, *203*, 737-754. doi: 10.1093/gji/ggv327

Wu, P. (2004). Using commercial finite element packages for the study of earth deformations, sea levels and the state of stress. *Geophysical Journal International*, *158*, 401-408. doi: 10.1111/j.1365-246X.2004.02338.x

Wu, P., Steffen, R., Steffen, H., & Lund, B. (2021). lacial isostatic adjustment models for earthquake triggering. In H. Steffen, O. Olesen, & R. Sutinen (Eds.), *Glacially-triggered faulting* (p. 383-401). Cambridge University Press.

Wu, P., Wang, H., & Steffen, H. (2012). The role of thermal effect on mantle seismic anomalies under laurentia and fennoscandia from observations of glacial isostatic adjustment. *Geophysical Journal International*, *192*(1), 7-17. doi: 10.1093/gji/ggs009

Yousefi, M., Milne, G. A., & Latychev, K. (2021). Glacial isostatic adjustment of the Pacific Coast of North America: the influence of lateral Earth structure. *Geophysical Journal International*, *226*, 91-113. doi: 10.1093/gji/ggab053

Zhao, C., A.King, M., Watson, C. S., Barletta, V. R., Bordoni, A., Dell, M., & Whitehouse, P. L. (2017). Rapid ice unloading in the Fleming Glacier region, southern Antarctic Peninsula and its effect on bedrock uplift rates. *Earth and Planetary Science Letters*, *473*, 164-176. doi: 10.1016/j.epsl.2017.06.002

Zhong, S., Kang, K., A, G., & Qin, C. (2022). CitcomSVE: A Three-dimensional Finite Element Software Package for Modeling Planetary Mantle's Viscoelastic Deformation in Response to Surface and Tidal Loads. *Geochemistry, Geophysics, Geosystems*, *23*, e2022GC010359. doi: 10.1029/2022GC010359

Chapter 2

Conclusions and outlook

Generally, it is assumed that GIA displacements consist of an elastic response to contemporary ice melt (Fig. 2.1A) and a viscous response to historic deglaciation (Fig. 2.1B). Low viscosities in the upper mantle can result in a viscous response to recent ice melt that is important on short (decadal) timescales (Fig. 2.1C). This viscous contribution to uplift is often not considered, but will become increasingly important in the future as deglaciation accelerates. Paper I presents a new solid earth deformation code for modeling glacial cycle to contemporary glacial mass changes with lateral variations in earth structure. This new code is used in Paper II to explore the importance of contemporary ice melt above confined low-viscosity regions in the upper mantle, and how the low-viscosity region properties affect uplift rates. With this newly gained knowledge, Paper III applies this code to southeast Greenland, where a weakened earth structure may be present as a result of Greenland passing over the Iceland plume (Fig. 2.1, bottom row).

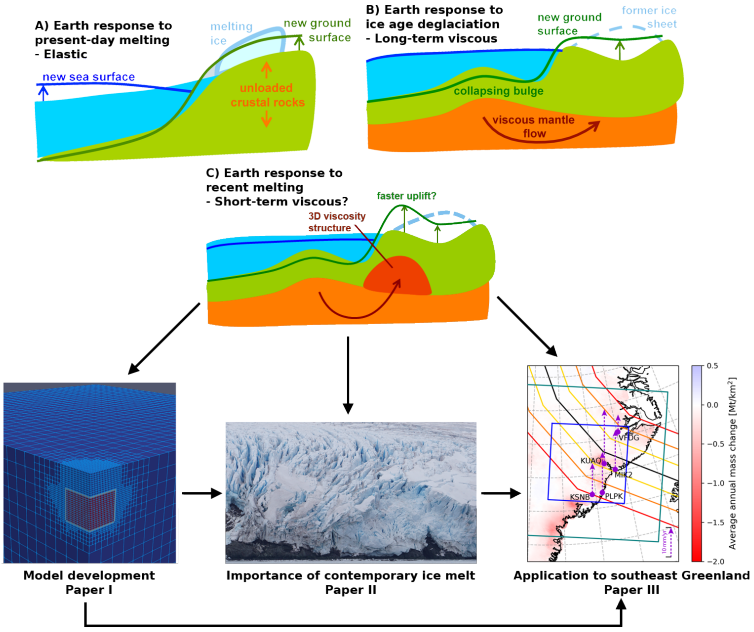

Figure 2.1: Motivation and overview of the research presented in this thesis. Figures A, B, and C courtesy of Clinton P. Conrad. Paper I and III figures courtesy of Maaike F. M. Weerdesteijn. Paper II photo by Maaike F. M. Weerdesteijn.

This chapter summarizes the main results from this thesis in Section 2.1, and discusses the limitations of the work as well as the author's vision on future directions in Section 2.2.

2.1 Summary of main results

Paper I key points:

- The solid Earth is deforming in response to past and present ice loading changes at rates determined by elastic and viscous parameters.
- We benchmark a new viscoelastic solid Earth deformation model in the open-source code ASPECT in combination with adaptive mesh refinement.
- This code can be used to study regional Earth deformation rates from ice age and contemporary ice melt on a laterally heterogeneous Earth.

Paper I covers the benchmark of a new solid earth deformation model in ASPECT: an open-source finite element code to simulate problems in thermal convection in the Earth's mantle, with large lateral variations in viscosity. We compare solid earth deformation using ASPECT to solutions using TABOO, a semi-analytical code based on the normal mode method, and Abaqus, a commercial finite element code, for a layered earth model. A big advantage of ASPECT over other codes is that it uses modern numerical methods, such as adaptive mesh refinement and is built for parallel computing, also in combination with dynamically changing meshes. ASPECT can be extended by users and is under continuous development. The maximum deformation and deformation rates using ASPECT agree within 2.6% for the average percentage difference with TABOO and Abaqus on glacial cycle ($\sim$100 kyr) and contemporary ice melt ($\sim$100 years) timescales. This gives confidence in the performance of our new solid earth deformation model.

We demonstrate the computational efficiency of using adaptively refined meshes and we report on parallel scalability of the code. Surface loads change at different rates and at different locations within the model domain. With the adaptive mesh refinement capability and differently changing ice loads across the domain, we can model earth deformation and speed up the computation considerably, saving computational resources by not requiring a highly refined mesh over regions where no large surface ice load changes occur. Furthermore, we demonstrate the model performance in the presence of lateral viscosity variations in the upper mantle, which represents a first of its kind benchmark for numerical GIA codes.

Paper II key points:

- Contemporary ice melt above low-viscosity mantle produces uplift on decadal timescales, but viscosity heterogeneity affects uplift rates.
- Our viscoelastic deformation models with varying viscosity show that a low-viscosity region's horizontal extent greatly affects uplift rates.
- The viscous response to recent ice melting, often not considered, may be a dominant contributor to uplift above low-viscosity regions.

Paper II investigates the role of small (∼100s km) regions of unusually low-viscosity mantle underneath areas of contemporary ice melt. We developed viscoelastic models with low-viscosity regions in the upper mantle, and measured the effect of these regions on solid earth uplift resulting from contemporary surface ice melt. Our viscoelastic deformation models show that contemporary ice melt generates not only an elastic response of the solid earth but also a viscous response. Although this may seem trivial and has been suggested before (e.g., Whitehouse, 2018; Simpson et al., 2011), it has not been quantified, especially not using an earth model with lateral variations. If the melting occurs near a low-viscosity region of the upper mantle, then this viscous response can be larger than the elastic response. With such a large viscous contribution, uplift in areas of large ice melt can be controlled by recent or contemporary ice melt instead of by historic ice melt from the last deglaciation.

From a sensitivity analysis of the location, dimensions, and viscosity of a low-viscosity region, we find that the largest uncertainty in uplift rates from contemporary ice melt comes from the horizontal extent of the low-viscosity region. We find that uplift from contemporary ice melt can be as much as 10 times larger for a very wide (essentially infinite) low-viscosity region than it is without a low-viscosity region, and a confined low-viscosity region produces intermediate rates. Our modeled uplift rates show that there is a significant reduction in rates for low-viscosity regions with a radius smaller than 300 km compared to an LV asthenospheric layer. Thus, 3D modeling is important near areas of reduced viscosity in the upper mantle. As the low-viscosity region amplifies GIA uplift from contemporary ice melt, it is important to constrain the location, dimensions, and viscosity of an low-viscosity region in order to distinguish between uplift generated by past and contemporary ice melt. Rapid viscous ground uplift can impact ice dynamics if the low-viscosity region is located close to an ice sheet margin, as for Antarctica and Greenland.

Paper III key points:

- On the coast of southeast Greenland, near the Kangerlussuaq glacier, GNSS stations show abnormally rapid ground uplift.
- We explain this uplift as being driven by recent ice melt sitting above weakened earth structure, consistent with Greenland passing over the Iceland plume.
- This viscous contribution is not often considered in GIA models, but will become increasingly important in the future as deglaciation accelerates.

Paper III follows up on the importance of contemporary ice melt above low-viscosity upper mantle that we found in Paper II, and applies the code presented in Paper I to investigate uplift rates in southeast Greenland. Along most of the periphery of the Greenland ice sheet, Global Navigation Satellite System (GNSS) stations observe slow uplift of the ground surface (few mm/yr), reflecting Earth's response to past and contemporary changes in Greenland's ice mass. On the coast of southeast Greenland, near the Kangerlussuaq glacier, GNSS stations show abnormally rapid ground uplift that cannot be explained by current GIA models, even with transient viscosity. One explanation for this rapid uplift may arise from Greenland's unusual tectonic history: Greenland passed over the Iceland mantle plume over 40 million years ago, and it is likely that the tracks of this plume-lithosphere interaction are preserved beneath southeast Greenland. Magnetic, heat flow, gravity, and seismic data point towards a potentially weakened lithosphere and upper mantle beneath southeast Greenland. Recent studies suggest that a weakened earth structure can dramatically accelerate the GIA response to deglaciation (showing viscous deformation to contemporary ice load changes), leading to rapid uplift beneath regions of active present-day mass loss. Indeed, a low-viscosity region associated with the Iceland plume has been shown to produce rapid uplift in layered models, but this has not been tested in a 3D setting, nor with all of the relevant ice mass changes occurring over last glacial cycle, the second millennium, and the past few decades, which have all been shown to significantly affect uplift patterns.

We show that a viscous response to ice loading changes over the second millennium and the satellite altimetry era may actually control uplift rates in parts of Greenland. The magnitude of these viscous components increases greatly in the presence of a low-viscosity plume track. This contribution is not often considered in glacial isostatic adjustment models, but will become increasingly important in the future as deglaciation accelerates. Our models suggest large uplift rates ($\sim$60 mm/yr) for a low-viscosity upper mantle during periods of fast ice mass loss over the last deglaciation (around 9 ka bp), which could also have helped to stabilize nearby glaciers over the last glacial cycle. These findings have implications for the interpretation of GNSS uplift rates near areas of past and current (de)glaciation. More complex modeling, as shown here, is needed near areas of significant recent deglaciation above low-viscosity mantle. Such modeling is important to accurately infer earth structure and ice loading history from uplift observations.

2.2 Limitations and future directions

This section discusses the limitations of the papers presented in this thesis, and presents ideas about how to overcome these limitations in future studies. The limitations are regarding: ice loading history models, linear versus complex earth rheology, regional versus global GIA modeling, and computational resources.

In Paper II we apply ice melt of 1 m/yr which is the order of magnitude for contemporary ice melt in Antarctica and Greenland (Helm et al., 2014; The IMBIE Team, 2018). In Paper III we try to match observations of uplift in southeast Greenland by including ice loading changes over the last glacial cycle, second millennium, and the satellite altimetry era. Although we are able to match observations of uplift at two of the GNSS sites near the Kangerlussuaq glacier and one in the north, two other stations located south of the glacier seem to be insensitive to the choice of plume track, and we predict slower uplift rates than observed. Even when the plume track extends to these sites, the uplift rates are barely affected. South of these stations lies the Helheim glacier, which next to the Kangerlussuaq glacier presents one of Greenland's largest ice mass losing glaciers (Khan et al., 2020). Mass loss at the Helheim glacier could affect uplift rates at these two sites.

The discrepancy between modeled and observed uplift rates at these sites suggests that either (i) the ice loading input data in the southern part of the ice loading area may not capture the full extent of the ice mass loss on the periphery of the ice sheet, or (ii) the weakened earth structure from the plume track extends further south toward the Helheim glacier's mass loss. (i) We use one volume-derived mass balance derived from satellite altimetry (Simonsen et al., 2021), and the second millennium ice loading pattern is scaled to this loading. Because uplift rates are dominated by these recent ice loading changes, alternative mass balance data sets should be considered (The IMBIE Team, 2020; Khan et al., 2022). For example, the altimetry derived mass balance from Khan et al. (2022) generally predicts larger annual mass change rates than the model used here. The mass anomaly over the second millennium shows large uncertainty (Adhikari et al., 2021) and for future studies one can take into account the upper and lower mass anomaly boundaries. Furthermore, for the last glacial cycle we use the global ICE-6G_C ice history model (Argus et al., 2014; Peltier et al., 2015). A more focused Greenland ice history model (Lecavalier et al., 2014) may provide better constraints as opposed to a global model. (ii) The lateral extent of the possible plume track or otherwise weakened earth structure is not well constrained (Rogozhina et al., 2016; Martos et al., 2018; Mordret, 2018; Steffen et al., 2018; Celli et al., 2021; Steinberger et al., 2004; O'Neill et al., 2005; Doubrovine et al., 2012; Steinberger et al., 2019), and potentially extends further south based on recent constraints from seismic tomography (Celli et al., 2021) and geothermal heat flux (Kolster et al., 2023). A lower viscosity in this region would reduce the resistance to material flow in the upper mantle flow and could lead to larger uplift rates at the southern GNSS sites following ice melt of the Helheim glacier.

In Paper I we benchmark solid earth deformation with a linear viscoelastic rheology, which we then apply in Papers II and III. We do not explore more complex rheologies such as composite flow laws (e.g., Ivins et al., 2021) or time- and stress-dependent viscosity (i.e., transient rheology), which may play an important role (Paxman et al., 2023; Lau et al., 2021; Kang et al., 2022; Blank et al., 2021; Adhikari et al., 2021). Such rheological complexity may also contribute to, or even generate, confined regions with effectively low viscosity, of the sort that we have modeled in Paper II. Regarding southeast Greenland (Paper III), a recent study on transient viscosity in Greenland predicts average apparent viscosities on the order of 10^{19} Pa s for centennial timescales, and increasing viscosities for longer timescales (Paxman et al., 2023). However, their low apparent viscosity is not as low as predicted in Paper III or by Khan et al. (2016) to match observed uplift rates near the Kangerlussuaq glacier, and is not as spatially confined. We show that we can match the rapid observed uplift rates near the Kangerlussuaq glacier without employing a transient rheology. Instead, excess rapid uplift can be driven by contemporary ice melt if it occurs above diminished linear viscosity and thin lithosphere, both weakened by interaction with the Iceland plume. We do not reject the idea of the presence of a more complex rheology, but show the potential non-uniqueness of the solution if uplift rates can be matched either by complex rheologies or laterally varying linear viscosities, as we have shown here. Viscoelastic-plastic rheologies are recently implemented in ASPECT, with additional options for selecting dislocation creep, diffusion creep or composite viscous flow laws. In order to use complex rheologies in combination with a free surface (i.e., mesh deformation) and boundary traction (i.e., surface loading), the next step would be to perform a new benchmark study for layered earth structures with analytical models. The impact of rheological complexity needs more investigation and could help to reconcile models and observations of uplift.

In Paper I we present a tool for modeling solid earth deformation on regional scales. This is only one component of several processes that work together to produce GIA (see Introduction). Our new model can be used for regional modeling but not for global studies, as it does not take into account gravity field changes induced by the deformation and does not solve for the gravitationally self-consistent redistribution of ocean water. Progress has been made on implementing GIA on a global scale, including solving the sea level equation, in ASPECT, but this work is unfortunately not finished by the time of submitting this thesis. Gravitational perturbations for a 3D spherical model are calculated using the "geoid.cc" postprocessor. Previously the gravitational perturbations were based on dynamic topography (i.e., instant surface deflection based on stresses at the surface). Now, we implemented a feature that computes gravitational perturbations based on the free surface (i.e., deforming mesh), which is essential for GIA modeling as the surface viscously deforms over time according to the free surface, and not instantaneously as for the dynamic topography. The geoid postprocessor is merged with the main code and can be found in the main branch of ASPECT on

GitHub (https://github.com/geodynamics/aspect). Furthermore, the new state of sea level as function of the geoid, topography (with an initial ocean basin), and solid earth deformation, can be calculated using the "sealevel.cc" postprocessor. Unfortunately, this postprocessor has not been tested yet due to large strain rate anomalies at the corners of more refined mesh regions in the spherical geometry, affecting the free surface deformations. This numerical problem needs to be solved first. The sea level postprocessor does not include rotational feedback. As the postprocessor is not benchmarked (yet), it is not on the main branch of the ASPECT code, but on the thesis author's personal GitHub page under the "gia_topo_to_sealevel_efficient" branch (https://github.com/mfmweerdesteijn/aspect/blob/gia_topo_to_sealevel_efficient/source/postprocess/sea_level.cc). These future developments will allow ASPECT to join a small suite of numerical 3D spherical GIA models.

The stabilization mechanism of the solid earth uplift on glaciers and ice sheet (Whitehouse et al., 2019; Gomez et al., 2018; Kachuck et al., 2020), as discussed in the Introduction, depends on the rate of uplift and thus Earth's viscosity. After a full 3D GIA model is implemented and benchmarked in ASPECT, the next step would be to couple the GIA model to an ice sheet evolution model, as e.g., van Calcar et al. (preprint) shows (but in commercial software) and (Gomez et al., 2018). Such a tool is useful to study the solid Earth - ice interactions and stabilization mechanisms both over the last deglaciation (where we model uplift rates of over 60 mm/yr between 10 and 4 ka bp) and on contemporary timescales for predicting future sea level change. This would also require better constraints on the viscosity structure from, for example, an inversion using a variety of geophysical observations (Ramirez et al., 2022).

Lastly, regarding code application, we can only test a finite number of earth and ice models. For this PhD thesis research sufficient computational resources were available through Sigma2. However, because not all researchers have access to large amounts of computational resources and because computations that require high-performance computing have a negative environmental impact, it is important to consider when a lower resolution or less powerful tool (e.g., 1D GIA model) provides sufficiently accurate results.

References

Adhikari, S., Milne, G. A., Caron, L., Khan, S. A., Kjeldsen, K. K., Nilsson, J., ... Ivins, E. R. (2021). Decadal to Centennial Timescale Mantle Viscosity Inferred From Modern Crustal Uplift Rates in Greenland. *Geophysical Research Letters*, *48*. doi: 10.1029/2021GL094040

Argus, D. F., Peltier, W. R., Drummond, R., & Moore, A. W. (2014). The Antarctica component of postglacial rebound model ICE-6G_C (VM5a) based upon GPS positioning, exposure age dating of ice thicknesses, and

relative sea level histories. *Geophysical Journal International*, *198*(1), 537-563. doi: 10.1093/gji/ggu140

Blank, B., Barletta, V., Hu, H., Pappa, F., & van der Wal, W. (2021). Effect of Lateral and Stress-Dependent Viscosity Variations on GIA Induced Uplift Rates in the Amundsen Sea Embayment. *Geochemistry, Geophysics, Geosystems*, *22*(9), e2021GC009807. doi: 10.1029/2021GC009807

Celli, N. L., Lebedev, S., Schaeffer, A. J., & Gaina, C. (2021). The tilted iceland plume and its effect on the north atlantic evolution and magmatism. *Earth and Planetary Science Letters*, *569*, 117048. doi: 10.1016/j.epsl.2021.117048

Doubrovine, P. V., Steinberger, B., & Torsvik, T. H. (2012). Absolute plate motions in a reference frame defined by moving hot spots in the pacific, atlantic, and indian oceans. *Journal of Geophysical Research: Solid Earth*, *117*(B9), B09101. doi: 10.1029/2011JB009072

Gomez, N., Latychev, K., & Pollard, D. (2018). A Coupled Ice Sheet–Sea Level Model Incorporating 3D Earth Structure: Variations in Antarctica during the Last Deglacial Retreat. *Journal of Climate*, *31*, 4041-4054. doi: 10.1175/JCLI-D-17-0352.1

Helm, V., Humbert, A., & Miller, H. (2014). Elevation and elevation change of Greenland and Antarctica derived from CryoSat-2. *The Cryosphere*, *8*, 1539-1559. doi: 10.5194/tc-8-1539-2014

Ivins, E. R., van der Wal, W., Wiens, D. A., Lloyd, A. J., & Caron, L. (2021). Antarctic upper mantle rheology. *Geological Society, London, Memoirs*, *56*. doi: 10.1144/M56-2020-19

Kachuck, S. B., Martin, D. F., Bassis, J. N., & Price, S. F. (2020). Rapid Viscoelastic Deformation Slows Marine Ice Sheet Instability at Pine Island Glacier. *Geophysical Research Letters*, *47*, e2019GL086446. doi: 10.1029/2019GL086446

Kang, K., Zhong, S., A, G., & Mao, W. (2022). The effects of non-Newtonian rheology in the upper mantle on relative sea level change and geodetic observables induced by glacial isostatic adjustment process. *Geophysical Journal International*, *228*, 1975-1991. doi: 10.1093/gji/ggab428

Khan, S. A., Bamber, J. L., Rignot, E., Helm, V., Aschwanden, A., Holland, D. M., ... Kuipers Munneke, P. (2022). Greenland Mass Trends From Airborne and Satellite Altimetry During 2011–2020. *Journal of Geophysical Research: Solid Earth*, *127*, e2021JF006505. doi: 10.1029/2021JF006505

Khan, S. A., Bjørk, A. A., Bamber, J. L., Morlighem, M., Bevis, M., Kjær, K. H., ... Schenk, T. (2020). Centennial response of Greenland's three largest outlet glaciers. *Nature Communications*, *11*. doi: 10.1038/s41467-020-19580-5

Khan, S. A., Sasgen, I., Bevis, M., van Dam, T., Bamber, J. L., Wahr, J., ... Munneke, P. K. (2016). Geodetic measurements reveal similarities between post–Last Glacial Maximum and present-day mass loss from the Greenland ice sheet. *Science Advances*, *2*(9). doi: 10.1126/sciadv.1600931

Kolster, M. E., Døssing, A., & Khan, S. A. (2023). Satellite Magnetics Suggest a Complex Geothermal Heat Flux Pattern beneath the Greenland Ice Sheet.

Remote Sensing, *15*(5), 1379. doi: 10.3390/rs15051379

Lau, H. C. P., Austermann, J., Holtzman, B. K., Havlin, C., Lloyd, A. J., Book, C., & Hopper, E. (2021). Frequency Dependent Mantle Viscoelasticity via the Complex Viscosity: Cases From Antarctica. *Journal of Geophysical Research: Solid Earth*, *126*(e2021JB022622). doi: 10.1029/2021JB022622

Lecavalier, B. S., Milne, G. A., Simpson, M. J. R., Wake, L., Huybrechts, P., Tarasov, L., ... Larsen, N. K. (2014). A model of Greenland ice sheet deglaciation constrained by observations of relative sea level and ice extent. *Quaternary Science Reviews*, *102*, 54-84. doi: 10.1016/j.quascirev.2014.07.018

Martos, Y. M., Jordan, T. A., Catalán, M., Jordan, T. M., Bamber, J. L., & Vaughan, D. G. (2018). Geothermal Heat Flux Reveals the Iceland Hotspot Track Underneath Greenland. *Geophysical Research Letters*, *45*, 8214-8222. doi: 10.1029/2018GL078289

Mordret, A. (2018). Uncovering the Iceland Hot Spot Track Beneath Greenland. *Journal of Geophysical Research: Solid Earth*, *123*, 4922-4941. doi: 10.1029/2017JB015104

O'Neill, C., Müller, D., & Steinberger, B. (2005). On the uncertainties in hot spot reconstructions and the significance of moving hot spot reference frames. *Geochemistry, Geophysics, Geosystems*, *6*(4), Q04003. doi: 10.1029/2004GC000784

Paxman, G. J. G., Lau, H. C. P., Austermann, J., Holtzman, B. K., & Havlin, C. (2023). Inference of the timescale-dependent apparent viscosity structure in the upper mantle beneath greenland. *AGU Advances*, *4*(2), e2022AV000751. doi: 10.1029/2022AV000751

Peltier, W. R., Argus, D. F., & Drummond, R. (2015). Space geodesy constrains ice-age terminal deglaciation: The global ICE-6G_C (VM5a) model. *Journal of Geophysical Research: Solid Earth*, *120*(1), 450-487. doi: 10.1002/2014JB011176

Ramirez, F., Selway, K., Conrad, C. P., & Lithgow-Bertelloni, C. (2022). Constraining upper mantle viscosity using temperature and water content inferred from seismic and magnetotelluric data. *Journal of Geophysical Research: Solid Earth*, *127*, e2021JB023824. doi: 10.1029/2021JB023824

Rogozhina, I., Petrunin, A. G., Vaughan, A. P. M., Steinberger, B., Johnson, J. V., Kaban, M. K., ... Koulakov, I. (2016). Melting at the base of the Greenland ice sheet explained by Iceland hotspot history. *Nature Geoscience*, *9*, 366-369. doi: 10.1038/ngeo2689

Simonsen, S. B., Barletta, V. R., Colgan, W. T., & Sandberg Sørensen, L. (2021). Greenland Ice Sheet Mass Balance (1992–2020) From Calibrated Radar Altimetry. *Geophysical Research Letters*, *48*(3), e2020GL091216. doi: 10.1029/2020GL091216

Simpson, M. J. R., Wake, L., Milne, G. A., & Huybrechts, P. (2011). The influence of decadal- to millennial-scale ice mass changes on present-day vertical land motion in Greenland: Implications for the interpretation of GPS observations. *Journal of Geophysical Research: Solid Earth*, *116*. doi: 10.1029/2010jb007776

Steffen, R., Audet, P., & Lund, B. (2018). Weakened Lithosphere Beneath Greenland Inferred From Effective Elastic Thickness: A Hot Spot Effect? *Geophysical Research Letters*, *45*, 4733-4742. doi: 10.1029/2017GL076885

Steinberger, B., Bredow, E., Lebedev, S., Schaeffer, A., & Torsvik, T. H. (2019). Widespread volcanism in the Greenland–North Atlantic region explained by the Iceland plume. *Nature Geoscience*, *12*, 61-68. doi: 10.1038/s41561-018-0251-0

Steinberger, B., Sutherland, R., & O'Connell, R. J. (2004). Prediction of emperor-hawaii seamount locations from a revised model of global plate motion and mantle flow. *Nature*, *430*, pages167–173. doi: 10.1038/nature02660

The IMBIE Team. (2018). Mass balance of the Antarctic Ice Sheet from 1992 to 2017. *Nature*, *558*, 219-222. doi: 10.1038/s41586-018-0179-y

The IMBIE Team. (2020). Mass balance of the Greenland Ice Sheet from 1992 to 2018. *Nature*, *579*, 233-239. doi: 10.1038/s41586-019-1855-2

van Calcar, C. J., van de Wal, R. S. W., Blank, B., de Boer, B., & van der Wal, W. (preprint). Simulation of a fully coupled 3d gia – ice-sheet model for the antarctic ice sheet over a glacial cycle. doi: 10.5194/egusphere-2022-1328

Whitehouse, P. L. (2018). Glacial isostatic adjustment modelling: historical perspectives, recent advances and future directions. *Earth Surface Dynamics*, *6*, 401-429. doi: 10.5194/esurf-6-401-2018

Whitehouse, P. L., Gomez, N., King, M. A., & Wiens, D. A. (2019). Solid Earth change and the evolution of the Antarctic Ice Sheet. *Nature Communications*, *10*(503). doi: 10.1038/s41467-018-08068-y

Papers

Paper I

Modeling Viscoelastic Solid Earth Deformation Due To Ice Age and Contemporary Glacial Mass Changes in ASPECT

I

Maaike F. M. Weerdesteijn[1], John B. Naliboff[2], C. P. Conrad[1], Jesse M. Reusen[3], Rebekka Steffen[4], Jiaqi Zhang[5], and Timo Heister[5]

[1]Centre for Earth Evolution and Dynamics, University of Oslo, Oslo, Norway
[2]Department of Earth and Environmental Science, New Mexico Institute of Mining and Technology, Socorro, United States
[3]Faculty of Aerospace Engineering, Delft University of Technology, Delft, The Netherlands
[4]Lantmäteriet, Gävle, Sweden
[5]School of Mathematical and Statistical Sciences, Clemson University, Clemson, United States

Published in *Geochemistry, Geophysics, Geosystems*, March 2023, volume 24, e2022GC010813, 10.1029/2022GC010813

Key Points:

- The solid Earth is deforming in response to past and present ice loading changes at rates determined by elastic and viscous parameters
- We benchmark a new viscoelastic solid Earth deformation model in the open-source code ASPECT in combination with adaptive mesh refinement
- This code can be used to study regional Earth deformation rates from ice age and contemporary ice melt on a laterally heterogeneous Earth

Abstract

The redistribution of past and present ice and ocean loading on Earth's surface causes solid Earth deformation and geoid changes, known as glacial isostatic adjustment. The deformation is controlled by elastic and viscous material parameters, which are inhomogeneous in the Earth. We present a new viscoelastic solid Earth deformation model in ASPECT (Advanced Solver for Problems in Earth's ConvecTion): a modern, massively parallel, open-source finite element code originally designed to simulate convection in the Earth's mantle. We show the performance of solid Earth deformation in ASPECT and compare solutions to TABOO, a semianalytical code, and Abaqus, a commercial finite element code. The maximum deformation and deformation rates using ASPECT agree within 2.6% for the average percentage difference with TABOO and Abaqus on glacial cycle (∼100 kyr) and contemporary ice melt (∼100 years) timescales. This gives confidence in the performance of our new solid Earth deformation model. We also demonstrate the computational efficiency of using adaptively refined meshes, which is a great advantage for solid Earth deformation modeling. Furthermore, we demonstrate the model performance in the presence of lateral viscosity variations in the upper mantle and report on parallel scalability of the code. This benchmarked code can now be used to investigate regional solid Earth deformation rates from ice age and contemporary ice melt. This is especially interesting for low-viscosity regions in the upper mantle beneath Antarctica and Greenland, where it is not fully understood how ice age and contemporary ice melting contribute to geodetic measurements of solid Earth deformation.

Plain Language Summary

Mass changes on the Earth's surface, for example, from melting ice sheets or sea level rise, cause deflections of Earth's surface as interior rocks deform and flow. Scientists have developed models of the interior deformation resulting from loads applied to Earth's surface. Such models depend on the viscous and elastic properties of interior rocks, which quantify their capacity to deform and flow. However, because the Earth is heterogeneous, its viscoelastic properties exhibit large lateral variations that have proven difficult to accommodate within a (numerical) model. Here, we present and benchmark a new application of the open-source code in ASPECT (Advanced Solver for Problems in Earth's ConvecTion), which was originally designed to model mantle convection occurring on timescales of millions of years or longer. The ASPECT code makes use of modern numerical methods, such as adaptive mesh refinement and advanced solver techniques. In particular, we show that this code is accurate and useful for modeling solid Earth deformation occurring on timescales relevant to contemporary (in response to climate change) and ice age melting (from decades to millennia). This code is especially useful for studying regions with both past and present ice melt and a heterogeneous Earth structure, such as Greenland and Antarctica.

I.1 Introduction

Glacial isostatic adjustment (GIA) is the ongoing response of the solid Earth and the geoid to past and present changes in ice and ocean loading and produces solid Earth ground motion and mass redistributions. The solid Earth ground motion can be measured using GNSS (Global Navigation Satellite Systems) and the solid Earth mass displacements using ground-based gravimetry and satellite gravimetry, such as GRACE (Gravity Recovery and Climate Experiment). These geodetic measurements capture the ongoing response of the solid Earth to changes from both past (i.e., ice age) and contemporary ice load changes. Near areas of past and current ice cover, it is commonly thought that solid Earth ground motion results from a combination of (a) a viscous response to past ice load changes, and (b) an elastic response to contemporary ice load changes. Consequently, these geodetic measurements are either (a) corrected for the viscous response to past ice load changes, based on GIA modeling, and the remaining (assumed elastic) signal is used to constrain contemporary ice load changes (e.g. Simpson et al., 2011; Bevis et al., 2012; The IMBIE Team, 2018, 2020) or (b) corrected for the elastic response to contemporary ice load changes and the remaining viscous signal is used to constrain Earth material properties (Scheinert et al., 2021, and references therein), such as mantle viscosity and lithospheric thickness, or ice sheet histories, also using GIA models.

To correct geodetic data for the viscous response to past ice load changes, GIA models commonly assume a radially symmetric Earth structure (1D) (e.g. Whitehouse et al., 2012; Ivins et al., 2013; Roy & Peltier, 2018) as opposed to a laterally heterogeneous Earth structure (3D) (e.g. Wu et al., 1998; H. Steffen et al., 2006; Li et al., 2020; Yousefi et al., 2021; Bagge et al., 2021), and yet the Earth is characterized by lateral heterogeneities. There are indications of low-viscosity mantle or weakened lithosphere underneath Antarctica and Greenland (areas characterized by both past and contemporary ice load changes), as inferred using a variety of geophysical observations, such as seismic, magnetic, and gravity data (Martos et al., 2018; R. Steffen et al., 2018; Pappa et al., 2019; Lloyd et al., 2020; Celli et al., 2021). In the presence of a low-viscosity region in the mantle, contemporary ice load change generates not only an instantaneous elastic response but can also generate a viscous response on short timescales (Whitehouse, 2018; Weerdesteijn et al., 2022). Recent studies have explored this rapid viscous response for Antarctica (Nield et al., 2014; Bradley et al., 2015; Wolstencroft et al., 2015; Zhao et al., 2017; Barletta et al., 2018; Samrat et al., 2020, 2021) and Greenland (Simpson et al., 2011; Khan et al., 2016; van Dam et al., 2017; Milne et al., 2018; Adhikari et al., 2021). The rapid viscous response is mixed with the elastic and long-term viscous deformation components of GIA, making it difficult to distinguish between solid Earth deformation due to past and contemporary ice load changes (Whitehouse, 2018). The effect of lateral viscosity variations on solid Earth deformation (Sabadini & Portney, 1986; Kaufmann et al., 1997) and whether a 3D Earth can be represented by 1D models for glacial cycle timescales (van der Wal et al., 2013, 2015; Milne et

al., 2018; Blank et al., 2021; Marsman et al., 2021) and contemporary ice melt timescales (Powell et al., 2020) has been a long-standing question. Furthermore, recent efforts showed the need for 3D modeling to predict solid Earth deformation rates due to contemporary ice load changes near confined low-viscosity regions (Weerdesteijn et al., 2022).

In order to isolate the solid Earth deformation due to past or contemporary ice load changes, we need a modeling tool that functions from glacial cycle to decadal timescales. Furthermore, this tool needs to be able to manage large lateral heterogeneities in material properties (most importantly viscosity). Benchmark studies have been undertaken for viscoelastic solid Earth deformation models (Spada et al., 2011; Martinec et al., 2018). There are currently models that scale well for parallel computing (e.g. Latychev et al., 2005) or use regional mesh refinement (e.g. Blank et al., 2021; Wan et al., 2022). However, there are only few models that can manage large lateral viscosity variations, are open-source, and are built for high performance parallel computing. These are CitComSVE (Zhong et al., 2022) and Elmer (Zwinger et al., 2020), although the latter is not benchmarked on glacial cycle timescales.

In this study, we present a new open-source viscoelastic solid Earth deformation model in ASPECT (Advanced Solver for Problems in Earth's ConvecTion). This new model can be used for regional modeling but not for global studies, as it does not take into account gravity field changes induced by the deformation and does not solve for the gravitationally self-consistent redistribution of ocean water. ASPECT is an open-source finite element code to simulate problems in thermal convection in the Earth's mantle with large lateral variations in viscosity. We use ASPECT v2.4.0 (Kronbichler et al., 2012; Heister et al., 2017; Bangerth et al., 2022a, 2022b; Rose et al., 2017; Clevenger & Heister, 2021) published under the GPL2 license and builds on the deal.II v9.4 finite element library (Arndt et al., 2022). We compare solid Earth deformation using ASPECT to solutions using TABOO, a semianalytical code based on the normal mode method, and Abaqus, a commercial finite element code. A big advantage of ASPECT over other codes is that it uses modern numerical methods, such as adaptive mesh refinement (AMR) (demonstrated in Sections I.5.1 and I.5.2) and is built for parallel computing, also in combination with dynamically changing meshes. ASPECT can be extended by users and is under continuous development.

I.2 Numerical Model

ASPECT is a code to model convection processes in the Earth's mantle and is used for studies on, for example, subduction zone dynamics, dynamic topography, gravity field anomalies, and mantle plume dynamics (e.g. Austermann et al., 2017; Glerum et al., 2018; Dannberg & Gassmöller, 2018; Root et al., 2022). In the following sections, we describe the constitutive equations used in ASPECT and how they are modified for the purpose of modeling solid Earth deformation. We also discuss the applied boundary conditions and solvers used for our purposes.

I.2.1 Constitutive Equations

ASPECT solves a system of equations that describes viscous fluid motion driven by gravitational force differences. The compressible momentum (Equation I.1) and continuity equations (Equation I.2), also known as the compressible Stokes equations, are as follows:

$$-\nabla \cdot \left[2\eta \left(\dot{\epsilon}(\mathbf{u}) - \frac{1}{3} (\nabla \cdot \mathbf{u}) \mathbf{1} \right) \right] + \nabla p = \rho \mathbf{g} \tag{I.1}$$

$$\nabla \cdot (\rho \mathbf{u}) = 0 \tag{I.2}$$

where η is the viscosity, $\dot{\epsilon}$ the strain rate, $\mathbf{u}$ the velocity, p the total pressure, ρ the density, $\mathbf{g}$ the gravity vector, and $2\eta \left(\dot{\epsilon}(\mathbf{u}) - \frac{1}{3} (\nabla \cdot \mathbf{u}) \mathbf{1} \right)$ represents the deviatoric stress τ.

For solid Earth deformation modeling purposes, ASPECT solves the 3D Stokes equations assuming isothermal flow, the Boussinesq approximation, and incompressibility. Since incompressible flow with a linear rheology is modeled, the temperature equation (i.e., energy conservation equation) and updates to the viscoelastic stresses are decoupled from the momentum and continuity equations. Note that assuming incompressibility can reduce present-day uplift rates by up to a few percent (A et al., 2013), and that horizontal velocities from incompressible GIA models are not accurate due to the neglect of material dilatation. For solid Earth deformation modeling, we consider isothermal flow (i.e., constant temperature throughout the domain) and therefore we do not solve for the temperature equation. The Boussinesq approximation assumes that density variations are so small that they can be neglected, apart from the right-hand side of the momentum equation (Equation I.1)). Under this approximation the continuity equation (Equation I.2) reduces to the following equation:

$$\nabla \cdot \mathbf{u} = 0 \tag{I.3}$$

The same approximation to the continuity equation is obtained when incompressible flow is assumed. Furthermore, the deviatoric stress reduces to $2\eta\dot{\epsilon}(\mathbf{u})$ for incompressible flow, and thus the momentum equation becomes the following equation:

$$-\nabla \cdot [2\eta\dot{\epsilon}(\mathbf{u})] + \nabla p = \rho \mathbf{g} \tag{I.4}$$

Force terms are added on the right-hand-side of the momentum equation to account for the linear viscoelastic behavior (Section I.2.2) and boundary traction (Section I.2.3). For incompressible and isothermal flow, under the Boussinesq approximation, the momentum (Equation I.4) and continuity equations (Equation I.3) reduce to the following equations:

$$-\nabla \cdot [2\eta_{\text{eff}}\dot{\epsilon}(\mathbf{u})] + \nabla p = \rho \mathbf{g} + \nabla \cdot F_{\text{e}} + \nabla \cdot F_{\text{t}} \tag{I.5}$$

$$\nabla \cdot \mathbf{u} = 0 \tag{I.6}$$

where η_{eff} is the effective, assumed Newtonian, viscosity, F_{e} the elastic force term, and F_{t} the boundary traction force term.

I.2.2 Viscoelastic Rheology

The viscoelastic rheology is implemented through an elastic force term and an effective viscosity in the momentum equation (Equation I.5) that account for the elastic and viscous deformation mechanisms. This approach, which starts from a viscous approximation, is standard within the long-term geodynamics community (e.g. Moresi et al., 2003). Our methodology for modeling viscoelasticity in ASPECT follows the approach of Moresi et al. (2003), as outlined in Sandiford et al. (2021). Within a time step, the viscoelastic stresses are first updated using the strain rate and material properties from the previous time step. Second, the values of the viscoelastic stresses stored on the compositional fields are simultaneously advected and updated via a reaction term in the advection equation. Last, the updated stresses on the compositional fields are used to construct and solve the Stokes system (Equations I.5 and I.6) with the elastic force term and boundary traction force term (Section I.2.3). We use an implicit second-order accurate time stepping scheme (BDF2 as described in Heister et al. (2017)) for the compositional fields that keeps track of the stresses, while the nonlinearity of the viscosity is linearized using a splitting approach with a single Stokes solve (see Section 2.4).

The viscoelastic rheology is implemented through an elastic force term and an effective viscosity in the momentum equation (Equation I.5) that account for the elastic and viscous deformation mechanisms. This approach, which starts from a viscous approximation, is standard within the long-term geodynamics community (e.g. Moresi et al., 2003). Our methodology for modeling viscoelasticity in ASPECT follows the approach of Moresi et al. (2003), as outlined in Sandiford et al. (2021). Within a time step, the viscoelastic stresses are first updated using the strain rate and material properties from the previous time step. Second, the values of the viscoelastic stresses stored on the compositional fields are simultaneously advected and updated via a reaction term in the advection equation. Last, the updated stresses on the compositional fields are used to construct and solve the Stokes system (Eqs. I.5 and I.6) with the elastic force term and boundary traction force term (Sect. I.2.3). We use an implicit second-order accurate time stepping scheme (BDF2 as described in Heister et al. (2017)) for the compositional fields that keeps track of the stresses, while the nonlinearity of the viscosity is linearized using a splitting approach with a single Stokes solve (see Section I.2.4).

The velocity gradient tensor $\boldsymbol{I}^t$ and deviatoric stress tensor $\boldsymbol{\tau}^t$ are constructed from the velocity solution and stored stress components of the previous time step t. The new viscoelastic stresses are computed according to the following equation:

$$\boldsymbol{\tau}^{t+\Delta t} = \eta_{eff}\left(2\hat{\boldsymbol{D}}^{t} + \frac{\boldsymbol{\tau}^{t}}{\mu\Delta t} + \frac{\boldsymbol{W}^{t}\boldsymbol{\tau}^{t} - \boldsymbol{\tau}^{t}\boldsymbol{W}^{t}}{\mu}\right) \tag{I.7}$$

with

$$\hat{\boldsymbol{D}} = \frac{1}{2}\left(\boldsymbol{I} + \boldsymbol{I}^{T}\right) \tag{I.8}$$

$$\boldsymbol{W} = \frac{1}{2}\left(\boldsymbol{I} - \boldsymbol{I}^{T}\right) \tag{I.9}$$

$$\eta_{eff} = \eta\frac{\Delta t}{\Delta t + \alpha} \tag{I.10}$$

where superscript t and $t + \Delta t$ indicate the previous and current time step, and μ is the shear modulus describing the relation between applied force and elastic deformation. $\hat{\boldsymbol{D}}$ and $\boldsymbol{W}$ are the deviatoric rate of the deformation tensor (Equation I.8) and the spin tensor (Equation I.9), respectively, and are a function of the velocity gradient tensor. η_{eff} is the effective viscosity (Equation I.10) and is defined as a function of (material) viscosity η, time step size Δt, and shear (Maxwell) relaxation time α, where $\alpha = \eta/\mu$. In this study, we only consider linear (fixed) viscosities for each distinct compositional field. ASPECT has the option for modeling visco-elastic-plastic rheologies, with additional options for selecting dislocation creep, diffusion creep or composite viscous flow laws, but has not been benchmarked yet in combination with a free surface and boundary traction. Nonlinear rheologies affect Equation I.7 through a different definition (consisting of more terms) of the effective viscosity.

With the viscoelastic stresses of the previous and current time step, the reaction term for the deviatoric stress q is determined. As described above, lithologic layers and stresses are tracked on compositional fields. Compositional fields were originally intended to track the chemical composition of the convecting medium, but have been shown to be useful for other purposes, such as tracking materials, simulating phase changes, and tracking finite strain accumulation. For each field $c_i\left(\mathbf{x}, t\right)$, with $i = 1...C$, an advection equation is solved, which updates the stresses on the field through a reaction term q:

$$\frac{\partial c_i}{\partial t} + \mathbf{u}\cdot\nabla c_i = q_i \tag{I.11}$$

with

$$q = \boldsymbol{\tau}^{t+\Delta t} - \boldsymbol{\tau}^{t} \tag{I.12}$$

Then, the Stokes system (Equations I.5 and I.6) is constructed with the updated deviatoric stress and the elastic force term, which is defined as follows:

$$F_e = -\frac{\eta_{eff}}{\eta_e}\boldsymbol{\tau}^{t+\Delta t} \tag{I.13}$$

where η_e is the "elastic" viscosity and equals $\mu\Delta t$. A new velocity field is determined by solving the Stokes system.

I.2.3 Boundary Conditions

In this study, to allow for surface deformation, we use a free surface on the top boundary (i.e. the Earth's surface) (Rose et al., 2017). The free surface is defined as having zero normal stress on the boundary. Thus, the following condition must be satisfied: $\sigma \cdot \mathbf{n} = 0$, where $\mathbf{n}$ is the vector normal to the boundary and $\sigma = 2\eta_{\text{eff}}\dot{\epsilon}\,(\mathbf{u})$ being the total stress (i.e. the total stress is equal to the deviatoric stress since there is no pressure gradient at the top surface). When there is flow across the boundary, the mesh must be able to deform to satisfy the above condition. On the free surface, mesh velocity $\mathbf{u}_m$ is calculated as follows:

$$\mathbf{u}_m = (\mathbf{u} \cdot \mathbf{n})\,\mathbf{n} \tag{I.14}$$

Using this approach, the Eulerian advection terms need to be corrected for the mesh velocity. The momentum and continuity equations become the following equations:

$$-\nabla \cdot [2\eta_{\text{eff}}\dot{\epsilon}(\mathbf{u} - \mathbf{u}_m)] + \nabla p = \rho\mathbf{g} + \nabla \cdot F_{\text{e}} + \nabla \cdot F_{\text{t}} \tag{I.15}$$

$$\nabla \cdot (\mathbf{u} - \mathbf{u}_m) = 0 \tag{I.16}$$

Furthermore, a quasi-implicit integration scheme is used to dampen free surface position instabilities arising from small deviations in the free surface location (Rose et al., 2017).

Next to the free surface on the top boundary, we also apply a traction force to represent the surface ice loading. The ice loading is a known external force, resulting in an unknown velocity. The given pressure is applied as a force that is normal to the boundary. The lateral and bottom boundaries are free-slip boundaries. A free-slip boundary requires that the flow is tangential to the boundary, i.e. $\mathbf{u} \cdot \mathbf{n} = 0$. The boundary traction is represented as F_{t} in the momentum equation (Equation I.5).

I.2.4 Solver Options

The solution of the Stokes system can be obtained using an algebraic multigrid (AMG) solver or a matrix-free geometric multigrid (GMG) solver. While the AMG solver can solve problems on the order of ∼0.5-1.0 billion degrees of freedom (DoF) and scale efficiently on up to ∼5,000 cores, the GMG solver can solve significantly larger problems, efficiently scaling to ∼100,000 cores, and reduce memory consumption by up to a factor of 8 (Clevenger et al., 2020; Clevenger & Heister, 2021). Here, we take advantage of recent development work in ASPECT (Bangerth et al., 2022a) integrating the GMG solver with mesh deformation and elasticity, which speeds up our simulations significantly (see Section I.6). Notably, the use of the GMG solver requires element-wise averaging of the viscosity, but we found this has no noticeable effect on accuracy for a given resolution.

Three different nonlinear solving schemes can be applied for our application in the model setup. The first option is "single Advection, single Stokes" in which only one nonlinear iteration is done, that is, the compositional fields and Stokes system are solved once per time step. The second option, the "iterated Advection and Stokes" scheme iterates this decoupled approach by alternating the solution of the composition and Stokes system. The third option is "single Advection, iterated Stokes" in which the composition equation is solved once at the beginning of each time step and then iterates over the Stokes system. We experienced no improvement of free surface deformation accuracy by applying an iterated Stokes and/or iterated advection scheme. This finding is consistent for a linear and incompressible system, under the condition that the time step size and solver tolerance are sufficiently small. Thus, for computational efficiency, we use the "single Advection, single Stokes" solver scheme. The solver schemes required for a nonlinear rheology are "single Advection, iterated Stokes" or "iterated Advection and Stokes". The former solver scheme is most commonly used but theoretically iterating on both the advection and Stokes system each time step is more accurate as the fields (composition, temperature) updated during advection steps are contained within the rheological formulation.

I.3 Benchmark Study: Short and Long Timescales

Two benchmark tests are executed to validate the performance of the solid Earth deformation implementation in ASPECT with respect to two reference GIA/solid Earth deformation modeling codes, TABOO and Abaqus. Both reference codes were part of the benchmark study by Spada et al. (2011). All models use a layered Earth structure and are forced with a time-dependent surface loading. The two benchmark tests are the solid Earth deformation in response to short timescale (contemporary ice melt) and long timescale (glacial cycle) surface loading changes. The reference models and the test setup are described in the following sections.

I.3.1 Reference Models

TABOO is an open-source postglacial rebound calculator (Spada, 2003; Spada et al., 2003). The model assumes an Earth that is layered, nonrotating, incompressible, self-gravitating, spherically symmetric, and is using a linear Maxwell viscoelastic rheology. It computes the surface deformation resulting from a variable surface ice loading, using the normal mode method (Peltier, 1974, 1976; Wu & Peltier, 1982; Vermeersen & Sabadini, 1997). The surface ice loading can be set by the user. The Earth structure can be chosen from a preset selection or set by the user by changing the FORTRAN source code. This latter option requires caution as it involves changing average density and mass reference parameters, which are used in the computation of the surface spherical harmonics.

Abaqus is a commercial finite-element software package (Dassault Systèmes, 2019). Wu (2004) modified the equation of motion to include the restoring force

of isostasy as a boundary condition, such that the code is applicable to GIA problems. In this study, we use a non-axisymmetric box model geometry in Abaqus (Schotman et al., 2008), which is incompressible and non-self-gravitating (e.g., as in H. Steffen et al. (2006) or Wu et al. (2021)). For the lateral boundaries no horizontal displacement is allowed (free slip) and for the bottom boundary no displacement, neither vertically nor horizontally, is allowed (no slip). Material parameters can vary in all dimensions, similar to ASPECT.

I.3.2 Test Setup

For the benchmark tests, we use a box model geometry in ASPECT (Figure I.1a) and Abaqus, and a spherical model geometry in TABOO. The Earth structure is vertically (or radially for TABOO) symmetric, since TABOO cannot include lateral variations in material properties. We apply an elastic lithosphere, and a viscoelastic upper mantle, transition zone, and lower mantle. The horizontal dimensions are 1,500 km for ASPECT and 3,000 km for Abaqus (due to non-axisymmetry), and the vertical dimension is 2,891 km (depth of the core-mantle boundary). The horizontal dimensions are chosen such that the model geometry is sufficiently large to allow for deformation far from the load without being affected by the model lateral boundaries. The choice of horizontal dimensions is thus dependent on the size of the ice loading. The effect of the lateral boundaries on surface deformation is discussed in Appendix A.

The layer properties for the Earth model used in TABOO are given in Table I.1. This Earth model has been extensively used in GIA and solid Earth deformation code benchmarks (Spada et al., 2011; Martinec et al., 2018; Zwinger et al., 2020) and is a preset Earth model in TABOO. For ASPECT we apply the following modifications: we do not model the core (the same for Abaqus), the lithospheric viscosity is set to 10^{40} Pa s to approximate an elastic lithosphere, and we use constant gravity throughout the model of 9.815 m/s^2, while TABOO and Abaqus do include the radially/vertically changing gravity.

Table I.1: Earth model properties, as in Spada et al. (2011).

Layer	Radius R (km)	Thickness T (km)	Density ρ (kg m^{-3})	Shear modulus μ (Pa)	Viscosity η (Pa s)	Gravity g (m/s^2)
Lithosphere, L	6371	70	3037	$0.50605{\cdot}10^{11}$	∞	9.815
Upper mantle, UM	6301	350	3438	$0.70363{\cdot}10^{11}$	$1{\cdot}10^{21}$	9.854
Transition zone, TZ	5951	250	3871	$1.05490{\cdot}10^{11}$	$1{\cdot}10^{21}$	9.978
Lower mantle, LM	5701	2221	4978	$2.28340{\cdot}10^{11}$	$2{\cdot}10^{21}$	10.024
Core	3480	3480	10750	0	0	10.457

The top boundary is a free surface, the bottom boundary and lateral boundaries are free slip. By applying the lateral free-slip boundaries (e.g., only tangential flow), and a symmetric ice loading in ASPECT, the model is axisymmetric. This means that only a quarter of the full geometry needs to be simulated, saving computational resources. Abaqus models the full ice disc as the model is not axisymmetric.

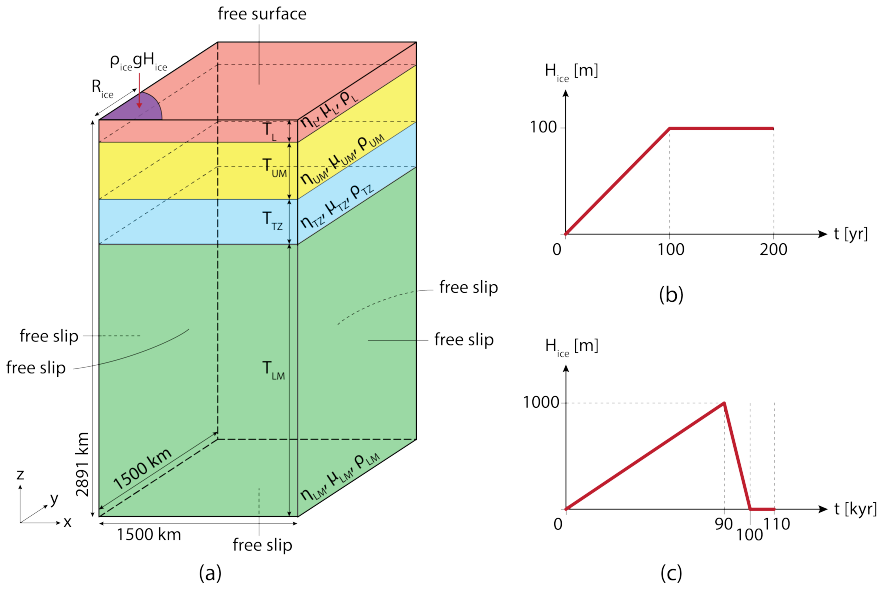

Figure I.1: (a) The box model geometry (not to scale) in ASPECT with lithosphere (red), upper mantle (yellow), transition zone (blue), lower mantle (green), boundary traction from ice loading (purple), boundary conditions, and layer material properties. (b) The ice loading height as a function of time for the short timescale simulation (contemporary ice melt). (c) The ice loading height as a function of time for the long timescale simulation (glacial cycle).

For both loading scenarios, the ice loading is a quarter disc (full disc in TABOO and Abaqus) with a spatially constant height H_{ice} (Figure I.1a). The radius of the ice disc R_{ice} is 100 km, the ice density ρ_{ice} is 931 kg/m^3, and the magnitude of the gravity at the surface is 9.815 m/s^2. For the short timescale simulation the ice height linearly increases from 0 to 100 m over 100 years, that is, 1 m/yr ice height change, which is the order of magnitude for contemporary ice melt in Antarctica and Greenland (Helm et al., 2014; The IMBIE Team, 2020), after which the height remains a constant 100 m from 100 to 200 years (Figure I.1b). The constant ice height is added to test the code performance in case of a change in surface loading rate. We choose a linear loading increase (ice growth) as opposed to decrease (ice melt), as the latter option would require an instantaneous loading at 0 years of 100 m, which is not realistic.

For the long timescale simulation, we approximate the ice height change over a glacial cycle of 110 kyr. The ice height linearly increases from 0 to 1,000 m over 90 kyr (glacial maximum), then linearly decreases to 0 m over 10 kyr, from 90 to 100 kyr (start interglacial period), after which the height remains a constant 0 m from 100 to 110 kyr (present day) (Figure I.1c). This is a rough representation of the evolution of an ice sheet during the last glacial cycle.

For the simulations in ASPECT, we make use of a constant layered mesh through time (Figure I.2). Tests with AMR are discussed in Section I.5.1. The cell size (x,y,z) in the upper 100 km is 6.25 × 6.25 × 6.02 km, and 50 × 50 × 48.18 km in the rest of the model, with a transition using 12.5 × 12.5 × 12.05 km and 25 × 25 × 24.09 km sized cells. The vertical cell dimension is slightly smaller than the horizontal cell dimension as we set 30 cells in horizontal direction (1,500 km) and 60 cells in vertical direction (2,891 km) for the initial mesh. For the simulations in Abaqus the mesh is also constant through time. The horizontal resolution is 5 km close to the ice loading (a square of 400 × 400 km centered around the load), and 200 km elsewhere. The vertical resolution varies from 8.75 to 277.625 km, increasing with depth (8 elements per layer). In ASPECT, we use quadratic continuous 3D finite elements (27 nodes) for the velocity with 3 DoF per node and linear continuous 3D finite elements (8 nodes) for the pressure with 1 DoF per node. In Abaqus linear continuous 3D finite elements (8 nodes) are used with 3 DoF per node for the velocity and 1 DoF per node for the pressure. The spectral resolution in TABOO with a maximum degree of 4,096 corresponds to ∼5 km resolution. In ASPECT the time step size for the short timescale simulation is 2.5 years and for the long timescale simulation is 50 years. From trial and error we found that smaller time step sizes do not yield more accurate results.

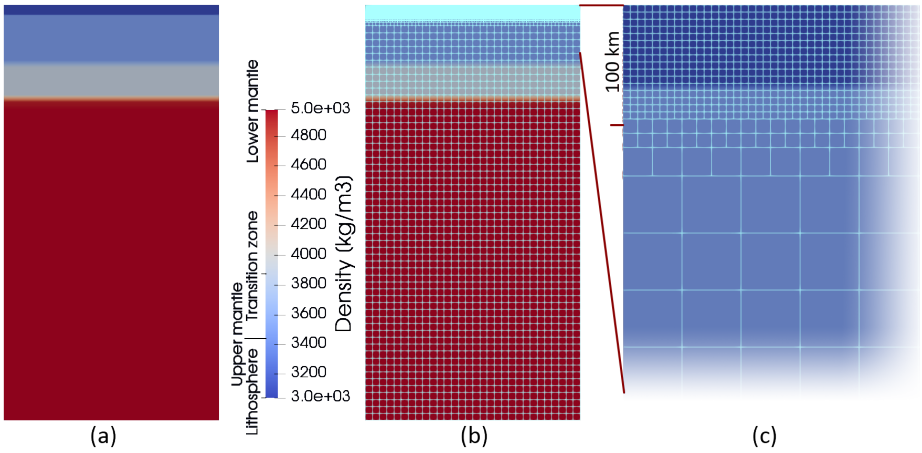

Figure I.2: (a) Front view of the box geometry in ASPECT with density variations with depth. (b) Same as (a) but with overlain mesh. (c) Same as (b) but zoomed in to see the mesh cells size changing from ∼50 km to ∼6.25 km in the upper 100 km of the model.

I.4 Benchmark Results and Model Performance

Here we present the benchmark results for the short timescale simulation (Section I.4.1) and the long timescale simulation (Section I.4.2), and a discussion on the models performances (Section I.4.3).

I.4.1 Short Timescale Simulation

The largest vertical surface deformation is, as expected, found underneath the load center, and the location of largest deformation gradient coincides with the boundary of the ice disc at 100 km distance (Figure I.3a). Most deformation takes place over the first 100 years, when the ice load increases, followed by 100 years of slower surface deformation increase due to the constant loading, also visible in the abrupt kink in deformation amplitudes and rates (Figures I.3b and I.3c). From a first view, the deformation profiles (Figure I.3a) look very similar among codes. Deviations between codes can be seen in the far field, where boundary effects may play a role for ASPECT and Abaqus (Appendix A). Furthermore, ASPECT under- or overshoots the deformation rate at times of ice loading changes, but quickly converges to the solutions from TABOO and Abaqus (Figure I.3c, right). Recent testing suggests that the following components of the numerical implementation may contribute to the under- and overshoots but would require further testing to isolate the exact contributing factors: the order in which stresses are updated, the time stepping scheme (we refer to details on the "elastic" time step in Moresi et al. (2003) and Sandiford et al. (2021)) or something intrinsic to storing and advecting stresses on compositional fields. We calculate the average absolute difference and average percentage difference according to the following equations:

$$\text{average absolute difference} = \frac{\sum_n |\mathbf{a_n} - \mathbf{b_n}|}{|\mathbf{a}|} \tag{I.17}$$

$$\text{average percentage difference} = \frac{\sum_n \left(|\mathbf{a_n} - \mathbf{b_n}|\right) / |\mathbf{b_n}|}{|\mathbf{a}|} \cdot 100\% \tag{I.18}$$

where $\mathbf{a}$ and $\mathbf{b}$ are arrays with n elements (time steps) with the deformation or deformation rate solutions, $\mathbf{a}$ is the ASPECT solution, and $\mathbf{b}$ the TABOO or Abaqus solution. The maximum vertical surface deformation is very similar between ASPECT, TABOO and Abaqus (Figure I.3b), and the average percentage difference at the load center over 200 yrs is only 0.28% between ASPECT - TABOO (Table I.2). For all distances from the load center (0, 100, and 250 km) the average absolute difference in deformation between ASPECT - TABOO and ASPECT - Abaqus is smaller than 0.01 m (Figure I.3c, left), with the largest average percentage difference (10.64%) at 250 km between ASPECT - TABOO (Table I.2). However, the deformation at 250 km is already considerably smaller because of the distance from the load (-0.075 m at 250 km as opposed to -0.75 m underneath the load center after 200 yrs). For the deformation rate we

see constant deviations until the end of the load increase at 100 yrs, after which the solutions for ASPECT and TABOO are within 0.0003 mm/yr from each other at 200 yrs (Figure I.3c, right). The largest average percentage difference in deformation rate are found at 250 km (Table I.2). Again, the deformation rate is considerably smaller at 250 km compared to 100 and 0 km (underneath the load center). The average percentage difference in deformation and deformation rate between ASPECT - Abaqus at 250 km, 2.25 and 2.30% respectively, are much smaller than compared to TABOO (Table I.2), which suggests this is due to the influence of the lateral boundaries (I.7) or sphericity and self-gravitation (Appendix B). Overall, underneath the load center we see average percentage differences of deformation and deformation rates between ASPECT - TABOO and ASPECT - Abaqus within 1.4% of each other, and within 3.0% at the load boundary at 100 km distance.

Table I.2: Average absolute and percentage difference of vertical surface deformation and deformation rate at different distances from the load center between ASPECT and TABOO and ASPECT and Abaqus for the short timescale simulation.

	ASPECT - TABOO			
	Deformation		Deformation rate	
Distance from load center [km]	Avg. absolute difference [m]	Avg. percentage difference [%]	Avg. absolute difference [mm/yr]	Avg. percentage difference [%]
0	0.0009	0.28	$2.01{\cdot}10^{-4}$	1.38
100	0.0062	2.25	$5.60{\cdot}10^{-4}$	2.66
250	0.0061	10.64	$4.90{\cdot}10^{-4}$	11.47
	ASPECT - Abaqus			
	Deformation		Deformation rate	
Distance from load center [km]	Avg. absolute difference [m]	Avg. percentage difference [%]	Avg. absolute difference [mm/yr]	Avg. percentage difference [%]
0	0.0041	0.91	$3.38{\cdot}10^{-4}$	0.84
100	0.0083	2.92	$6.06{\cdot}10^{-4}$	1.95
250	0.0009	2.25	$8.41{\cdot}10^{-5}$	2.30

I.4.2 Long Timescale Simulation

The vertical surface deformation in the long timescale simulation is larger than in the short timescale simulation because of the 10 times larger maximum ice height. The deformation increases up to 90 kyr, after which it decreases drastically (Figure I.4), which is consistent with the change in applied surface loading. The maximum vertical surface deformation is very similar between ASPECT, TABOO, and Abaqus (Figure I.4b). ASPECT models a slightly larger maximum surface deformation (-64.5 m) than TABOO (-63.8 m) and Abaqus (-63.5 m) at the ice height maximum at 90 kyr (Figure I.4b) and also after 110 kyr, -10.8 m for ASPECT, -9.7 m for TABOO, and -9.9 m for Abaqus. The average percentage difference over 110 kyr is less than 1.3% for both the deformation and deformation rate at 100 km distance and underneath the load

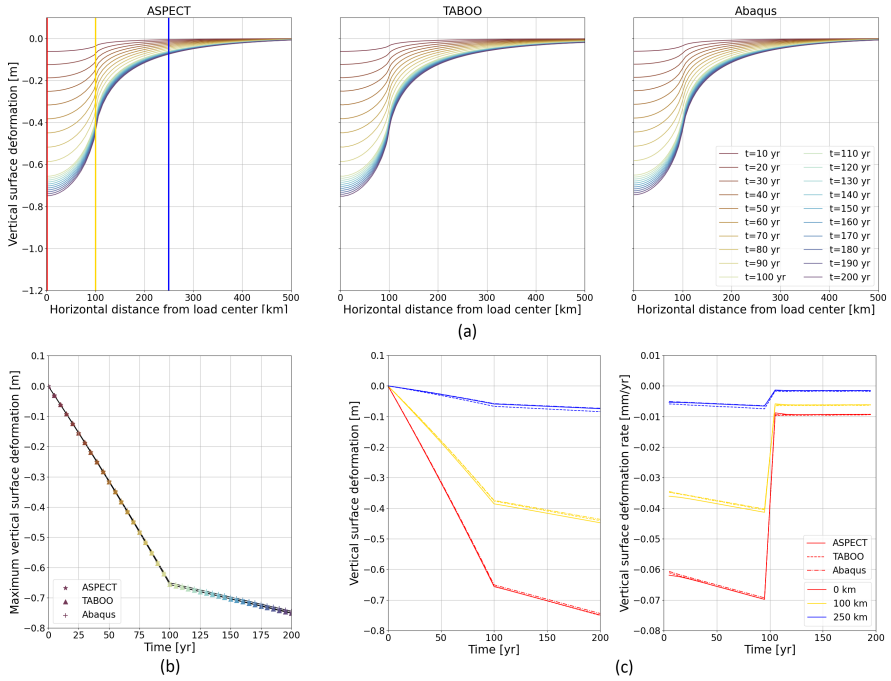

Figure I.3: Short timescale simulations: (a) Vertical surface deformation as function of the horizontal distance from the load center along $y = x$ at different time intervals (colors) for ASPECT (left), TABOO (middle), and Abaqus (right), with vertical lines at 0 km (red), 100 km (yellow), and 250 km (blue). (b) Maximum vertical surface deformation for ASPECT (stars), TABOO (triangles), and Abaqus (pluses), with marker colors corresponding to the times in plot (a). (c) Maximum vertical surface deformation (left) and maximum vertical surface deformation rate (right) as function of time for ASPECT (solid line), TABOO (dashed line), and Abaqus (dash-dotted line) at 0 km (red), 100 km (yellow), and 250 km (blue) distance from the load center.

center between ASPECT and TABOO and less than 2.8% between ASPECT and Abaqus (Table I.3). Again, the largest difference between ASPECT and TABOO we see further away from the ice load at 250 km distance (Figure I.4c, blue lines, and Table I.3). Also for the long timescale simulation, the average percentage difference in deformation and deformation rate between ASPECT and Abaqus at 250 km, 2.29% and 3.72% respectively, is much smaller than compared to TABOO (Table I.3). Overall, underneath the load center, we see average percentage differences of deformation and deformation rates between ASPECT–TABOO and ASPECT–Abaqus within 2.6% of each other and within 2.8% at the load boundary at 100 km distance. The deformation and deformation rate differences between the models are consistent for the short and long timescale simulations.

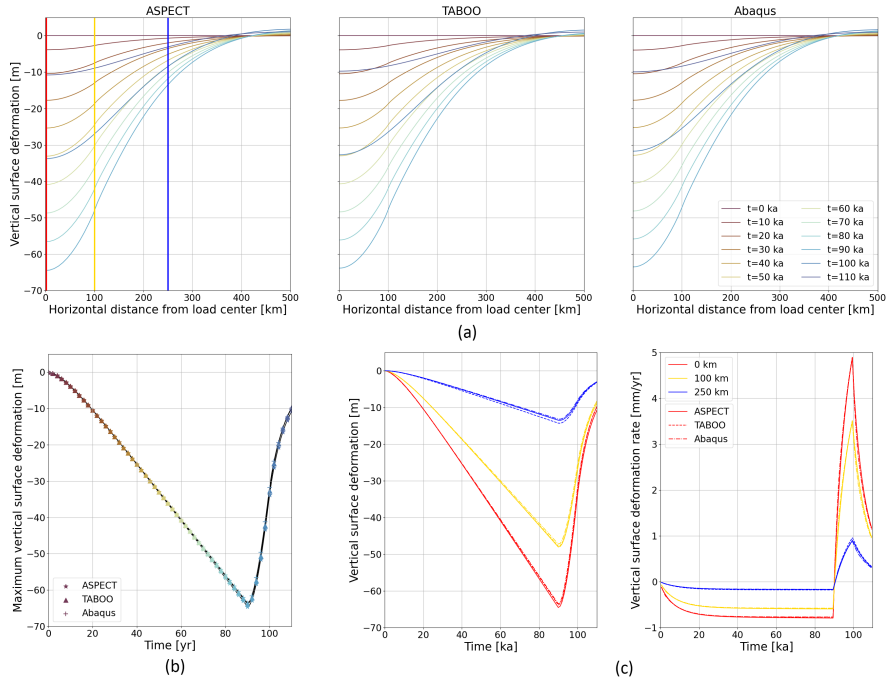

Figure I.4: Long timescale simulations: (a) Vertical surface deformation as function of the horizontal distance from the load center along $y = x$ at different time intervals (colors) for ASPECT (left), TABOO (middle), and Abaqus (right), with vertical lines at 0 km (red), 100 km (yellow), and 250 km (blue). (b) Maximum vertical surface deformation for ASPECT (stars), TABOO (triangles), and Abaqus (pluses), with marker colors corresponding to the times in plot (a). (c) Maximum vertical surface deformation (left) and maximum vertical surface deformation rate (right) as function of time for ASPECT (solid line), TABOO (dashed line), and Abaqus (dash-dotted line), at 0 km (red), 100 km (yellow), and 250 km (blue) distance from the load center.

I.4.3 Model Performance

The deformation solutions do not perfectly agree due to model differences, which will be discussed here. As mentioned earlier, the mesh resolution, both vertically (or radially) and horizontally (or laterally) varies for each model. An increase in consistency in model meshes is expected to improve model comparisons. Furthermore, TABOO is fully spherical, while ASPECT and Abaqus are box models and have lateral boundaries. The lateral boundaries are closed (e.g., no material inflow and outflow), which causes material to move vertically along these boundaries. To minimize this effect, it is important to choose a large model

Table I.3: Average absolute and percentage difference of vertical surface deformation and deformation rate at different distances from the load center between ASPECT and TABOO for the long timescale simulation.

ASPECT - TABOO				
	Deformation		Deformation rate	
Distance from load center [km]	Avg. absolute difference [m]	Avg. percentage difference [%]	Avg. absolute difference [mm/yr]	Avg. percentage difference [%]
0	0.327	1.21	$1.11{\cdot}10^{-2}$	1.11
100	0.137	0.79	$6.58{\cdot}10^{-3}$	0.78
250	0.381	5.80	$1.28{\cdot}10^{-2}$	5.82
ASPECT - Abaqus				
	Deformation		Deformation rate	
Distance from load center [km]	Avg. absolute difference [m]	Avg. percentage difference [%]	Avg. absolute difference [mm/yr]	Avg. percentage difference [%]
0	0.526	1.95	$3.13{\cdot}10^{-2}$	2.52
100	0.420	1.93	$2.36{\cdot}10^{-2}$	2.71
250	0.157	2.29	$8.10{\cdot}10^{-3}$	3.72

horizontal dimension with respect to the load size (Appendix A). Moreover, TABOO is self-gravitating, whilst ASPECT and Abaqus are non-self-gravitating. Amelung and Wolf (1994) and Wu and Johnston (1998) compared surface deformation following ice age loading for a spherical Earth and a non-spherical Earth approximation and showed that the effects of sphericity and self-gravitation partly cancel each other out. They found that surface deformation results are sufficiently accurate with a non-spherical Earth approximation for Fennoscandian-sized ice sheets and also for Laurentide-sized ice sheets but the non-spherical Earth approximation accuracy decreases in the periphery of the ice sheet. Ivins and James (1999) showed similar results and found sufficiently accurate results (generally ∼1% difference, and ∼10% in the periphery between spherical and non-spherical Earth) for ice sheets up to 20° in size. We show comparable results between ASPECT and TABOO for wider surface loads (Appendix B), making ASPECT suitable for regional solid Earth deformation modeling. Also, for model horizontal dimensions larger than 1,500 km for the numerical models, we see an additional small deviation (<1%) compared to TABOO (see Appendix A), which will affect percentage deviations. In ASPECT, we use constant gravity within the 3D box geometry, but TABOO and Abaqus employ variable gravity. As most material movement following ice loading changes takes place in the upper mantle, we do not expect a significant effect of the constant gravity assumption on the solid Earth deformation solution as gravity reduces by only 1.7% from the surface to the bottom of the transition zone (Table I.1). Lastly, ASPECT uses quadratic finite elements, while Abaqus uses linear elements. Quadratic elements improve accuracy as they deform more realistically and capture more geometric detail with fewer elements. Generally, despite these differences, the models show a very good agreement, which gives confidence in the performance of our new solid Earth deformation model in ASPECT.

I.5 Benchmark Variations: Adaptive Mesh Refinement and Lateral Heterogeneous Viscosity

In this section, we apply changes to the original short timescale benchmark test to demonstrate the use of adaptive mesh refinement in ASPECT (Section I.5.1), and we demonstrate that ASPECT can manage large lateral viscosity variations in combination with an adaptive mesh (Section I.5.2).

I.5.1 Adaptive Mesh Refinement

Here, we demonstrate the use of adaptive mesh refinement (AMR) for GIA/solid earth deformation studies. AMR has the advantage of using a different regionally refined mesh at every time step. This is especially useful for Antarctica where in some areas most of the ice history is not well constrained for older times and ice history resolution is increased for more recent times. These areas could be modelled with a coarse resolution when the ice history is not well constrained, and with a more refined mesh resolution at times of higher resolution ice history. This allows for faster computation of the entire loading history.

In order to use ASPECT's AMR capabilities in combination with a free surface, we need to apply a constant density throughout the domain. With a laterally varying mesh, the vertically varying density is not equally represented laterally and free surface instabilities arise. In Appendix C we analyze the model performance with a constant density instead of a density profile without AMR and the effect of the density magnitude on surface deformation. However, glacially induced stresses largely depend on the density distribution (see the equations in Wu (2004)) and an increased density for the crust would result in enlarged and inaccurate stresses. To test AMR, we set the constant density equal to the volume-averaged mantle density of the Earth model density profile, 4491.76 kg/m^3. ASPECT's mesh refinement criterion is based on the strain rate norm at the center of each cell. The cells with the smallest error in strain rate norm, accounting for 5% of the total error, are flagged for coarsening, and the cells with the largest error, accounting for 30% of the total error, are flagged for refinement at each time step. With the AMR functionality, ASPECT balances the solution accuracy and computational resources for the simulation. The size of the near cubical cells varies between 50 and 6.25 km (Figure I.5).

The difference in vertical surface deformation and deformation rates between the constant layered mesh and the adaptive mesh is small (Figure I.6) and of the same order as the differences between ASPECT-TABOO and ASPECT-Abaqus (Figure I.3). The constant layered mesh simulation takes 74 min 14 s ($\sim$111 million DOF), and the AMR simulation takes 63 min and 32 s ($\sim$9 million DOF), $\sim$15% faster (on 512 CPU). The largest differences in computation time come from the speed-up of building the Stokes and composition systems (fewer cells and thus fewer integration points for the adaptively refined mesh) and the slow-down associated with redefining the mesh structure. We refine the mesh

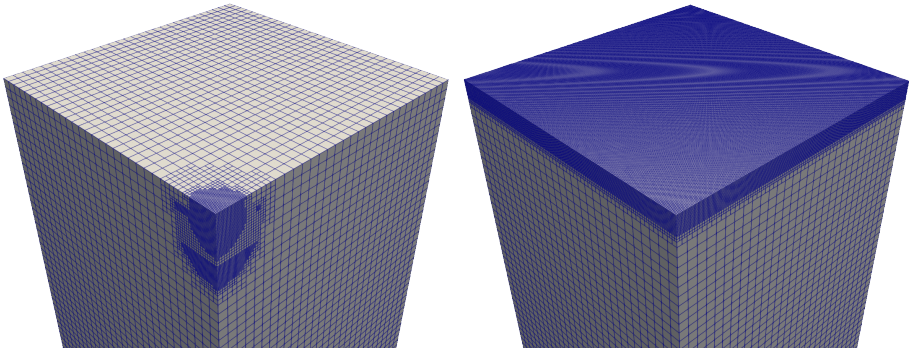

Figure I.5: (left) The mesh at 200 yrs with adaptive mesh refinement and (right) with a constant layered mesh through time, with cell sizes ranging between ∼50 and ∼6.25 km

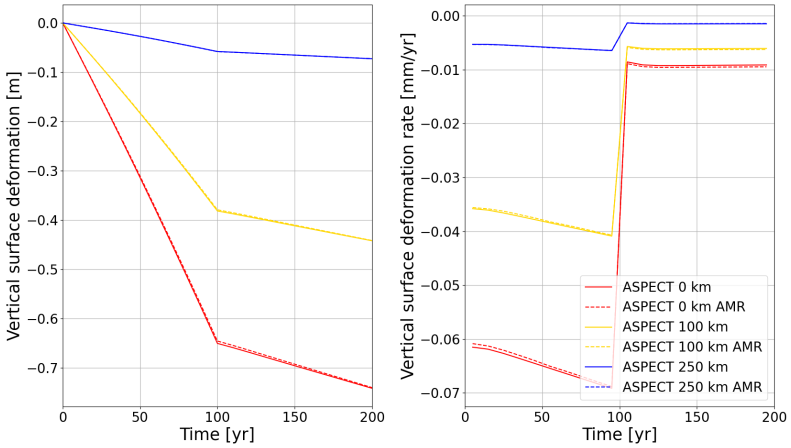

Figure I.6: Maximum vertical surface deformation (left) and rate (right) as function of time for ASPECT with the constant layered mesh (solid line), and ASPECT with the adaptively refined mesh (AMR) (dashed line), at 0 km (red), 100 km (yellow), and 250 km (blue) distance from the load center.

every time step, which is expensive. The runtime can be further reduced by doing the AMR during fewer steps, and by optimizing the AMR criteria based on strain rate when no boundary traction is present at time zero (the mesh starts out refined, ∼113 million DOF, and focuses onto areas with active boundary tractions in the following time steps). We recommend using AMR for solid earth deformation applications, because of the potentially considerable speed-up of the simulation while maintaining the same accuracy of the solution compared to using a constant mesh through time.

I.5.2 Lateral Heterogeneous Viscosity

The Earth is laterally heterogeneous, and therefore there is a need for solid earth deformation and GIA codes that can include lateral variations in earth material properties. Here, we demonstrate the code performance in the presence of a low-viscosity region underneath the ice load, in combination with AMR. We use the same earth model as in the previous section, but include a (quarter) cylindrical shaped low-viscosity region underneath the ice load. The low-viscosity region radius is 100 km, the viscosity is $1{\cdot}10^{19}$ Pa s, the upper depth is 70 km (boundary between upper mantle and lithosphere), and the lower depth is 170 km (thickness is 100 km). We compare ASPECT with Abaqus, as TABOO cannot include lateral variations in material properties. The constant density is 4,491.76 kg/m^3 and the shear modulus of the low-viscosity region remains equal to that of the upper mantle (70.363 GPa). The refinement criteria are the same as in the previous test: the cells with the smallest error in strain rate norm, accounting for 5% of the total error, are flagged for coarsening, and the cells with the largest error, accounting for 30% of the total error, are flagged for refinement at each time step.

Table I.4: Average absolute and percentage difference of vertical surface deformation and deformation rate at different distances from the load center between ASPECT and Abaqus for the short timescale simulation with a low-viscosity region.

	Deformation		Deformation rate	
Distance from load center [km]	Avg. absolute difference [m]	Avg. percentage difference [%]	Avg. absolute difference [mm/yr]	Avg. percentage difference [%]
0	0.009	1.18	$1.91{\cdot}10^{-3}$	8.05
100	0.010	2.71	$8.71{\cdot}10^{-4}$	4.70
250	0.001	2.30	$1.30{\cdot}10^{-4}$	8.37

The mesh is refined based on the strain rate and shows a finer refinement at the location of the surface load and the low-viscosity region, where material flows faster than elsewhere (Figure I.7a). Due to the low-viscosity region, for the same loading scenario, the maximum vertical surface deformation (-1.23 m, Fig I.7c) is larger than for the layered solution (-0.75 m, Figure I.3b). The deformation profiles of ASPECT and Abaqus look similar (Figure I.7b), but on closer inspection the maximum vertical surface deformation solutions do deviate (Figure I.7c) with an average percentage difference of 1.18% (Table I.4). Generally, the ASPECT deformation and deformation rate is larger than the Abaqus solution. The average percentage difference for the deformation is within 2.8% for all distances. The deformation rate shows larger deviations, up to 8.4%.

Here, we illustrate some of the reasons that the codes provide similar, but different solutions in the presence of a lateral viscosity jump. Previously ASPECT and Abaqus runs utilized the same density profile. Here we use an adaptive mesh which requires a constant density throughout the domain in combination with the free surface. The constant density results in a maximum difference of 2.7%

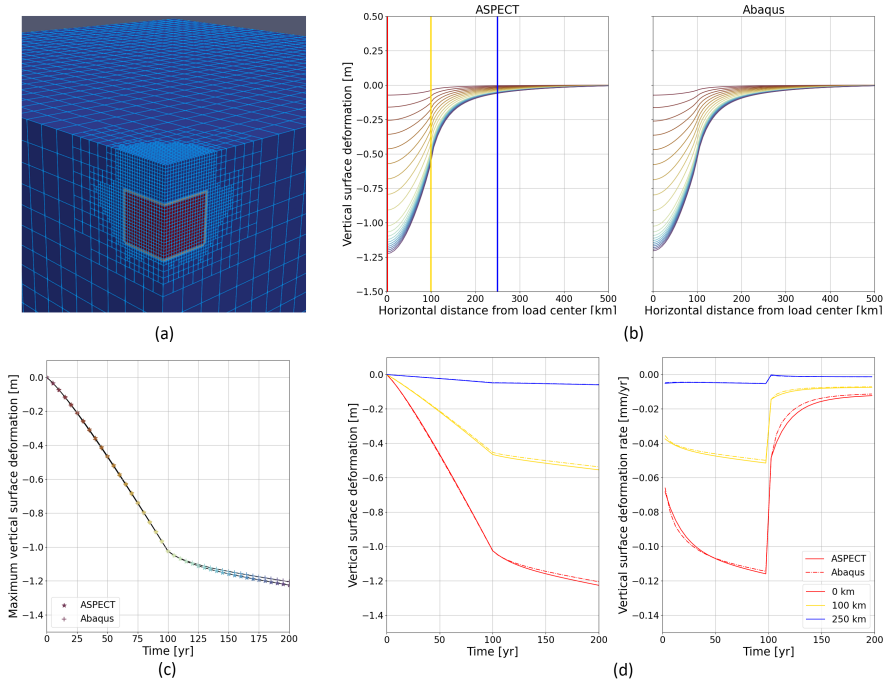

Figure I.7: Low-viscosity region short timescale simulations: (a) the mesh in ASPECT after 200 years (light blue) with the low-viscosity region (red). (b) Vertical surface deformation as function of the horizontal distance from the load center along $y = x$ at different time intervals (colors) for ASPECT (left) and Abaqus (right), with vertical lines at 0 km (red), 100 km (yellow), and 250 km (blue). (c) Maximum vertical surface deformation for ASPECT (stars) and Abaqus (pluses), with marker colors corresponding to the times in plot (b). (d) Maximum vertical surface deformation (left) and maximum vertical surface deformation rate (right) as function of time for ASPECT (solid line) and Abaqus (dash-dotted line), at 0 km (red), 100 km (yellow), and 250 km (blue) distance from the load center.

for the deformation and deformation rate over all distances with respect to the density profile (Appendix C). Furthermore, ASPECT uses quadratic elements for the velocity and linear elements for the pressure, whereas in the Abaqus simulations linear elements are applied. In ASPECT, on the boundary of the low-viscosity region, the viscosity value is interpolated between the values inside and outside the low-viscosity region, resulting in a linear change of the viscosity over an element (possible due to the quadratic element with nodes in the center of the vertices). This is not only true for the lateral extent of the low-viscosity region but also for the thickness, and the spatial representation of the layers with depth. The difference in the order of the elements comes with a slightly different representation of the earth model, but of course also a change in computational

resources. The simulation in ASPECT takes 55 min and 0 s on 256 CPU, whereas the simulation in Abaqus takes 514 min and 59 s on 16 CPU, which is ∼1.7 times faster than ASPECT when dividing the ASPECT run time by 16 to normalize the number of CPUs used (note that ASPECT only models a quarter of the geometry due to axisymmetry). Abaqus is commercial software that is highly optimised for (elastic) deformation problems, and thus it is no surprise that Abaqus runs faster. However, Abaqus is limited in its geoscientific applications, whereas the open-source code ASPECT expands its applications in the realms of thermal convective flow. Despite the fundamental differences in these finite element codes, we see a reasonable agreement for the surface deformation and deformation rates. We demonstrate the use of AMR in ASPECT with laterally heterogeneous earth models. This is a powerful tool when one wants to model several surface loads at different locations that change at different times.

I.6 Scaling and Material Averaging

In this section, we use the model setup as in Section I.4.1 to perform scaling tests and compare the performance of key components of the geometric multigrid (GMG) and algebraic multigrid (AMG) solvers. In addition, we study the effects of different viscosity averaging schemes as they are required when using the GMG solver. Our goal is to demonstrate the performance advantages of GMG and to find the number of processors that can be used for a particular problem size, where the methods still scale.

The GMG method requires solving the same problems on coarser meshes, but viscosity generally only exists on the finest mesh, therefore we need to transfer it from the fine mesh to the coarser meshes. ASPECT currently provides multiple options to achieve this. Here, we consider the two options that provide the most (harmonic average) or least (Q1 projection) amount of smoothing between the meshes. The first one is “harmonic average only viscosity”, where viscosity on coarse cells is a piece-wise constant per cell computed by the harmonic average of viscosity values at quadrature points on the finest cells. The second one is “project to Q1 only viscosity”, which is a cell-wise projection from the viscosity on the finest cells from quadrature points to a Q1 polynomial space, which is then transferred to the coarse cells.

The total number of DoF is ∼111 million and the Stokes system owns 26 million of them. Both GMG and AMG take about 40 GMRES (generalized minimal residual method) iterations to converge regardless of the number of cores and viscosity averaging methods. We observe that the AMG solver is not sensitive to different viscosity averaging schemes in these scaling tests, and we thus skip the results of the AMG solver without averaging viscosity. Table I.5 show the runtime in time step 1 of the three important components of the solvers (“Setup”, “Assembly”, “Stokes solve”). Both GMG and AMG have similar scaling efficiency. The optimal scaling range is near 500 cores, leading to around 50,000 DoF per core.

The “Setup” part includes setting up all the sparsity patterns, distributing the degrees of freedom, and for GMG, it also includes initializing the data structures for the matrix-free multilevel transfer. Note that we only need this “Setup” part whenever the mesh is refined or coarsened. If a fixed mesh is used, everything in this part should be done in time step 0 only. GMG is about 1.7× faster than AMG for the setup, since it does not need to build any sparsity patterns for the Stokes equations. The “Assembly” part includes the runtime for all the matrix and vector assembly and preconditioner construction. For AMG, the matrices include the system matrix, preconditioner matrix, and preconditioner setup, while the GMG method only assembles the right hand side of the linear system and computes necessary data on coarser levels. Here, GMG is at least 3.4× faster than AMG. Combining “Assembly” and “Stokes solve”, GMG is at least 2.6x faster than AMG. Switching to harmonic averaging of the viscosity saves another 20% of the runtime (see Table I.5). To work with AMR using GMG, one will have to consider the workload imbalance defined in Clevenger et al. (2020), which is caused by the unfair partition of the mesh. With 2,240 cores, this mesh produces an imbalance of 2.8 due to the heavy refinement at the surface. One can expect the GMG solver to be up to 2.8 times faster, if the mesh was globally refined like in the strong scaling results in Clevenger and Heister (2021).

Other important parts of the runtime include the assembly and solution of the compositional fields, mesh deformation, and temperature. More than 50% of the total runtime is spent in the assembly of the 10 compositional fields. Note that when the GMG solver is used, the matrix-free GMG method is used to solve for the mesh displacement, which is at least 3× faster than AMG and scales more efficiently, but it only takes about 1% of the total runtime. The temperature field takes about 5% of the total runtime to assemble and solve (the temperature equation is still solved although temperature is constant in our simulations). All the other parts not shown here contribute to less than 1% of the total runtime. Overall, using GMG can be at least 1.2× faster. Using GMG with harmonic average on 2,240 cores produces the greatest speedup, which is 1.5× faster than AMG in the total runtime in time step 1 as indicated in the first row in Table I.5 for the harmonic averaging. Significantly, we observe almost no change in accuracy when varying between the AMG and GMG solvers, or viscosity averaging method (Table I.6).

Table I.5: Runtime [s] of the key components in the GMG and AMG solvers using using Q1 projection and harmonic averaging for viscosity.

	Q1 projection of viscosity							
Number of processors	280		560		1,120		2,240	
Stokes DoFs/core	93,602		46,801		23,401		11,700	
Solver	GMG	AMG	GMG	AMG	GMG	AMG	GMG	AMG
Total	118.0	143.0	64.0	80.0	36.5	48.0	22.1	30.4
Setup	8.8	15.3	6.1	10.3	4.4	7.5	3.0	4.8
Assembly	4.5	15.1	2.4	8.5	1.3	5.0	0.7	3.4
Stokes Solve	6.7	14.3	3.6	7.5	2.4	4.7	1.8	3.5
Assembly + Stokes Solve	11.2	29.4	6.1	16.0	3.7	9.7	2.5	6.9
GMG speedup	2.6	-	2.6	-	2.6	-	2.8	-
	Harmonic averaging of viscosity							
Number of processors	280		560		1,120		2,240	
Stokes DoFs/core	93,602		46,801		23,401		11,700	
Solver	GMG	AMG	GMG	AMG	GMG	AMG	GMG	AMG
Total	106.0	136.0	59.0	75.0	34.2	46.0	20.5	30.7
Setup	9.0	15.5	6.0	10.2	4.4	7.4	3.0	5.3
Assembly	3.9	14.6	2.1	7.9	1.2	4.9	0.7	3.2
Stokes Solve	5.0	14.3	2.8	7.6	1.7	4.6	1.4	3.7
Assembly + Stokes Solve	8.9	28.9	4.9	15.5	2.9	9.5	2.1	6.9
GMG speedup	3.3	-	3.2	-	3.3	-	3.3	-

Table I.6: Maximum deformation after 5 years and difference relative to the TABOO solution (-0.0305 m) for Abaqus and for 5 different combinations of the Stokes solver type and material averaging for ASPECT.

Solution	Material averaging	Maximum deformation [m]	Difference relative to TABOO [%]
AMG	None	-0.0309442	+1.456
	Q1	-0.0308437	+1.127
	Harmonic	-0.0309272	+1.401
GMG	Q1	-0.0309081	+1.338
	Harmonic	-0.0309124	+1.352
Abaqus		-0.0301383	-1.186

I.7 Conclusion

In this study, we benchmark a new viscoelastic solid earth deformation model in ASPECT. ASPECT is a finite-element based code originally built for mantle convection studies. Unlike most other solid earth deformation codes, it has all of the following advantages: it is open-source, built for parallel computing, has AMR capabilities, and can be extended by users. This new model can be used for regional modeling, but not yet for global GIA studies, as it does not take into account gravity field changes induced by the deformation and does not solve for the gravitationally self-consistent redistribution of ocean water. We show the performance of earth deformation in ASPECT and compare solutions to

TABOO, a semi-analytical code based on the normal mode method, and Abaqus, a commercial finite element code. We show that the maximum deformation and deformation rates in ASPECT agree within 2.6% for the average percentage difference with TABOO and Abaqus on glacial cycle and contemporary ice melt timescales. This gives confidence in the performance of our new solid earth deformation model in ASPECT.

We show the performance of an adaptively refined mesh in ASPECT, which is a great advantage for solid earth deformation modeling. Here, we model one cylindrical ice load. However, over a glacial cycle, and also for contemporary ice melt, surface loads increase or decrease at different rates and at different locations within the model domain. With the AMR capability and differently changing ice loads across the domain, we can model earth deformation and speed up the computation considerably, saving computational resources by not requiring a highly refined mesh over regions where no large surface ice load changes occur. Furthermore, we show a good fit to Abaqus solutions comparing ice-load-induced deformations above a laterally confined low-viscosity region, which supports the applicability of ASPECT for regional solid earth deformation problems with lateral variations in earth structure. Lastly, we report on the parallel scalability of the code, which is useful information for new users.

This benchmarked code can now be used to investigate the earth deformation rates from past ice melt (ice age melting, long timescale), and contemporary ice melt (short timescale). This is especially interesting in areas of low-viscosity regions in the upper mantle beneath Antarctica and Greenland, where it is not fully understood how much ice age melting and contemporary ice melt contribute to modern geodetic measurements of earth deformation (from GNSS). Or in other words, we can use ASPECT to estimate mantle viscosity from GNSS measurements in combination with an ice sheet evolution model over the last glacial cycle and observations of contemporary ice mass change.

Furthermore, ASPECT offers great flexibility to implement new code parts. We can for example, investigate the effect of nonlinear rheology on earth deformation, such as time-dependent (e.g. transient) and stress-dependent viscosity (Adhikari et al., 2021; Blank et al., 2021; Lau et al., 2021), or the effect of anisotropic viscosity (Han & Wahr, 1997). This benchmark study is performed for a 3D box geometry, and developments are under way to solve for GIA in a 3D spherical geometry. Future development work will include adding self-gravitation to ASPECT, which already supports an option for variable gravity, and solving the sea level equation, which involves implementing geoid changes, rotational feedback, shoreline migration, and associated ocean load redistributions. These developments will allow ASPECT to join a small suite of numerical 3D spherical GIA models.

Appendix A: Model Horizontal Dimension

In the benchmark test the horizontal dimensions are 1,500 km for an ice load of 100 km radius. The lateral boundaries far from the load are free-slip boundaries (e.g. only tangential flow). In a spherical world these boundaries do not exist. These boundaries can affect the material flow and thus the free surface deformation significantly. We wish to minimize the effect of the boundaries on the material flow, for an accurate representation of the surface deformation. Here, we demonstrate the effect the far lateral boundaries have by varying the model's horizontal dimension from 500 to 3,000 km (i.e. 5 times to 30 times the load radius).

The maximum vertical surface deformation for models with different model widths at 200 years decreases with an increase in model width (Figure I.A.1). Convergence to a maximum vertical surface deformation is reached with an increase in model width. Thus, the lateral boundaries affect surface deformation, and thus material flow, less for a wider model, as expected. The model width is an important consideration for balancing between model accuracy and computational resources. We performed the model tests with a 1,500 km model width, resulting in a maximum deformation of -0.749 m, which is 1.2% off w.r.t. a model width of 3,000 km (Figure I.A.2). Note that the model width has a large impact on the surface deformation when chosen too small (500 km width for a 100 km radius load). Model widths of 15 times the load radius (i.e. 1,500 km), used in this study, or larger, result in surface deformation and deformation rates within 1.4% of the solution using TABOO, and within 3.2% of the solution using TABOO for model widths of 10 times the load radius (i.e. 1,000 km) (Figure I.A.2).

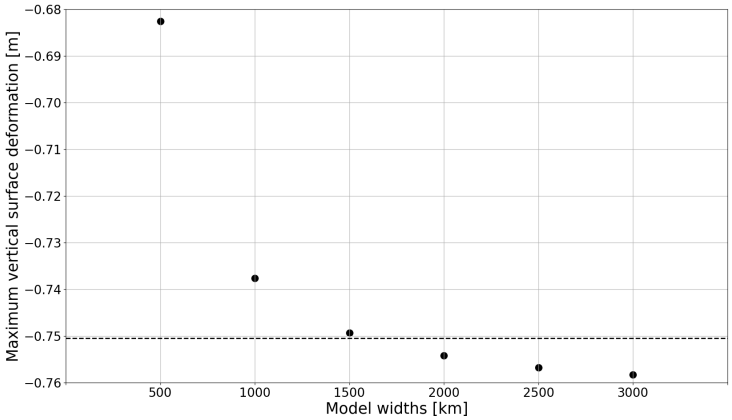

Figure I.A.1: Maximum vertical surface deformation for models with different model widths (500-3,000 km) at 200 years in ASPECT (dots), and TABOO (dashed line).

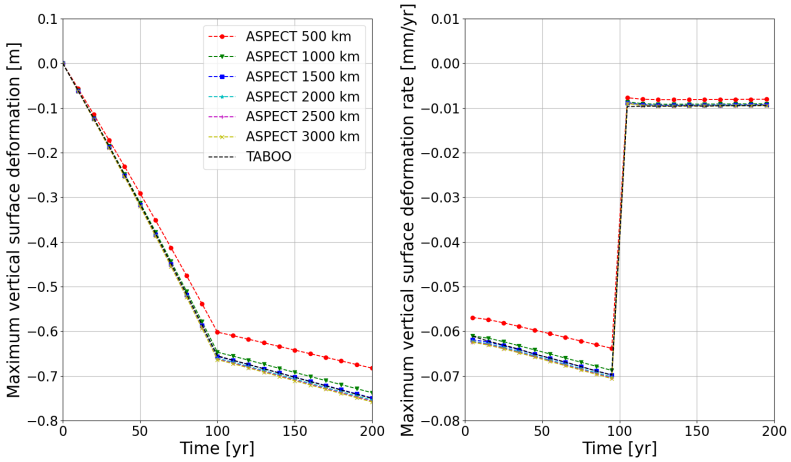

Figure I.A.2: Maximum vertical surface deformation (left) and rate (right) for a model horizontal dimension of 500 km (red dots), 1,000 km (green triangles), 1,500 km (blue squares), 2,000 km (cyan stars), 2,500 km (magenta pluses), 3,000 km (yellow crosses), and TABOO (dashed black line).

Appendix B: Sphericity and Self-Gravitation

We show the effect of the box model's non-spherical and non-self-gravitational features by applying wider surface loads. For regional GIA modeling, one needs to model not only the local ice load, but also the surrounding ice masses, because solid earth deformation sensitivity stretches to distances away from the ice load. Amelung and Wolf (1994) showed the applicability of box models for regional studies. As ASPECT is non-spherical and non-self-gravitating, we test the effect of a wider surface load. Here, we increase the ice disc radius to 500 km and increase the model horizontal dimensions to 10,000 km (see Appendix A) for the effect of lateral boundaries).

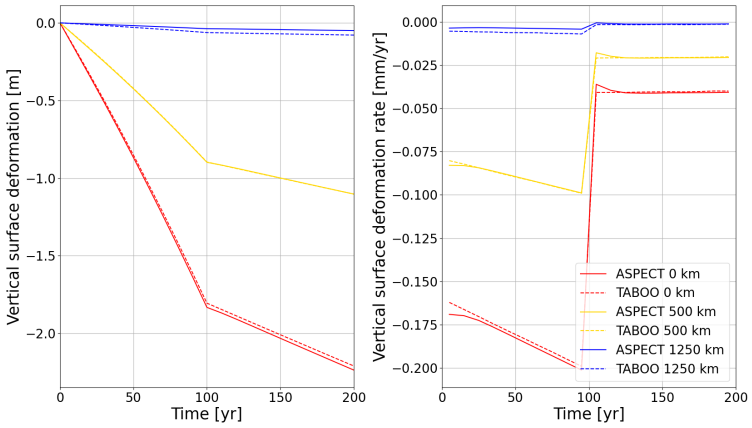

Figure I.B.1: Maximum vertical surface deformation (left) and rate (right) for a load with 500 km radius as function of time for ASPECT (solid line), and TABOO (dashed line), at 0 km (red), 500 km (yellow), and 1,250 km (blue) distance from the load center.

Table I.B.1: Average absolute and percentage difference of vertical surface deformation and deformation rate at different distances from the load center between ASPECT and TABOO for the short timescale simulation for a load radius of 500 km.

	Deformation		Deformation rate	
Distance from load center [km]	Avg. absolute difference [m]	Avg. percentage difference [%]	Avg. absolute difference [mm/yr]	Avg. percentage difference [%]
0	0.020	1.70	$1.90 \cdot 10^{-3}$	2.11
500	0.002	0.58	$5.31 \cdot 10^{-4}$	1.67
1250	0.019	38.29	$1.44 \cdot 10^{-3}$	32.27

From a first view, the deformation and deformation rates look similar between ASPECT and TABOO for the 500 km load radius (Figure I.B.1). At a distance

of 2.5 times the ice disc radius (i.e. 1,250 km) we see a similar difference between ASPECT and TABOO as for the 100 km radius ice disc at 250 km (Figs. I.3c and I.B.1, blue lines). At the ice disc boundary there is a better agreement for the 500 km disc radius (Figs. I.3c and I.B.1, yellow lines), and underneath the center of the ice load the agreement slightly worsens for the 500 km radius ice disc (Figs. I.3c and I.B.1, red lines). We see average percentage differences for the deformation and deformation rate well within 2.2% between the models underneath the load center and at 500 km distance (i.e. at the load boundary) (Table I.B.1). Larger differences occur at 1,250 km distance (2.5 times the load radius) (Figure I.B.1, blue lines), for example, we observe a ∼30% average percentage difference in deformation rate between ASPECT and TABOO. However, the absolute rate is already remarkably small at this distance, with 0.001 mm/year at 200 years, which is 2.4% of the rate underneath the load center (Figure I.B.1, right). Whereas the rate for the 100 km load radius was 0.0016 mm/yr at 250 km distance (also 2.5 times the load radius), which is 16% of the rate underneath the load center (Figure I.3). On these larger scales, sphericity and self-gravitation seem to play a smaller role close to the ice load, and a larger but still minor role in the surface deformation and deformation rates further away from the ice load. This study agrees with findings from Amelung and Wolf (1994), Wu and Johnston (1998), and Ivins and James (1999). We show that the solid earth deformation model in ASPECT is suitable for regional GIA modeling.

Appendix C: Model Density

In order to use ASPECT's adaptive mesh refinement capabilities in combination with a free surface, we need to apply a constant density throughout the domain. With a laterally varying mesh, the vertically varying density is not equally represented laterally, and free surface instabilities arise. Here, we show the effect of using a constant density as opposed to a density profile for ASPECT and TABOO.

We set the constant density to the volume-averaged mantle density of the earth model density profile, 4,491.76 kg/m^3. We run two more simulations with a constant density of 4,400 kg/m^3 and 4,600 kg/m^3 to show the effect of average density on the free surface deformation. In TABOO, we change the density of the pre-set earth model in the source code. However, for the computation of the surface deformation based on load deformation coefficients (Spada, 2003), the average earth density is required. In order to keep the reference average earth density equal among runs with different constant density, we tune the core density accordingly in the source code.

The average percentage difference between using a density profile or a constant density is within 1.4% for the deformation and deformation rate at 0 km for ASPECT and within 2.0% for TABOO (Table I.C.1). The average percentage

Table I.C.1: Average percentage difference of vertical surface deformation and deformation rate at different distances from the load center between the density profile and constant density of 4,491.76 kg/m^3 for ASPECT and TABOO for the short timescale simulation.

	ASPECT $\rho_{profile}$ - $\rho_{constant}$		TABOO $\rho_{profile}$ - $\rho_{constant}$	
Distance from load center [km]	Deformation avg. percentage difference [%]	Deformation rate avg. percentage difference [%]	Deformation avg. percentage difference [%]	Deformation rate avg. percentage difference [%]
0	0.85	1.40	1.49	1.95
100	0.98	1.59	1.82	2.32
250	2.02	2.68	3.69	5.61

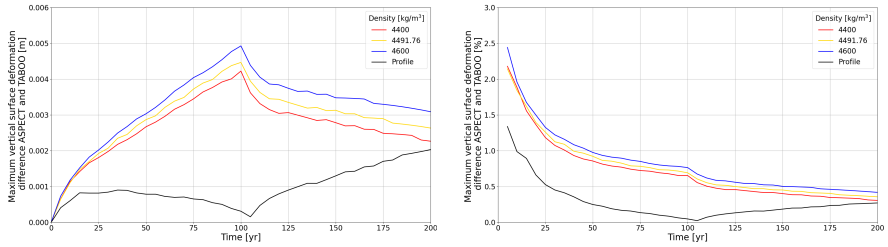

Figure I.C.1: (a) Maximum vertical surface deformation absolute difference between ASPECT and TABOO and (b) percentage difference, as function of time for a constant density of 4,400 kg/m^3 (red), 4,491.76 kg/m^3 (yellow), 4,600 kg/m^3 (blue), and the density profile as in the benchmark test (black).

difference is within 5.7% for both ASPECT and TABOO for distances from the load center of 0, 100, and 250 km (Table I.C.1). The absolute difference in maximum vertical surface deformation between ASPECT and TABOO is slightly larger for the constant density cases (<0.005 m after 100 years, or <1% percentage difference) than for the density profile (0.002 m after 200 years, or <0.5% percentage difference) (Figure I.C.1). Furthermore, we show that constant density variations give very similar surface deformation results compared to each other. Thus, the density value has a small effect on the surface deformation results. This test gives confidence in the performance of the models for either using a constant density or a density profile. Since density is not an important factor on the surface deformation results, we can confidently use the AMR in ASPECT.

Acknowledgments

The authors thank two anonymous reviewers and Volker Klemann for their reviews, which helped us to improve the manuscript, Giorgio Spada for making TABOO open-source, Fiona Clerc and Daniel Douglas for their work on free surface deformation in ASPECT on which this study could build, and Björn Heyn

for his work on making ASPECT and `deal.II` available on the HPC clusters in Norway. The authors also thank the Glacial Isostatic Adjustment Training School 2019 sponsored by SCAR-SERCE and NSF-POLENET. This work was supported by the Norwegian Research Council projects 223272 (Centre of Excellence) and 288449 (MAGPIE Project). Computations were made possible by the Norwegian Research Infrastructure Services (NRIS) via allocations NN9283K/NS9029K. We thank the Computational Infrastructure for Geodynamics (geodynamics.org), which is funded by the National Science Foundation under award EAR-0949446 and EAR-1550901, for supporting the development of ASPECT. R. Steffen is supported by a project grant from Rymdstyrelsen (Swedish National Space Agency; grant number 2018-00140). T. Heister and J. Zhang were partially supported by the National Science Foundation (NSF) award DMS-2028346, OAC-2015848, EAR-1925575, and by the Computational Infrastructure in Geodynamics initiative (CIG), through the NSF under award EAR-0949446 and EAR-1550901 and The University of California, Davis. This research is part of the Frontera computing project at the Texas Advanced Computing Center. Frontera is made possible by National Science Foundation award OAC-1818253.

Open Research: Data Availability Statement

The open-source code ASPECT (v2.4.0) (Kronbichler et al., 2012; Heister et al., 2017; Bangerth et al., 2022a, 2022b; Rose et al., 2017; Clevenger & Heister, 2021) is available for download on GitHub (https://github.com/geodynamics/aspect/releases/tag/v2.4.0) or Zenodo (https://doi.org/10.5281/zenodo.6903424), along with the parameter and log files for the simulations in this study (https://doi.org/10.5281/zenodo.7334568). The open-source code TABOO (v1.1) is available for download on GitHub (https://github.com/danielemelini/TABOO). Abaqus 2019 is commercial licensed software and can be purchased through https://www.3ds.com/products-services/simulia/products/Abaqus/. In Figs. 3, 4, and 7 the scientific cyclic color map romaO is used (Crameri, 2018).

References

A, G., Wahr, J., & Zhong, S. (2013). Computations of the viscoelastic response of a 3-D compressible Earth to surface loading: an application to Glacial Isostatic Adjustment in Antarctica and Canada. *Geophysical Journal International*, *192*(2), 557-572. doi: 10.1093/gji/ggs030

Adhikari, S., Milne, G. A., Caron, L., Khan, S. A., Kjeldsen, K. K., Nilsson, J., ... Ivins, E. R. (2021). Decadal to Centennial Timescale Mantle Viscosity Inferred From Modern Crustal Uplift Rates in Greenland. *Geophysical Research Letters*, *48*. doi: 10.1029/2021GL094040

Amelung, W., & Wolf, D. (1994). Viscoelastic perturbations of the earth: significance of the incremental gravitational force in models of glacial isostasy. *Geophysical Journal International*, *117*, 864-879. doi: 10.1111/j.1365-246X.1994.tb02476.x

Arndt, D., Bangerth, W., Feder, M., Fehling, M., Gassmöller, R., Heister, T., ... Wells, D. (2022). The `deal.II` library, version 9.4. *Journal of Numerical Mathematics*. Retrieved from https://dealii.org/deal94-preprint.pdf doi: 10.1515/jnma-2022-0054

Austermann, J., Mitrovica, J. X., Huybers, P., & Rovere, A. (2017). Detection of a dynamic topography signal in last interglacial sea-level records. *Science Advances*, *3*(7), e1700457. doi: 10.1126/sciadv.1700457

Bagge, M., Klemann, V., Steinberger, B., Latinović, M., & Thomas, M. (2021). Glacial-Isostatic Adjustment Models Using Geodynamically Constrained 3D Earth Structures. *Geochemistry, Geophysics, Geosystems*, *22*(11), e2021GC009853. doi: 10.1029/2021GC009853

Bangerth, W., Dannberg, J., Fraters, M., Gassmöller, R., Glerum, A., Heister, T., ... Naliboff, J. (2022a). *ASPECT v2.4.0.* Zenodo. doi: 10.5281/zenodo.6903424

Bangerth, W., Dannberg, J., Fraters, M., Gassmöller, R., Glerum, A., Heister, T., ... Naliboff, J. (2022b). *ASPECT: Advanced Solver for Problems in Earth's ConvecTion, User Manual.* doi: 10.6084/m9.figshare.4865333.v9

Barletta, V., Bevis, M., Smith, B., Wilson, T., Brown, A., Bordoni, A., ... Wiens, D. (2018). Observed rapid bedrock uplift in amundsen sea embayment promotes ice-sheet stability. *Science*, *360*, 1335–1339. doi: 10.1126/science.aao1447

Bevis, M., Wahr, J., Khan, S. A., Madsen, F. B., Brown, A., Willis, M., ... Francis, O. (2012). Bedrock displacements in Greenland manifest ice mass variations, climate cycles and climate change. *Proceedings of the National Academy of Sciences*, *109*(30), 11944-11948. doi: 10.1073/pnas.1204664109

Blank, B., Barletta, V., Hu, H., Pappa, F., & van der Wal, W. (2021). Effect of Lateral and Stress-Dependent Viscosity Variations on GIA Induced Uplift Rates in the Amundsen Sea Embayment. *Geochemistry, Geophysics, Geosystems*, *22*(9), e2021GC009807. doi: 10.1029/2021GC009807

Bradley, S. L., Hindmarsh, R. C. A., Whitehouse, P. L., Bentley, M. J., & King, M. A. (2015). Low post-glacial rebound rates in the Weddell Sea due to Late Holocene ice-sheet readvance. *Earth and Planetary Science Letters*, *413*, 79-89. doi: 10.1016/j.epsl.2014.12.039

Celli, N. L., Lebedev, S., Schaeffer, A. J., & Gaina, C. (2021). The tilted iceland plume and its effect on the north atlantic evolution and magmatism. *Earth and Planetary Science Letters*, *569*, 117048. doi: 10.1016/j.epsl.2021.117048

Clevenger, T. C., & Heister, T. (2021). Comparison between algebraic and matrix-free geometric multigrid for a Stokes problem on an adaptive mesh with variable viscosity. *Numerical Linear Algebra with Applications*, *28*(5), e2375. doi: 10.1002/nla.2375

Clevenger, T. C., Heister, T., Kanschat, G., & Kronbichler, M. (2020). A Flexible, Parallel, Adaptive Geometric Multigrid Method for FEM. *ACM Transactions on Mathematical Software*, *47*(1), 1-27. doi: 10.1145/3425193

Crameri, F. (2018). *Scientific colour maps.* Zenodo. doi: 10.5281/zenodo.1243862

Dannberg, J., & Gassmöller, R. (2018). Chemical trends in ocean islands explained by plume–slab interaction. *Proceedings of the National Academy of Sciences*, *115*(17), 4351-4356. doi: 10.1073/pnas.1714125115

Dassault Systèmes. (2019). *Abaqus 2019.* Retrieved from https://www.3ds.com/products-services/simulia/products/abaqus/

Glerum, A., Thieulot, C., Fraters, M., Blom, C., & Spakman, W. (2018). Nonlinear viscoplasticity in ASPECT: benchmarking and applications to subduction. *Solid Earth*, *9*(2), 267-294. doi: 10.5194/se-9-267-2018

Han, D., & Wahr, J. (1997). An analysis of anisotropic mantle viscosity and its possible effects on post-glacial rebound. *Physics of the Earth and Planetary Interiors*, *102*(1), 33-50. doi: 10.1016/S0031-9201(96)03268-2

Heister, T., Dannberg, J., Gassmöller, R., & Bangerth, W. (2017). High Accuracy Mantle Convection Simulation through Modern Numerical Methods – II: Realistic Models and Problems. *Geophysical Journal International*, *210*, 833-851. doi: 10.1093/gji/ggx195

Helm, V., Humbert, A., & Miller, H. (2014). Elevation and elevation change of Greenland and Antarctica derived from CryoSat-2. *The Cryosphere*, *8*, 1539-1559. doi: 10.5194/tc-8-1539-2014

Ivins, E. R., & James, T. S. (1999). Simple models for late Holocene and present-day Patagonian glacier fluctuations and predictions of a geodetically detectable isostatic response. *Geophysical Journal International*, *138*, 601-624. doi: 10.1046/j.1365-246x.1999.00899.x

Ivins, E. R., James, T. S., Wahr, J., O. Schrama, E. J., Landerer, F. W., & Simon, K. M. (2013). Antarctic contribution to sea level rise observed by GRACE with improved GIA correction. *Journal of Geophysical Research: Solid Earth*, *118*(6), 3126-3141. doi: 10.1002/jgrb.50208

Kaufmann, G., Wu, P., & Wolf, D. (1997). Some effects of lateral heterogeneities in the upper mantle on postglacial land uplift close to continental margins. *Geophysical Journal International*, *128*(1), 175-187. doi: j.1365-246X.1997.tb04078.x

Khan, S. A., Sasgen, I., Bevis, M., van Dam, T., Bamber, J. L., Wahr, J., ... Munneke, P. K. (2016). Geodetic measurements reveal similarities between post–Last Glacial Maximum and present-day mass loss from the Greenland ice sheet. *Science Advances*, *2*(9). doi: 10.1126/sciadv.1600931

Kronbichler, M., Heister, T., & Bangerth, W. (2012). High Accuracy Mantle Convection Simulation through Modern Numerical Methods. *Geophysical Journal International*, *191*, 12-29. doi: 10.1111/j.1365-246x.2012.05609.x

Latychev, K., Mitrovica, J. X., Tromp, J., Tamisiea, M. E., Komatitsch, D., & Christara, C. C. (2005). Glacial isostatic adjustment on 3-D Earth models: a finite-volume formulation. *Geophysical Journal International*, *161*(2), 421-444. doi: 10.1111/j.1365-246X.2005.02536.x

Lau, H. C. P., Austermann, J., Holtzman, B. K., Havlin, C., Lloyd, A. J., Book, C., & Hopper, E. (2021). Frequency Dependent Mantle Viscoelasticity via

the Complex Viscosity: Cases From Antarctica. *Journal of Geophysical Research: Solid Earth*, *126*(e2021JB022622). doi: 10.1029/2021JB022622

Li, T., Wu, P., Wang, H. S., Steffen, H., Khan, N. S., Engelhart, S. E., ... Horton, B. P. (2020). Uncertainties of Glacial Isostatic Adjustment model predictions in North America associated with 3D structure. *Geophysical Research Letters*, *47*, e2020GL087944. doi: 10.1029/2020GL087944

Lloyd, A. J., Wiens, D. A., Zhu, H., Tromp, J., Nyblade, A. A., Aster, R. C., ... O'Donnell, J. P. (2020). Seismic Structure of the Antarctic Upper Mantle Imaged with Adjoint Tomography. *Journal of Geophysical Research: Solid Earth*, *125*. doi: 10.1029/2019JB017823

Marsman, C. P., van der Wal, W., Riva, R. E. M., & Freymueller, J. T. (2021). The Impact of a 3-D Earth Structure on Glacial Isostatic Adjustment in Southeast Alaska Following the Little Ice Age. *Journal of Geophysical Research: Solid Earth*, *126*, e2021JB022312. doi: 10.1029/2021JB022312

Martinec, Z., Klemann, V., van der Wal, W., Riva, R. E. M., Spada, G., Sun, Y., ... James, T. S. (2018). A benchmark study of numerical implementations of the sea level equation in gia modelling. *Geophysical Journal International*, *215*(1), 389-414. doi: 10.1093/gji/ggy280

Martos, Y. M., Jordan, T. A., Catalán, M., Jordan, T. M., Bamber, J. L., & Vaughan, D. G. (2018). Geothermal Heat Flux Reveals the Iceland Hotspot Track Underneath Greenland. *Geophysical Research Letters*, *45*, 8214-8222. doi: 10.1029/2018GL078289

Milne, G. A., Latychev, K., Schaeffer, A., Crowley, J. W., Lecavalier, B. S., & Audette, A. (2018). The influence of lateral Earth structure on glacial isostatic adjustment in Greenland. *Geophysical Journal International*, *214*, 1252–1266. doi: 10.1093/gji/ggy189

Moresi, L., Dufour, F., & Mühlhaus, H.-B. (2003). A Lagrangian integration point finite element method for large deformation modeling of viscoelastic geomaterials. *Journal of Computational Physics*, *184*, 476-497. doi: 10.1016/S0021-9991(02)00031-1

Nield, G. A., Barletta, V. R., A. Bordoni and, M. A. K., Whitehouse, P. L., Clarke, P. J., Domack, E., ... Berthier, E. (2014). Rapid bedrock uplift in the Antarctic Peninsula explained by viscoelastic response to recent ice unloading. *Earth and Planetary Science Letters*, *397*, 32-41. doi: 10.1016/j.epsl.2014.04.019

Pappa, F., Ebbing, J., Ferraccioli, F., & van der Wal, W. (2019). Modeling Satellite Gravity Gradient Data to Derive Density, Temperature and Viscosity Structure of the Antarctic Lithosphere. *Journal of Geophysical Research: Solid Earth*, *124*(11), 12053-12076. doi: 10.1029/2019JB017997

Peltier, W. R. (1974). The impulse response of a maxwell earth. *Reviews of Geophysics*, *12*(4), 649-669. doi: 10.1029/RG012i004p00649

Peltier, W. R. (1976). Glacial-isostatic adjustment - II. The inverse problem. *Geophysical Journal of the Royal Astronomical Society*, *46*, 669-706. doi: 10.1111/j.1365-246X.1976.tb01253.x

Powell, E., Gomez, N., Hay, C., Latychev, K., & Mitrovica, J. X. (2020). Viscous Effects in the Solid Earth Response to Modern Antarctic Ice Mass Flux:

Implications for Geodetic Studies of WAIS Stability in a Warming World. *Journal of Climate*, *33*(2), 443-459. doi: 10.1175/JCLI-D-19-0479.1

Root, B. C., Sebera, J., Szwillus, W., Thieulot, C., Martinec, Z., & Fullea, J. (2022). Benchmark forward gravity schemes: the gravity field of a realistic lithosphere model WINTERC-G. *Solid Earth*, *13*(5), 849-873. doi: 10.5194/se-13-849-2022

Rose, I., Buffett, B., & Heister, T. (2017). Stability and accuracy of free surface time integration in viscous flows. *Physics of the Earth and Planetary Interiors*, *262*, 90-100. doi: 10.1016/j.pepi.2016.11.007

Roy, K., & Peltier, W. (2018). Relative sea level in the Western Mediterranean basin: A regional test of the ICE-7G_NA (VM7) model and a constraint on late Holocene Antarctic deglaciation. *Quaternary Science Reviews*, *183*, 76-87. doi: 10.1016/j.quascirev.2017.12.021

Sabadini, D. A. Y., R., & Portney, M. (1986). The effects of upper-mantle lateral heterogeneities on postglacial rebound. *Geophysical Research Letters*, *13*(4), 337-340. doi: 10.1029/GL013i004p00337

Samrat, N. H., King, M. A., Watson, C., Hay, A., Barletta, V. R., & Bordoni, A. (2021). Upper Mantle Viscosity Underneath Northern Marguerite Bay, Antarctic Peninsula Constrained by Bedrock Uplift and Ice Mass Variability. *Geophysical Research Letters*, *48*(24), e2021GL097065. doi: 10.1029/2021GL097065

Samrat, N. H., King, M. A., Watson, C., Hooper, A., Chen, X., Barletta, V. R., & Bordoni, A. (2020). Reduced ice mass loss and three-dimensional viscoelastic deformation in northern Antarctic Peninsula inferred from GPS. *Geophysical Journal International*, *222*, 1013-1022. doi: 10.1093/gji/ggaa229

Sandiford, D., Brune, S., Glerum, A., Naliboff, J. B., & Whittaker, J. M. (2021). Kinematics of footwall exhumation at oceanic detachment faults: Solid-block rotation and apparent unbending. *Geochemistry, Geophysics, Geosystems*, *22*(4), e2021GC009681. doi: 10.1029/2021GC009681

Scheinert, M., Engels, O., Schrama, E. J. O., van der Wal, W., & Horwath, M. (2021). Geodetic observations for constraining mantle processes in Antarctica. *Geological Society, London, Memoirs*, *56*(1), M56-2021-22. doi: 10.1144/M56-2021-22

Schotman, H. H. A., Wu, P., & Vermeersen, L. L. A. (2008). Regional perturbations in a global background model of glacial isostasy. *Physics of the Earth and Planetary Interiors*, *171*(1), 323-335. doi: 10.1016/j.pepi.2008.02.010

Simpson, M. J. R., Wake, L., Milne, G. A., & Huybrechts, P. (2011). The influence of decadal- to millennial-scale ice mass changes on present-day vertical land motion in Greenland: Implications for the interpretation of GPS observations. *Journal of Geophysical Research: Solid Earth*, *116*. doi: 10.1029/2010jb007776

Spada, G. (2003). *The theory behind TABOO.* Retrieved 18 November 2021, from https://github.com/danielemelini/TABOO/blob/master/DOC/TABOO-theory.pdf

Spada, G., Antonioli, A., Boschi, L., Brandi, V., Cianetti, S., Galvani, G.,

... Stocchi, P. (2003). *TABOO User Guide.* Retrieved 18 November 2021, from https://github.com/danielemelini/TABOO/blob/master/DOC/TABOO_User_Guide.pdf

Spada, G., Barletta, V. R., Klemann, V., Riva, R. E. M., Martinec, Z., P. Gasperini, B., ... King, M. A. (2011). A benchmark study for glacial isostatic adjustment codes. *Geophysical Journal International*, *185*(1), 106-132. doi: 10.1111/j.1365-246X.2011.04952.x

Steffen, H., Kaufmann, G., & Wu, P. (2006). Three-dimensional finite-element modeling of the glacial isostatic adjustment in Fennoscandia. *Earth and Planetary Science Letters*, *250*(1), 358-375. doi: 10.1016/j.epsl.2006.08.003

Steffen, R., Audet, P., & Lund, B. (2018). Weakened Lithosphere Beneath Greenland Inferred From Effective Elastic Thickness: A Hot Spot Effect? *Geophysical Research Letters*, *45*, 4733-4742. doi: 10.1029/2017GL076885

The IMBIE Team. (2018). Mass balance of the Antarctic Ice Sheet from 1992 to 2017. *Nature*, *558*, 219-222. doi: 10.1038/s41586-018-0179-y

The IMBIE Team. (2020). Mass balance of the Greenland Ice Sheet from 1992 to 2018. *Nature*, *579*, 233-239. doi: 10.1038/s41586-019-1855-2

van Dam, T., O. Francis, a. d. J., Khan, S. A., Bevis, M., & den Broeke, M. R. (2017). Using GPS and absolute gravity observations to separate the effects of present-day and Pleistocene ice-mass changes in South East Greenland. *Earth and Planetary Science Letters*, *459*, 127-135. doi: 10.1016/j.epsl.2016.11.014

van der Wal, W., Barnhoorn, A., Stocchi, P., Gradmann, S., Wu, P., Drury, M., & Vermeersen, B. (2013). Glacial isostatic adjustment model with composite 3-D Earth rheology for Fennoscandia. *Geophysical Journal International*, *194*(1), 61-77. doi: 10.1093/gji/ggt099

van der Wal, W., Whitehouse, P. L., & Schrama, E. J. O. (2015). Effect of GIA models with 3D composite mantle viscosity on GRACE mass balance estimates for Antarctica. *Earth and Planetary Science Letters*, *414*, 134-143. doi: 10.1016/j.epsl.2015.01.001

Vermeersen, L. L. A., & Sabadini, R. (1997). A new class of stratified viscoelastic models by analytical techniques. *Geophysical Journal International*, *129*, 531-570. doi: 10.1111/j.1365-246X.1997.tb04492.x

Wan, J. X. W., Gomez, N., Latychev, K., & Han, H. K. (2022). Resolving glacial isostatic adjustment (GIA) in response to modern and future ice loss at marine grounding lines in West Antarctica. *The Cryosphere*, *16*(6), 2203–2223. doi: 10.5194/tc-16-2203-2022

Weerdesteijn, M. F. M., Conrad, C. P., & Naliboff, J. B. (2022). Solid Earth Uplift Due To Contemporary Ice Melt Above Low-Viscosity Regions of the Upper Mantle. *Geophysical Research Letters*, *49*(17), e2022GL099731. doi: 10.1029/2022GL099731

Whitehouse, P. L. (2018). Glacial isostatic adjustment modelling: historical perspectives, recent advances and future directions. *Earth Surface Dynamics*, *6*, 401-429. doi: 10.5194/esurf-6-401-2018

Whitehouse, P. L., Bentley, M. J., Milne, G. A., King, M. A., & Thomas, I. D. (2012). A new glacial isostatic adjustment model for antarctica: calibrated and tested using observations of relative sea-level change and present-day uplift rates. *Geophysical Journal International*, *190*(3), 1464-1482. doi: 10.1111/j.1365-246X.2012.05557.x

Wolstencroft, M., King, M. A., Whitehouse, P. L., Bentley, M. J., Nield, G. A., King, E. C., ... Gunter, B. C. (2015). Uplift rates from a new high-density GPS network in Palmer Land indicate significant late Holocene ice loss in the southwestern Weddell Sea. *Geophysical Journal International*, *203*, 737-754. doi: 10.1093/gji/ggv327

Wu, P. (2004). Using commercial finite element packages for the study of earth deformations, sea levels and the state of stress. *Geophysical Journal International*, *158*, 401-408. doi: 10.1111/j.1365-246X.2004.02338.x

Wu, P., & Johnston, P. J. (1998). Validity of using flat-earth finite element models in the study of postglacial rebound. In P. Wu (Ed.), *Dynamics of the ice age earth: A modern perspective* (p. 191-202). Trans Tech Publications Ltd.

Wu, P., Ni, Z., & Kaufmann, G. (1998). Postglacial Rebound with Lateral Heterogeneities : from 2D to 3D modeling. In P. Wu (Ed.), *Dynamics of the ice age earth: A modern perspective* (p. 557-582). Trans Tech Publications Ltd.

Wu, P., & Peltier, W. R. (1982). Viscous gravitational relaxation. *Geophysical Journal International*, *70*(2), 435-485. doi: 10.1111/j.1365-246X.1982.tb04976.x

Wu, P., Steffen, R., Steffen, H., & Lund, B. (2021). lacial isostatic adjustment models for earthquake triggering. In H. Steffen, O. Olesen, & R. Sutinen (Eds.), *Glacially-triggered faulting* (p. 383-401). Cambridge University Press.

Yousefi, M., Milne, G. A., & Latychev, K. (2021). Glacial isostatic adjustment of the Pacific Coast of North America: the influence of lateral Earth structure. *Geophysical Journal International*, *226*, 91-113. doi: 10.1093/gji/ggab053

Zhao, C., A.King, M., Watson, C. S., Barletta, V. R., Bordoni, A., Dell, M., & Whitehouse, P. L. (2017). Rapid ice unloading in the Fleming Glacier region, southern Antarctic Peninsula and its effect on bedrock uplift rates. *Earth and Planetary Science Letters*, *473*, 164-176. doi: 10.1016/j.epsl.2017.06.002

Zhong, S., Kang, K., A, G., & Qin, C. (2022). CitcomSVE: A Three-dimensional Finite Element Software Package for Modeling Planetary Mantle's Viscoelastic Deformation in Response to Surface and Tidal Loads. *Geochemistry, Geophysics, Geosystems*, *23*, e2022GC010359. doi: 10.1029/2022GC010359

Zwinger, T., Nield, G. A., Ruokolainen, J., & King, M. A. (2020). A new open-source viscoelastic solid earth deformation module implemented in Elmer (v8.4). *Geoscientific Model Development*, *13*(3), 1155-1164. doi: 10.5194/gmd-13-1155-2020

Paper II

Solid Earth Uplift Due To Contemporary Ice Melt Above Low-Viscosity Regions of the Upper Mantle

Maaike F. M. Weerdesteijn[1], C. P. Conrad[1], and John B. Naliboff[2]

[1]Centre for Earth Evolution and Dynamics, University of Oslo, Oslo, Norway
[2]Department of Earth and Environmental Science, New Mexico Institute of Mining and Technology, Socorro, United States

Published in *Geophysical Research Letters*, September 2022, volume 49, e2022GL099731, 10.1029/2022GL099731

II

Key Points:

- Contemporary ice melt above low-viscosity mantle produces uplift on decadal timescales, but viscosity heterogeneity affects uplift rates
- Our viscoelastic deformation models with varying viscosity show that a low-viscosity region's horizontal extent greatly affects uplift rates
- The viscous response to recent ice melting, usually not considered, may be a dominant contributor to uplift above low-viscosity regions

Abstract

Glacial isostatic adjustment explains topographic change in formerly and currently glaciated regions, but the role of small (∼100s km) regions of unusually low-viscosity mantle is poorly understood. We developed viscoelastic models with low-viscosity regions in the upper mantle, and measured the effect of these regions on solid earth uplift resulting from contemporary surface ice melt. We found viscous uplift occurring on decadal timescales above the low-viscosity region, at rates comparable to or larger than those from elastic uplift or the viscous response to ice age melting. We find that uplift rates are sensitive to the location, dimensions, and viscosity of the low-viscosity region, and that the largest

uncertainty in uplift rates likely comes from the low-viscosity region's horizontal extent. Rapid viscous ground uplift can impact ice dynamics if the low-viscosity region is located close to an ice sheet margin, as for Antarctica and Greenland.

Plain Language Summary

Ice melting in Antarctica and Greenland causes ground motion as Earth's interior rocks deform in response to ice mass changes at the surface. The timescale on which the deformation takes place is dependent on the capacity of the interior rocks to deform, controlled by viscosity. It is commonly thought that high viscosity in the mantle causes deformation to take place on timescales of thousands of years. However, low-viscosity regions speed up the deformation considerably, taking decades instead. We developed numerical models that can handle large spatial variations in viscosity. We found that contemporary ice melt above a low-viscosity region can cause upward deformation at rates faster than from the past (ice age) melting, and large enough to be an important consideration for understanding future ice dynamics in potential rapid melting scenarios.

II.1 Introduction

Glacial isostatic adjustment (GIA) is the ongoing response of the solid earth and the geoid to changes in ice and ocean loading, and produces solid earth ground motion that can be measured using GNSS (Global Navigation Satellite Systems). Near areas of past or current ice cover change, it is commonly thought GIA displacements result from a combination of (a) a viscous response to historic ice load changes (i.e., ice age melting), and (b) an elastic response to contemporary ice load changes. Typically, the viscous response occurs over several thousand years, but recent studies have shown regions undergoing rapid viscous uplift on decadal or centennial timescales in response to contemporary ice melt in West Antarctica (Nield et al., 2014; Barletta et al., 2018) and southeast Greenland (Khan et al., 2016). Rapid uplift in these regions is commonly linked to low-viscosities in the upper mantle that accelerate the viscous response to recent melting. In this case, contemporary ice melt generates not only an instantaneous elastic response, but also a viscous response on short timescales. This rapid viscous response is mixed with the other deformation components of GIA (elastic and long-term viscous) that are measured using GNSS, which makes it difficult to distinguish between solid earth deformation due to historical and contemporary ice load changes (Whitehouse, 2018).

There are indications that low-viscosity regions of the upper mantle are present beneath both Antarctica and Greenland. Here, we define low-viscosity regions as regions where the viscosity is considerably lower than surrounding mantle material, with a value that can result in deformation on decadal or centennial timescales ($5{\cdot}10^{19}$ Pa s or lower), as opposed to thousands of years. Seismic

studies in Antarctica show slower velocity anomalies in West compared to East Antarctica (Heeszel et al., 2016; Lloyd et al., 2020), consistent with a colder cratonic region in East Antarctica, and a warmer tectonically active region in West Antarctica, possibly with a mantle plume (Bredow et al., 2021). Lateral variations in mantle temperature, derived from seismic velocity anomalies, suggest lateral variations in mantle rheology (Ivins & Sammis, 1995; van der Wal et al., 2013). Upper mantle viscosities constrained by GNSS uplift and ice mass change show large variations across the Antarctic Peninsula and the Amundsen Sea Embayment, ranging from $<3{\cdot}10^{18}$ Pa s to $3{\cdot}10^{20}$ Pa s (Nield et al., 2014; Wolstencroft et al., 2015; Barletta et al., 2018).

The Kangerlussuaq glacier in southeast Greenland, one of Greenland's three largest ice mass losing glaciers (Brough et al., 2019), sits above a proposed upper mantle low-viscosity feature that is likely as a consequence of Greenland having passed over the Iceland plume more than 40 Myr ago (Steinberger et al., 2019). Proposed hot spot tracks align with magnetic, temperature, gravity, and seismic data (Rogozhina et al., 2016; Steffen et al., 2018; Martos et al., 2018; Mordret, 2018; Celli et al., 2021) and suggest a weakened lithosphere and upper mantle (Figure II.1a). Khan et al. (2016) suggested that GNSS uplift rates are consistent with a low-viscosity upper mantle of $1{\cdot}10^{19}$ Pa s beneath southeast Greenland, but their modeled uplift rates are based on a summation of deformation solutions from discretized ice loads above laterally homogeneous (1D) earth models. Milne et al. (2018) explored the influence of laterally heterogeneous (3D) earth structure on GIA in Greenland, but to this day no reconciliation is reached yet between modeled and observed uplift rates.

From seismic tomography models (Lloyd et al., 2020; Celli et al., 2021), we know there is a limited horizontal and vertical extent to potential low-viscosity regions beneath the lithosphere for Antarctica and Greenland (Figure II.1a). As yet, no study has systematically examined the sensitivity of uplift patterns to the dimensions, location, and viscosity of a low-viscosity region deforming as a result of contemporary ice melting, nor has any study characterized which parameter(s) contribute(s) dominantly to the uplift signal. The purpose of this study is to provide this systematic understanding in order to evaluate whether 3D modeling is important. To investigate this sensitivity, we compute viscoelastic earth deformation caused by contemporary ice melt above both a homogeneous earth (1D) and a heterogeneous earth (3D). By varying the dimensions, location, and viscosity of a low-viscosity region, we determine their effect on patterns and rates of uplift.

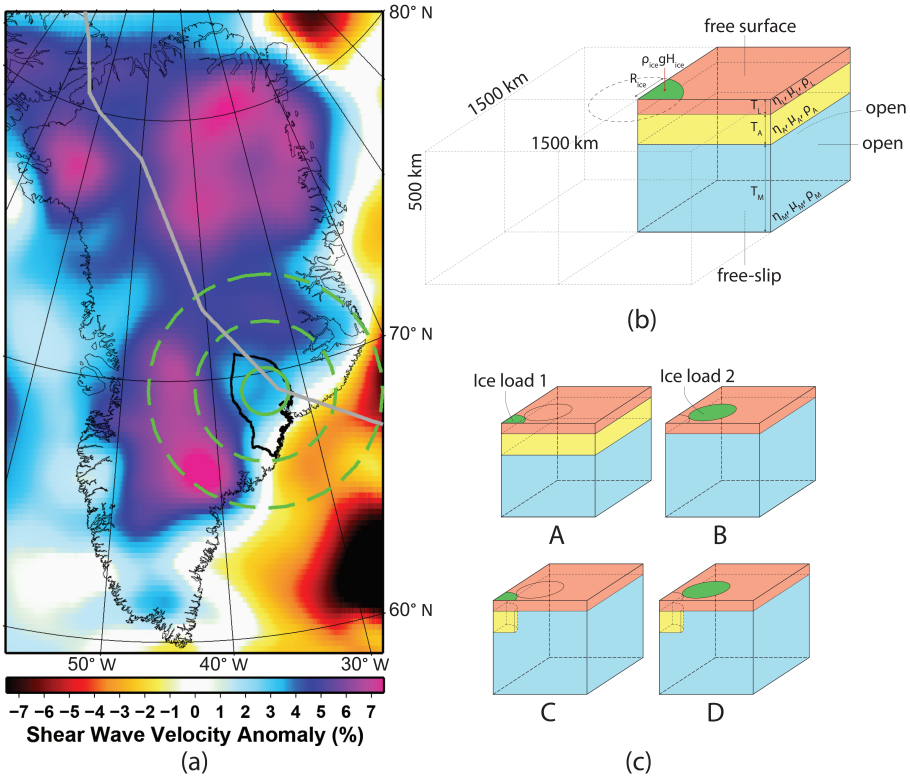

Figure II.1: (a) Seismic velocity anomalies at 150 km depth for Greenland (Celli et al., 2021). The gray line represents the potential plume track, drawn following Martos et al. (2018), the black bordered area is the drainage basin where the Kangerlussuaq glacier is located, and the inner green circle is the size of the modeled ice load and low-viscosity region (100 km radius), plus dashed green circles with radii of 300 and 500 km. (b) A quarter of the box model geometry (not to scale) with upper mantle (blue), low-viscosity asthenosphere (yellow), lithosphere (red), and active ice load (green), boundary conditions, layer properties, and boundary traction from ice loading. (c) Cases A and B showcase the 1D approach and cases C and D showcase the 3D approach for the two ice loads.

II.2 Modeling Deformation Near a Low-Viscosity Region: 1D Versus 3D Approach

We compare solid earth deformation due to contemporary ice melt for two modeling approaches, a 1D and 3D approach. The 1D approach consists of a summation of deformation solutions from discretized ice loads above layered viscosity structures. The 3D approach incorporates a low-viscosity (LV) region. In this study, we use an open-source, finite-element based, viscoelastic

earth deformation model in ASPECT v2.3.0 (Advanced Solver for Problems in Earth's ConvecTion) (Bangerth et al., 2021b, 2021a). For the GIA simulations, ASPECT solves the 3-D incompressible conservation equations assuming an infinite Prandtl number, the Boussinesq approximation, and isothermal flow, and assuming linear viscoelasticity (Moresi et al., 2003; Sandiford et al., 2021) (see Texts II.S1 to II.S3 in Supporting Information S1 for the model's mathematical description).

Model properties are shown in Figure II.1b and Table II.S1 in Supporting Information S1 (Dziewonski & Anderson, 1981). We use a box geometry with a horizontal dimension of 1,500 km in both directions and vertical dimension of 500 km, introducing a <0.05% error compared to a very wide (3,000 km) box, and a 0.5% error compared to a box of earth mantle depth (∼3,000 km). We use a linear Maxwell viscoelastic rheology. The top boundary is a free surface (Rose et al., 2017), allowing for vertical and lateral mesh deformation, and the bottom boundary is free-slip, allowing for tangential material flow only. The lateral boundaries are open, allowing for material in- and outflow, by applying boundary traction based on the lithostatic pressure profile. The ice loading consists of two cylindrical loads with a 100 km radius (approximate drainage basin size, Figure II.1a), 931 kg/m^3 ice density, and constant height in space. The ice height linearly decreases from 100 to 0 m over 100 years, that is, 1 m/yr ice melt, which is the order of magnitude for contemporary ice melt in Antarctica and Greenland (Helm et al., 2014; The IMBIE Team, 2020). Ice load 1 is located in the center of the domain, and ice load 2 is offset by $x = y = \sqrt{2{R_{ice}}^2}$, such that the ice loads touch, but do not overlap (Figure II.1c).

In the 1D approach, solid earth deformations are summed for a solution in which ice load 1 is above an LV layer (Figure II.1c.A), also referred to as LV asthenosphere, and a solution in which ice load 2 is above an earth structure without an LV layer (Figure II.1c.B). In the 3D approach, the same ice loads are placed on an earth model with an LV region (different from an LV layer as it has lateral boundaries), located in the upper mantle underneath ice load 1. In the 3D approach, the simulation is also split into two cases, one for each ice load (Figure II.1c.C and II.1c.D), to be able to distinguish between the deformations resulting from each ice load to compare to the solutions of the 1D approach (Figure II.2). Simulating the two ice loads separately or together results in essentially the same results, as expected for a linear system. The earth model for case A is given in Table II.S1 in Supporting Information S1. In case B, without an LV asthenosphere, the mantle extends to the bottom of the lithosphere. In cases C and D the LV region has the same material properties as the LV asthenosphere, and a radius equal to the ice load radius of 100 km (consistent with the potential low-viscosity feature size, Figure II.1a). The asthenosphere has a viscosity of $1{\cdot}10^{19}$ Pa s (background mantle viscosity is $5{\cdot}10^{20}$ Pa s), which is in the plausible range of LV features in West Antarctica and southeast Greenland (Nield et al., 2014; Khan et al., 2016). Using adaptive

mesh refinement (i.e., the mesh automatically adjusts itself with time), we have a resolution ranging between 3.625 and 50 km, with higher resolution within volumes of higher strain rate. The numerical time step size is 2.5 years.

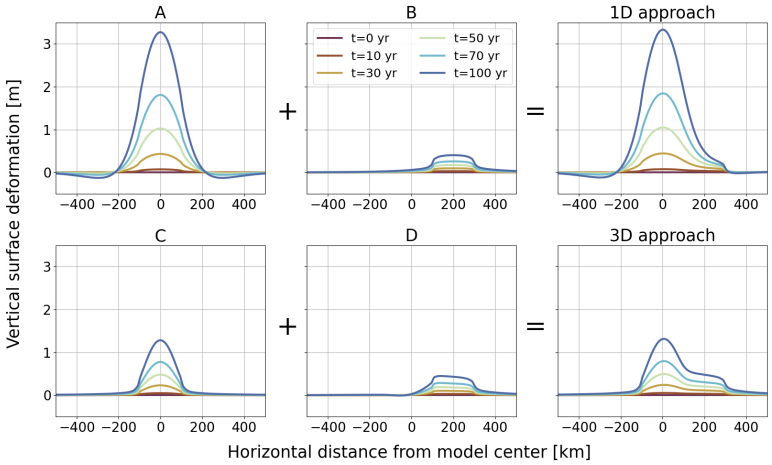

Figure II.2: Vertical surface deformation as a function of the horizontal distance from the model center at different time intervals (colors) for case A, case B, the total solution from the 1D approach (upper right), case C, case D, and the total solution from the 3D approach (lower right). See Figure II.1c for depictions of the different cases.

The vertical surface deformation due to ice load 1 above the LV asthenosphere (Figure II.2, case A) is ∼2.5 times larger than for the ice load above the LV region (Figure II.2, case C). This is because the ice load is sensitive not only to the viscosity structure directly underneath it, but also to the viscosities surrounding the load. Furthermore, case A shows subsidence in the periphery, about 300 km away from the ice load center. These areas of subsidence (or bulges in case of ice load increase) are a result of the LV layer that allows for channel flow (Cathles, 1975). The areas of subsidence are not present in the 3D solution as there is no LV channel present (Figure II.2, case C). The deformation due to ice load 2 in the 3D approach is skewed toward the LV region, and is slightly larger than for the 1D approach (Figure II.2, case D). The total deformation for the 1D and 3D approaches is very different in magnitude and spatial pattern (Figure II.2, right column). This emphasizes the importance of using 3D earth models for solid earth deformation studies from contemporary ice melt in the presence of an LV region, and not a summation of discretized ice loads above different 1D earth models (Khan et al., 2016; Hartmann et al., 2020).

II.3 Sensitivity of Deformation to Low-Viscosity Region Characteristics

Now that we have established that in the presence of an LV region the 3D approach provides a more accurate, and different, solution than the 1D approach, we use our 3D modeling tool to look into how the LV region affects solid earth deformation, by varying parameters that describe the LV region. These parameters are the LV region thickness, radius, depth, and viscosity, the distance between the LV region and the ice load (measured between the centers), and the ice load radius. The maximum vertical surface deformation (Figure II.3) and rate (Figure II.4) at 100 years give insight into how these parameters affect solid earth deformation. We chose parameter ranges to span the range of influence of each parameter.

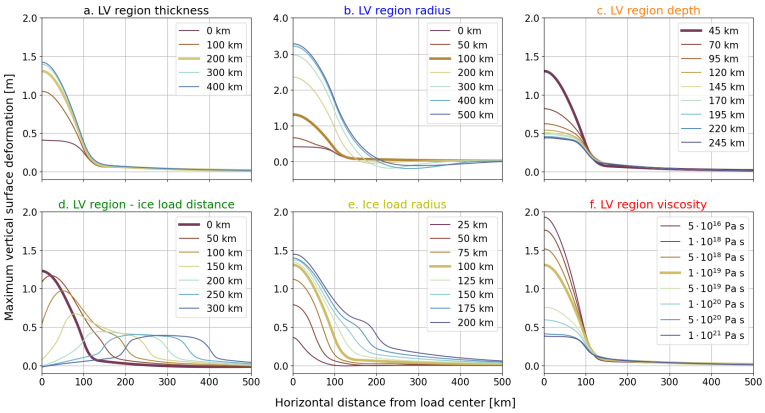

Figure II.3: Maximum vertical surface deformation (at t = 100 years) as function of horizontal distance from the ice load center for the (a) LV region thickness, (b) LV region radius, (c) LV region depth, (d) distance between the LV region and ice load center, (e) ice load radius, and (f) LV region viscosity. Each colored line represents a variation of the given parameter, and the thick line refers to the parameter value used in the reference case. Note that for the LV region radius (b) the y axis range is doubled.

The reference earth model and ice load are as in case C in the previous section. For the distance between the LV region and the ice load we use the full box geometry. For the other parameters tested (Figures II.3 and II.4), we take advantage of model symmetry and use a quarter of the box model geometry (as shown in Figure II.1b), but with free-slip conditions on the left and front lateral boundaries. We limit the model horizontal dimension to 500 km (reduced from 1,500 km used for Figure II.2), introducing only a <0.5% error compared to a very wide (∼3,000 km) box, and resulting in a ∼3 times faster computation for case C (18 vs. 53 min on 512 CPU).

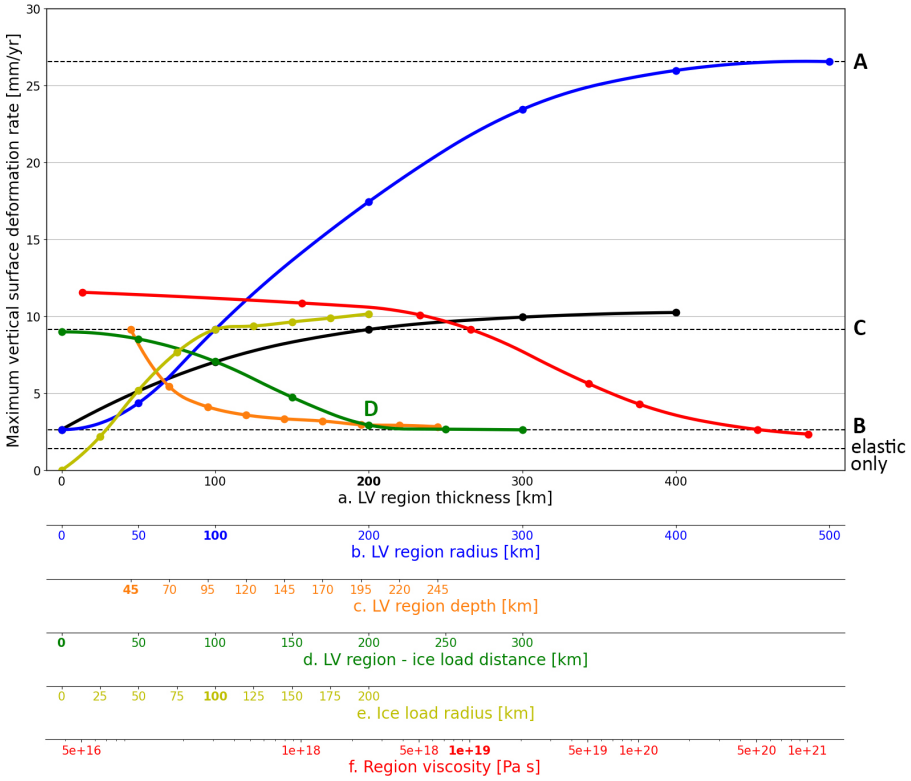

Figure II.4: Maximum vertical surface deformation rate (at t = 100 years) as function of the (black) LV region thickness, (blue) LV region radius, (orange) LV region depth, (green) distance between the LV region and ice load center, (yellow) ice load radius, and (red) LV region viscosity (colors refer to lines and corresponding x axes). The colored dots indicate model runs and the lines are second order spline interpolated values. The four horizontal dashed lines correspond to cases A, B, C, and purely elastic, and the green dot labeled D corresponds to case D (See Figure II.1c for the cases). For each given parameter, the bold values on the x axes represent the parameter value used in the reference case.

For a purely elastic case (viscosities in all layers are set to $1{\cdot}10^{40}$ Pa s) the maximum deformation rate is 1.4 mm/yr. The elastic contribution to the deformation rate at 100 years is 5% for case A, 53% for case B, 15% for case C, and 48% for case D. Thus, the viscous contribution to the deformation rate is of comparable size (for cases B and D) or larger than (for cases A and C) the elastic contribution, in the presence of a low-viscosity feature (Figure II.4).

II.3.1 Low-Viscosity Region Thickness

We vary the LV region thickness from 0 km (no LV region) to 400 km. The maximum vertical surface deformation increases with increasing LV region thickness (Figure II.3a), by a factor of ∼3. The maximum rate ranges from 2.6 to 10.2 mm/yr (Figure II.4a), a factor ∼4 difference. The deformation saturates for thicknesses greater than 200 km, for which the rate already reaches 9.1 mm/yr.

II.3.2 Low-Viscosity Region Radius

We vary the LV region radius from 0 km (no LV region) to 500 km (approximating an LV asthenosphere). The maximum vertical surface deformation increases with increasing LV region radius (Figure II.3b). Standing out is the subsidence in the periphery of the ice load (also seen in Figure II.2, case A), which appears when the LV region radius is larger than the ice load radius (i.e., >100 km). Of all six parameters, the LV region radius produces the largest range in deformation rates, from 2.6 to 26.6 mm/yr (Figure II.4b), a factor ∼10 difference.

II.3.3 Low-Viscosity Region Depth

We vary the LV region depth (defined at the upper surface of the LV region) from 45 km (top surface immediately below the elastic lithosphere) to 245 km. The maximum vertical surface deformation decreases with an increase in LV region depth (Figure II.3c), by a factor of ∼3. At a depth of 245 km, the presence of the LV region is barely apparent and approximates the solution for no LV region (as case B). The LV region thus is most important at shallower depths, with a drop in deformation rate from 9.1 to 3.3 mm/yr for an LV region depth from 45 to 145 km, nearly a factor 3 difference (Figure II.4c).

II.3.4 Low-Viscosity Region and Ice Load Distance

We vary the distance between the LV region and ice load from 0 km (overlapping) to 300 km (100 km between the boundaries of the two). The maximum vertical surface deformation decreases if the LV region is farther away from the ice load (Figure II.3d). The location of maximum deformation moves with the location of the ice load and the deformation profile becomes increasingly asymmetric. For distances larger than 200 km, the deformation beneath the ice load is no longer sensitive to the LV region. In this case, deformation profiles become symmetric again, and uplift rates of 2.6 mm/yr approximate rates for earth models without an LV region (Figure II.4d).

II.3.5 Ice Load Radius

We vary the ice load radius from 25 to 200 km (twice as large as the LV region radius). The maximum vertical surface deformation increases with the ice load radius, by a factor of ∼4 (Figure II.3e). There is little change in the maximum

deformation and rate for ice load radii larger than the LV region radius of 100 km (Figures II.3e and II.4e). For ice load radii larger than 100 km, however, we predict large deformations for distances greater than the LV region radius. The deformation of this second bulge saturates around 0.5 m, which is comparable to the uplift expected without an LV region (case B), as this outer part of the ice load cannot sense the LV region.

II.3.6 Low-Viscosity Region Viscosity

We vary the LV region viscosity from $5{\cdot}10^{16}$ Pa s to $1{\cdot}10^{21}$ Pa s (a higher viscosity than the surrounding mantle). The maximum vertical surface deformation decreases with an increase in LV region viscosity, by a factor $\sim$5 (Figure II.3f). The maximum rate ranges from 11.6 to 2.3 mm/yr (Figure II.4f), but changes little for viscosities lower than $1{\cdot}10^{19}$ Pa s (from 9.1 to 11.6 mm/yr). On the other hand, increasing the viscosity by one order of magnitude (from $1{\cdot}10^{19}$ to $1{\cdot}10^{20}$ Pa s) slows the uplift rate by more than a factor of 2 (from 9.1 to 4.3 mm/yr).

II.4 Discussion

II.4.1 Factors Affecting Uplift From Contemporary Ice Melt

Uncertainty in the location, viscosity, and even more so dimensions, of an LV region translates directly into uncertainty in the uplift and uplift rates resulting from contemporary ice melt. The largest uncertainty in uplift rates comes from the horizontal extent of the LV region (Figures II.3b and II.4b), where we see that expanding the LV region size can nearly triple uplift rates. Furthermore, we identify ranges of parameter values for which small variations lead to large differences in uplift rates (Figure II.4). These parameter ranges are the LV region thickness up to 200 km, LV region depth up to 145 km, ice load radius up to 100 km (i.e., up to the LV region radius), LV region and ice load distance up to 200 km, and LV region viscosities up to 50 times smaller than the surrounding mantle. Moreover, the LV region radius, distance between the LV region and ice load, and ice load radius greatly impact the spatial pattern of deformation (Figure II.3).

Although we employ a linear Maxwell viscoelastic rheology in this study, other more complex rheologies are likely for the mantle. Ivins et al. (2021) described three different flow laws to derive lateral viscosity variations from a seismic model. These flow laws either assume diffusion creep (used in this study), dislocation creep, or a combination of both (i.e., composite flow law). The choice of flow law can locally result in subsurface viscosities that vary by several orders of magnitude depending on the flow law. Large uncertainties may also arise from unknown variability in grain size, water content, and composition (van der Wal et al., 2015). Recent studies explore time- and stress-dependent viscosity (i.e., transient rheology) (Kang et al., 2022) in Antarctica (Lau et al., 2021; Blank et al., 2021) and Greenland (Adhikari et al., 2021). For example,

several studies focused on similar locations have resulted in different estimates for mantle viscosity and lithosphere thickness based on historical sea level data and present-day deformation. Lau et al. (2021) argued that these different estimates result from different timescales of deformation and that transient, frequency-dependent, rheology may play an important role on GIA timescales. Kang et al. (2022) showed that stress-dependent rheology causes temporal variations in upper mantle viscosity due to stress variations during the last deglaciation (ended 8,000 years ago), and that the effects can be rather localized (i.e., affecting load-proximal stresses but not far field stresses). Such rheological complexity may also contribute to, or even generate, confined regions with effectively low viscosity, of the sort that we have modeled here. Regardless, the impact of rheological complexity needs more investigation and could help to reconcile models and observations of uplift (Adhikari et al., 2021; Blank et al., 2021; Lau et al., 2021).

II.4.2 Importance of Contemporary Ice Melt for Greenland Uplift

Bevis et al. (2012) found that in most of coastal Greenland the elastic response to contemporary ice mass change matches the historic viscous response or dominates the uplift signal. However, we show that the viscous response from contemporary ice melt can also significantly contribute to the total uplift, and is a component that is not commonly considered. Simpson et al. (2011) did consider the viscous response from contemporary ice melt, but applied a radially symmetric earth viscosity structure. For areas of rapid ice mass loss near low-viscosity regions of the upper mantle, uplift may be dominated by recent or contemporary ice melt instead of by historic ice melt from the last deglaciation. Furthermore, we show that the GIA signal from contemporary ice change may not grow linearly over short timescales in the presence of an LV region (Figure II.2, compare deformation at 50 vs. 100 years). This can complicate (a) studies in which GNSS uplift rates are corrected for GIA from historic ice load changes and the remaining (assumed elastic) deformation is used to constrain contemporary ice discharge, an approach that Hansen et al. (2021) used to constrain mass loss from Greenland's three largest outlet glaciers, and (b) studies in which an elastic correction for contemporary ice change is applied to GNSS uplift rates to infer the GIA signal from past ice change, because the viscous response from contemporary ice change is not considered.

II.4.3 1D Versus 3D Modeling for Greenland

The 1D approach adopted by, for example, Khan et al. (2016) to estimate ice history and earth rheology in Greenland may be valid for some regions of Greenland, but perhaps not for southeast Greenland, which is likely characterized by a confined LV region in the upper mantle (Figure II.1a). By applying a layered viscosity structure per drainage basin, Khan et al. (2016) effectively expanded the LV feature in southeast Greenland infinitely (as a full LV asthenospheric layer) for the ice loss in that region. We show that using a wide LV region

highly overestimates uplift rate, by up to 3 times, if the actual LV region is confined. Figure II.1a shows that an LV region of 300 km radius already overlaps with larger positive velocity anomalies in the upper mantle, indicating higher viscosity. Our modeled uplift rates show that there is a significant reduction in rates for LV regions with a radius smaller than 300 km compared to an LV asthenospheric layer (Figure II.4b). This means that to reconcile models and observations of uplift using a 3D approach instead of a 1D approach (i.e., to achieve larger modeled uplift rates with a 3D approach), the ice melt must be larger/faster and/or the LV region must be even shallower (Figure II.4c) or have an even lower viscosity (Figure II.4f) than considered here. Alternatively, more complex creep mechanisms need to be considered (Section II.4.1). Furthermore, the 1D approach generates subsidence across a wide horizontal extent of the LV region, due to channel flow.

The 1D approach, regardless of the presence of an LV layer, may be valid for long-wavelength loading in the far field (Hartmann et al., 2020), but it is not a valid approach near an LV region, because it does not account for stresses that are transmitted through rheological boundaries. Furthermore, even if the LV region is very wide (e.g., as wide as the drainage basin), deformation in neighboring drainage basins (without an LV layer) may also be affected (Figures II.3d and II.4d) because the influence of a nearby LV region cannot be captured in the 1D approach. A 1D approach may be valid in regions with a broad LV region, as Marsman et al. (2021) found for Alaska, where lateral viscosity variations ($1.6{\cdot}10^{19}$ to $5.0{\cdot}10^{19}$ Pa s in the shallow upper mantle) across a broad region (1,425 by 2,325 km) did not improve the fit to observations compared to a 1D model. However, southeast Greenland is likely characterized by a confined LV region (Figure II.1a) that is small enough to significantly reduce uplift rates compared to a 1D case (LV layer). For Antarctica, there are large viscosity variations between East and West Antarctica, and even within West Antarctica and the Antarctic Peninsula seismic velocity anomalies vary greatly in the upper mantle (Lloyd et al., 2020). A 1D approach may be accurate for selected regions where the viscosity does not vary much laterally over a wide region, but not near rheological boundaries.

II.4.4 Ice Sheet and Glacier Dynamics

Rapid uplift from contemporary ice melt may also impact ice sheet and glacier dynamics. When ice melts, the surface elevation decreases and the ice is subjected to warmer temperatures and larger melt rates, leading to further ice melt, and potential ice sheet destabilization (Levermann et al., 2013). However, GIA counteracts this feedback by increasing the surface elevation when ice melts (Zeitz et al., 2022), and fast uplift above LV regions can amplify this feedback. For marine terminating glaciers, GIA can stabilize the grounding line. Ice melt far from the grounding line results in local sea level rise and potential grounding line retreat, while ice melt close to the grounding line (i.e., close enough to trigger isostatic effects at the grounding line) causes solid earth uplift and local

sea level fall, leading to grounding line advance if the viscoelastic response is large/fast enough to counteract the ice thinning (Whitehouse, 2018; Whitehouse et al., 2019). Thus, near LV regions with rapid solid earth uplift, this feedback may limit future ice loss (Gomez et al., 2015; Konrad et al., 2015; Pollard et al., 2017; Gomez et al., 2018; Kachuck et al., 2020). The feedback of local sea level change on grounding line position is more evident in Antarctica than Greenland, as most marine terminating glaciers in Greenland do not have large floating ice sections (Khan et al., 2020). However, grounding line positions, and thus stability, of these glaciers are affected by solid earth uplift due to ice thinning. West Antarctica is characterized by low upper mantle viscosities (although absolute mantle viscosity is still poorly constrained and could benefit from an inversion using a variety of geophysical data (Ramirez et al., 2022)), and large ice mass loss (The IMBIE Team, 2018); a combination that may help to stabilize the ice sheet.

II.5 Conclusion

Our viscoelastic deformation models show that contemporary ice melt generates not only an elastic response of the solid earth but also a viscous response. If the melting occurs near a low-viscosity region of the upper mantle, then this viscous response can be larger than the elastic response (Figure II.4f). With such a large viscous contribution, uplift in areas of large ice melt can be controlled by recent or contemporary ice melt instead of by historic ice melt from the last deglaciation. From a sensitivity analysis of the location, dimensions, and viscosity of an LV region, we find that the largest uncertainty in uplift rates from contemporary ice melt comes from the horizontal extent of the LV region. We find that uplift from contemporary ice melt can be as much as 10 times larger for a very wide (essentially infinite) LV region than it is without an LV region, and a confined LV region produces intermediate rates. Our modeled uplift rates show that there is a significant reduction in rates for LV regions with a radius smaller than 300 km compared to an LV asthenospheric layer (Figure II.4b). Thus, 3D modeling is important near areas of reduced viscosity in the upper mantle. As the LV region amplifies GIA uplift from contemporary ice melt, it is important to constrain the location, dimensions, and viscosity of an LV region in order to distinguish between uplift generated by past and contemporary ice melt. Rapid viscous ground uplift can impact ice dynamics if the low-viscosity region is located close to an ice sheet margin, as for Antarctica and Greenland.

Acknowledgments

The authors thank an anonymous reviewer and Pippa Whitehouse for their reviews, which helped us to improve the manuscript, and Rebekka Steffen for her feedback on the 1D versus 3D modeling. This work was supported by the Norwegian Research Council projects 223272 (Centre of Excellence) and 288449 (MAGPIE Project). Computations were made possible by the Norwegian

Research Infrastructure Services (NRIS) via allocations NN9283K/NS9029K. We thank the Computational Infrastructure for Geodynamics (geodynamics.org), which is funded by the National Science Foundation under award nos. EAR-0949446 and EAR-1550901, for supporting the development of ASPECT.

Open Research: Data Availability Statement

The open-source code ASPECT (v2.3.0) (Bangerth et al., 2021b) is available for download on GitHub (https://github.com/geodynamics/aspect) or Zenodo (https://doi.org/10.5281/zenodo.5131909), along with an example parameter file for the reference case (https://doi.org/10.5281/zenodo.6861410). In Figures II.2 and II.3 the scientific cyclic colour map romaO is used (Crameri, 2018).

Supporting Information S1

Text II.S1: Conservation Equations
For the GIA simulations, ASPECT solves the 3-D incompressible conservation equations assuming an infinite Prandtl number, the Boussinesq approximation, and isothermal flow. The constitutive equations thus only consist of the momentum and continuity equation. Force terms are added on the right-hand-side of the momentum equation to account for the viscoelastic behavior and boundary traction. For incompressible and isothermal flow, under the Boussinesq approximation, the momentum equation (Eq. II.1) and continuity equation (Eq. II.2) reduce to:

$$-\nabla \cdot [2\eta_{\text{eff}}\dot{\epsilon}(\mathbf{u})] + \nabla p = \rho\mathbf{g} + \nabla \cdot F_{\text{e}} + \nabla \cdot F_{\text{t}} \tag{II.1}$$

$$\nabla \cdot \mathbf{u} = 0 \tag{II.2}$$

where η_{eff} is the effective viscoelastic viscosity, $\dot{\epsilon}$ the strain rate, $\mathbf{u}$ the velocity, p the total pressure, ρ the density, $\mathbf{g}$ the gravity vector, F_{e} the elastic force term, F_{t} the boundary traction force term, and $2\eta_{\text{eff}}\dot{\epsilon}(\mathbf{u})$ represents the deviatoric stress.

Text II.S2: Viscoelastic Rheology.
The viscoelastic rheology is implemented through an elastic force term, and an effective viscosity in the momentum equation (Eq. II.1) that accounts for the viscous and elastic deformation mechanisms. Our methodology for modeling viscoelasticity in ASPECT follows the approach of Moresi et al. (2003), as outlined in Sandiford et al. (2021). Within a timestep, first the viscoelastic stresses are updated, then the properties are updated through a reaction term in the advection equation, followed by constructing and solving the Stokes system with the elastic force term.

The velocity gradient tensor $\boldsymbol{I}^t$ and deviatoric stress tensor $\boldsymbol{\tau}^t$ are constructed from the velocity solution and stored stress components of the previous timestep

t. The new viscoelastic stresses become:

$$\boldsymbol{\tau}^{t+\Delta t} = \eta_{eff}\left(2\hat{\boldsymbol{D}}^t + \frac{\boldsymbol{\tau}^t}{\mu\Delta t} + \frac{\boldsymbol{W}^t\boldsymbol{\tau}^t - \boldsymbol{\tau}^t\boldsymbol{W}^t}{\mu}\right) \tag{II.3}$$

with

$$\hat{\boldsymbol{D}} = \frac{1}{2}\left(\boldsymbol{I} + \boldsymbol{I}^T\right) \tag{II.4}$$

$$\boldsymbol{W} = \frac{1}{2}\left(\boldsymbol{I} - \boldsymbol{I}^T\right) \tag{II.5}$$

$$\eta_{eff} = \eta\frac{\Delta t}{\Delta t + \alpha} \tag{II.6}$$

where superscript t and $t + \Delta t$ indicate the previous and current timestep, and μ is the shear modulus. $\hat{\boldsymbol{D}}$ and $\boldsymbol{W}$ are the deviatoric rate of deformation tensor (Eq. II.4) and the spin tensor (Eq. II.5), respectively, and are a function of the velocity gradient tensor. η_{eff} is the effective viscosity (Eq. II.6) and is defined as a function of viscosity, timestep size and shear relaxation time α, where $\alpha = \eta/\mu$.

With the viscoelastic stresses of the previous and current timestep, the reaction term for the deviatoric stress q is determined. Materials are being tracked on compositional fields and for each field $c_i\,(x,t)$ with $i = 1...C$ an advection equation is solved which updates the stresses on the fields:

$$\frac{\partial c_i}{\partial t} + \mathbf{u}\cdot\nabla c_i = q_i \tag{II.7}$$

with

$$q = \boldsymbol{\tau}^{t+\Delta t} - \boldsymbol{\tau}^t \tag{II.8}$$

Then, the Stokes system (Eq. II.1 and II.2) is constructed with the updated deviatoric stress and the elastic force term, which is defined as:

$$F_e = -\frac{\eta_{eff}}{\eta_e}\boldsymbol{\tau}^{t+\Delta t} \tag{II.9}$$

where η_e is the elastic viscosity and equals $\mu\Delta t$. With this Stokes system, we can solve for the new velocity field.

Text II.S3: Boundary Conditions.
In this study, we use a free surface on the top boundary (Rose et al., 2017) (i.e. the earth's surface). The free surface is defined as having zero stress on the boundary. Thus, the following condition must be satisfied: $\sigma\cdot\mathbf{n} = 0$, where $\mathbf{n}$ is the vector normal to the boundary and total stress $\sigma = 2\eta_{\text{eff}}\dot{\epsilon}\,(\mathbf{u})$ (i.e. the total stress is the deviatoric stress since there is no pressure gradient at the top surface). When there is flow across the boundary, the mesh must be able to deform to satisfy the above condition. On the free surface, mesh velocity $\mathbf{u}_m$ is calculated as follows:

$$\mathbf{u}_m = (\mathbf{u} \cdot \mathbf{n})\,\mathbf{n} \tag{II.10}$$

Using this approach, the Eulerian advection terms need to be corrected for the mesh velocity. The momentum and continuity equations become:

$$-\nabla \cdot [2\eta_{\text{eff}}\dot{\epsilon}(\mathbf{u} - \mathbf{u}_m)] + \nabla p = \rho\mathbf{g} + \nabla \cdot F_{\text{e}} + \nabla \cdot F_{\text{t}} \tag{II.11}$$

$$\nabla \cdot (\mathbf{u} - \mathbf{u}_m) = 0 \tag{II.12}$$

Furthermore, a quasi-implicit integration scheme is used to prevent free surface position instabilities arising from small deviations in the free surface location.

Next to the free surface on the top boundary, we also apply a traction force to represent the surface ice loading. The ice loading is a known external force, resulting in an unknown velocity. The given pressure is applied as a force that is normal to the boundary. The boundary traction is represented as F_{t} in the momentum equation (Eq. II.1). The other boundaries are either free-slip or open boundaries. The free-slip boundary requires that the flow is tangential to the boundary, i.e. $\mathbf{u} \cdot \mathbf{n} = 0$. For the open boundary, material can flow in and out of the model domain. Because inflow and outflow velocities are unknown, a 1D lithostatic pressure profile at a location of choice is computed from the model start situation and applied as boundary traction.

Table II.S1: Layer properties for case A. The density is the average mantle density and the shear moduli are PREM-averaged values for their depths (Dziewonski & Anderson, 1981).

Layer	Thickness T (km)	Density ρ (kg m^{-3})	Shear modulus μ (Pa)	Viscosity η (Pa s)	Relaxation time $\tau(=\eta/\mu)$ (yr)
Lithosphere, $_L$	45	4450	$0.45{\cdot}10^{11}$	$1{\cdot}10^{40}$	$7{\cdot}10^{21}$
Asthenosphere, $_A$	200	4450	$1.75{\cdot}10^{11}$	$1{\cdot}10^{19}$	1.8
Upper mantle, $_M$	255	4450	$1.75{\cdot}10^{11}$	$5{\cdot}10^{20}$	90.5

References

Adhikari, S., Milne, G. A., Caron, L., Khan, S. A., Kjeldsen, K. K., Nilsson, J., ... Ivins, E. R. (2021). Decadal to Centennial Timescale Mantle Viscosity Inferred From Modern Crustal Uplift Rates in Greenland. *Geophysical Research Letters*, *48*. doi: 10.1029/2021GL094040

Bangerth, W., Dannberg, J., Fraters, M., Gassmoeller, R., Glerum, A., Heister, T., & Naliboff, J. (2021a). *ASPECT: Advanced Solver for Problems in Earth's ConvecTion, User Manual.* doi: 10.6084/m9.figshare.4865333

Bangerth, W., Dannberg, J., Fraters, M., Gassmoeller, R., Glerum, A., Heister, T., & Naliboff, J. (2021b). *ASPECT v2.3.0.* Zenodo. doi: 10.5281/zenodo.5131909

Barletta, V., Bevis, M., Smith, B., Wilson, T., Brown, A., Bordoni, A., ... Wiens, D. (2018). Observed rapid bedrock uplift in amundsen sea embayment promotes ice-sheet stability. *Science*, *360*, 1335–1339. doi: 10.1126/science.aao1447

Bevis, M., Wahr, J., Khan, S. A., Madsen, F. B., Brown, A., Willis, M., ... Francis, O. (2012). Bedrock displacements in Greenland manifest ice mass variations, climate cycles and climate change. *Proceedings of the National Academy of Sciences*, *109*(30), 11944-11948. doi: 10.1073/pnas.1204664109

Blank, B., Barletta, V., Hu, H., Pappa, F., & van der Wal, W. (2021). Effect of Lateral and Stress-Dependent Viscosity Variations on GIA Induced Uplift Rates in the Amundsen Sea Embayment. *Geochemistry, Geophysics, Geosystems*, *22*(9), e2021GC009807. doi: 10.1029/2021GC009807

Bredow, E., Steinberger, B., Gassmoeller, R., & Dannberg, J. (2021). Mantle convection and possible mantle plumes beneath Antarctica – insights from geodynamic models and implications for topography. *Geological Society, London, Memoirs*, *56*. doi: https://doi.org/10.1144/M56-2020-2

Brough, S., Carr, J. R., Ross, N., & Lea, J. M. (2019). Exceptional Retreat of Kangerlussuaq Glacier, East Greenland, Between 2016 and 2018. *Frontiers in Earth Science*, *7*(123). doi: 10.3389/feart.2019.00123

Cathles, L. M. (1975). The viscosity of the earth's mantle. In (p. 386). Princeton University Press, Princeton, New Jersey.

Celli, N. L., Lebedev, S., Schaeffer, A. J., & Gaina, C. (2021). The tilted iceland plume and its effect on the north atlantic evolution and magmatism. *Earth and Planetary Science Letters*, *569*, 117048. doi: 10.1016/j.epsl.2021.117048

Crameri, F. (2018). *Scientific colour maps.* Zenodo. doi: 10.5281/zenodo.1243862

Dziewonski, A. M., & Anderson, D. L. (1981). Preliminary reference Earth model. *Physics of the Earth and Planetary Interiors*, *25*, 297-356. doi: 10.1016/0031-9201(81)90046-7

Gomez, N., Latychev, K., & Pollard, D. (2018). A Coupled Ice Sheet–Sea Level Model Incorporating 3D Earth Structure: Variations in Antarctica during the Last Deglacial Retreat. *Journal of Climate*, *31*, 4041-4054. doi: 10.1175/JCLI-D-17-0352.1

Gomez, N., Pollard, D., & Holland, D. (2015). Sea-level feedback lowers projections of future Antarctic Ice-Sheet mass loss. *Nature Communications*, *6*(8798). doi: 10.1038/ncomms9798

Hansen, K., Truffer, M., Aschwanden, A., Mankoff, K., Bevis, M., Humbert, A., ... Khan, S. A. (2021). Estimating Ice Discharge at Greenland's Three Largest Outlet Glaciers Using Local Bedrock Uplift. *Geophysical Research Letters*, *48*. doi: 10.1029/2021GL094252

Hartmann, R., Ebbing, J., & Conrad, C. P. (2020). A Multiple 1D Earth Approach (M1DEA) to account for lateral viscosity variations in solutions of the sea level equation: An application for glacial isostatic adjustment

by Antarctic deglaciation. *Journal of Geodynamics*, *135*, 101695. doi: 10.1016/j.jog.2020.101695

Heeszel, D. S., Wiens, D. A., Anandakrishnan, S., Aster, R. C., Dalziel, I. W. D., Huerta, A. D., ... Winberry, J. P. (2016). Upper mantle structure of central and West Antarctica from array analysis of Rayleigh wave phase velocities. *Journal of Geophysical Research: Solid Earth*, *121*, 1758-1775. doi: 10.1002/2015JB012616

Helm, V., Humbert, A., & Miller, H. (2014). Elevation and elevation change of Greenland and Antarctica derived from CryoSat-2. *The Cryosphere*, *8*, 1539-1559. doi: 10.5194/tc-8-1539-2014

Ivins, E. R., & Sammis, C. G. (1995). On lateral viscosity contrast in the mantle and the rheology of low-frequency geodynamics. *Geophysical Journal International*, *123*, 305-322. doi: 10.1111/j.1365-246X.1995.tb06856.x

Ivins, E. R., van der Wal, W., Wiens, D. A., Lloyd, A. J., & Caron, L. (2021). Antarctic upper mantle rheology. *Geological Society, London, Memoirs*, *56*. doi: 10.1144/M56-2020-19

Kachuck, S. B., Martin, D. F., Bassis, J. N., & Price, S. F. (2020). Rapid Viscoelastic Deformation Slows Marine Ice Sheet Instability at Pine Island Glacier. *Geophysical Research Letters*, *47*, e2019GL086446. doi: 10.1029/2019GL086446

Kang, K., Zhong, S., A, G., & Mao, W. (2022). The effects of non-Newtonian rheology in the upper mantle on relative sea level change and geodetic observables induced by glacial isostatic adjustment process. *Geophysical Journal International*, *228*, 1975-1991. doi: 10.1093/gji/ggab428

Khan, S. A., Bjørk, A. A., Bamber, J. L., Morlighem, M., Bevis, M., Kjær, K. H., ... Schenk, T. (2020). Centennial response of Greenland's three largest outlet glaciers. *Nature Communications*, *11*. doi: 10.1038/s41467-020-19580-5

Khan, S. A., Sasgen, I., Bevis, M., van Dam, T., Bamber, J. L., Wahr, J., ... Munneke, P. K. (2016). Geodetic measurements reveal similarities between post–Last Glacial Maximum and present-day mass loss from the Greenland ice sheet. *Science Advances*, *2*(9). doi: 10.1126/sciadv.1600931

Konrad, H., Sasgen, I., Pollard, D., & Klemann, V. (2015). Potential of the solid-Earth response for limiting long-term West Antarctic Ice Sheet retreat in a warming climate. *Earth and Planetary Science Letters*, *432*, 254-264. doi: 10.1016/j.epsl.2015.10.008

Lau, H. C. P., Austermann, J., Holtzman, B. K., Havlin, C., Lloyd, A. J., Book, C., & Hopper, E. (2021). Frequency Dependent Mantle Viscoelasticity via the Complex Viscosity: Cases From Antarctica. *Journal of Geophysical Research: Solid Earth*, *126*(e2021JB022622). doi: 10.1029/2021JB022622

Levermann, A., Clark, P. U., Marzeion, B., Milne, G. A., Pollard, D., Radic, V., & Robinson, A. (2013). The multimillennial sea-level commitment of global warming. *Proceedings of the National Academy of Sciences*, *110*(34), 13745-13750. doi: 10.1073/pnas.1219414110

Lloyd, A. J., Wiens, D. A., Zhu, H., Tromp, J., Nyblade, A. A., Aster, R. C., ... O'Donnell, J. P. (2020). Seismic Structure of the Antarctic Upper Mantle

Imaged with Adjoint Tomography. *Journal of Geophysical Research: Solid Earth*, *125*. doi: 10.1029/2019JB017823

Marsman, C. P., van der Wal, W., Riva, R. E. M., & Freymueller, J. T. (2021). The Impact of a 3-D Earth Structure on Glacial Isostatic Adjustment in Southeast Alaska Following the Little Ice Age. *Journal of Geophysical Research: Solid Earth*, *126*, e2021JB022312. doi: 10.1029/2021JB022312

Martos, Y. M., Jordan, T. A., Catalán, M., Jordan, T. M., Bamber, J. L., & Vaughan, D. G. (2018). Geothermal Heat Flux Reveals the Iceland Hotspot Track Underneath Greenland. *Geophysical Research Letters*, *45*, 8214-8222. doi: 10.1029/2018GL078289

Milne, G. A., Latychev, K., Schaeffer, A., Crowley, J. W., Lecavalier, B. S., & Audette, A. (2018). The influence of lateral Earth structure on glacial isostatic adjustment in Greenland. *Geophysical Journal International*, *214*, 1252–1266. doi: 10.1093/gji/ggy189

Mordret, A. (2018). Uncovering the Iceland Hot Spot Track Beneath Greenland. *Journal of Geophysical Research: Solid Earth*, *123*, 4922-4941. doi: 10.1029/2017JB015104

Moresi, L., Dufour, F., & Mühlhaus, H.-B. (2003). A Lagrangian integration point finite element method for large deformation modeling of viscoelastic geomaterials. *Journal of Computational Physics*, *184*, 476-497. doi: 10.1016/S0021-9991(02)00031-1

Nield, G. A., Barletta, V. R., A. Bordoni and, M. A. K., Whitehouse, P. L., Clarke, P. J., Domack, E., ... Berthier, E. (2014). Rapid bedrock uplift in the Antarctic Peninsula explained by viscoelastic response to recent ice unloading. *Earth and Planetary Science Letters*, *397*, 32-41. doi: 10.1016/j.epsl.2014.04.019

Pollard, D., Gomez, N., & Deconto, R. M. (2017). Variations of the Antarctic Ice Sheet in a Coupled Ice Sheet-Earth-Sea Level Model: Sensitivity to Viscoelastic Earth Properties. *Journal of Geophysical Research: Earth Surface*, *122*, 2124-2138. doi: 10.1002/2017JF004371

Ramirez, F., Selway, K., Conrad, C. P., & Lithgow-Bertelloni, C. (2022). Constraining upper mantle viscosity using temperature and water content inferred from seismic and magnetotelluric data. *Journal of Geophysical Research: Solid Earth*, *127*, e2021JB023824. doi: 10.1029/2021JB023824

Rogozhina, I., Petrunin, A. G., Vaughan, A. P. M., Steinberger, B., Johnson, J. V., Kaban, M. K., ... Koulakov, I. (2016). Melting at the base of the Greenland ice sheet explained by Iceland hotspot history. *Nature Geoscience*, *9*, 366-369. doi: 10.1038/ngeo2689

Rose, I., Buffett, B., & Heister, T. (2017). Stability and accuracy of free surface time integration in viscous flows. *Physics of the Earth and Planetary Interiors*, *262*, 90-100. doi: 10.1016/j.pepi.2016.11.007

Sandiford, D., Brune, S., Glerum, A., Naliboff, J. B., & Whittaker, J. M. (2021). Kinematics of footwall exhumation at oceanic detachment faults: Solid-block rotation and apparent unbending. *Geochemistry, Geophysics, Geosystems*, *22*(4), e2021GC009681. doi: 10.1029/2021GC009681

Simpson, M. J. R., Wake, L., Milne, G. A., & Huybrechts, P. (2011). The

influence of decadal- to millennial-scale ice mass changes on present-day vertical land motion in Greenland: Implications for the interpretation of GPS observations. *Journal of Geophysical Research: Solid Earth*, *116*. doi: 10.1029/2010jb007776

Steffen, R., Audet, P., & Lund, B. (2018). Weakened Lithosphere Beneath Greenland Inferred From Effective Elastic Thickness: A Hot Spot Effect? *Geophysical Research Letters*, *45*, 4733-4742. doi: 10.1029/2017GL076885

Steinberger, B., Bredow, E., Lebedev, S., Schaeffer, A., & Torsvik, T. H. (2019). Widespread volcanism in the Greenland–North Atlantic region explained by the Iceland plume. *Nature Geoscience*, *12*, 61-68. doi: 10.1038/s41561-018-0251-0

The IMBIE Team. (2018). Mass balance of the Antarctic Ice Sheet from 1992 to 2017. *Nature*, *558*, 219-222. doi: 10.1038/s41586-018-0179-y

The IMBIE Team. (2020). Mass balance of the Greenland Ice Sheet from 1992 to 2018. *Nature*, *579*, 233-239. doi: 10.1038/s41586-019-1855-2

van der Wal, W., Barnhoorn, A., Stocchi, P., Gradmann, S., Wu, P., Drury, M., & Vermeersen, B. (2013). Glacial isostatic adjustment model with composite 3-D Earth rheology for Fennoscandia. *Geophysical Journal International*, *194*(1), 61-77. doi: 10.1093/gji/ggt099

van der Wal, W., Whitehouse, P. L., & Schrama, E. J. O. (2015). Effect of GIA models with 3D composite mantle viscosity on GRACE mass balance estimates for Antarctica. *Earth and Planetary Science Letters*, *414*, 134-143. doi: 10.1016/j.epsl.2015.01.001

Whitehouse, P. L. (2018). Glacial isostatic adjustment modelling: historical perspectives, recent advances and future directions. *Earth Surface Dynamics*, *6*, 401-429. doi: 10.5194/esurf-6-401-2018

Whitehouse, P. L., Gomez, N., King, M. A., & Wiens, D. A. (2019). Solid Earth change and the evolution of the Antarctic Ice Sheet. *Nature Communications*, *10*(503). doi: 10.1038/s41467-018-08068-y

Wolstencroft, M., King, M. A., Whitehouse, P. L., Bentley, M. J., Nield, G. A., King, E. C., ... Gunter, B. C. (2015). Uplift rates from a new high-density GPS network in Palmer Land indicate significant late Holocene ice loss in the southwestern Weddell Sea. *Geophysical Journal International*, *203*, 737-754. doi: 10.1093/gji/ggv327

Zeitz, M., Haacker, J. M., Donges, J. F., Albrecht, T., & Winkelmann, R. (2022). Dynamic regimes of the Greenland Ice Sheet emerging from interacting melt-elevation, and glacial isostatic adjustment feedbacks. *Earth System Dynamics*, *13*, 1077–1096. doi: 10.5194/esd-13-1077-2022